The investigation into polymer semiconductor photoelectrodes for light-driven water splitting

2019.10

A thesis submitted of the partial fulfilment of the requirements for the degree of

Doctor of Philosophy at University College London

I. Acknowledgements

I want to show my most profound appreciation to my supervisor for his persistent guidance during the course of my PhD study. He conveyed a spirit of adventure in regard to research, which always and will continue to stimulate me to overcome challenges. Without his continuous help, the dissertation would not have been possible.

I am also very grateful to my second supervisor, who had given me constructive suggestions from the beginning of my research.

Great thanks should go to Dr Wenjun Luo, the visiting lecturer in our group. He taught me the basic knowledge of photoelectrochemical and inspired me quite a lot in my research.

My kind colleagues were always helpful and willing to share their knowledge. They make my daily research full of fun. Finally, thanks to my parents for supporting my research and life mentally and physically.

II. Abstract

Photoelectrochemical (PEC) photosynthesis has been regarded as a promising method to convert inexhaustible solar energy to fuels, in which polymer semiconductors have been identified to be promising photocatalysts because they are abundant, environmentally benign, and has easily tuneable band structure. Graphitic carbon nitride (g-C_3N_4) as one of the most promising polymer photocatalysts has realized efficient water splitting in a suspension system. However, its PEC application is limited by its low efficiency due to both unclear understanding of reaction kinetics in the film and low quality g-C_3N_4 film fabricated.

Herein, a novel film fabrication method has been developed to prepare dense, uniform and highly crystallized g-C_3N_4 films as a photoanode with a controllable thickness. Comparing with g-C_3N_4 films prepared by other methods, the relationship between crystallinity, deep trap states and PEC performance of g-C_3N_4 photoelectrodes was investigated. I found that longer-lived charge carriers were present in more poorly crystalline samples, due to more deeply trapped states, which inversely correlated with photoelectrochemical performance. The electron diffusion length in such a crystalline g-C_3N_4 film was determined to be *ca.* 1000 nm, which is the first report for this promising photoelectrode.

Although g-C_3N_4 has a long electron diffusion length, its PEC performance was still minimal due to the low charge carrier density and severe charge recombination. A novel one-step construction approach has then been developed to solve this problem, by synthesising a nanojunction metal-free photoanode, composed of B-doped g-C_3N_4 nanolayer on the surface and bulk

carbon nitride. This type of nanojunction overcame a few intrinsic drawbacks of g-C_3N_4 film, e.g. severe charge recombination and slow charge transfer. For the optimum sample, the top layer of the nanojunction has a depth of ca. 100 nm and the bottom layer is ca. 900 nm. This nanojunction photoanode resulted into a 10 fold higher photocurrent than bulk g-C_3N_4 photoanode with a record photocurrent density of 103.2 μA/cm^2 at 1.23 V vs RHE under one sun condition and a high incident photon-to-current efficiency (IPCE) of ca. 10% at 400 nm. The EIS, MS and IMPS spectroscopies proved such enhancement was mainly due to more than 10 times faster charge transfer rate at electrode/electrolyte interface and nearly 3 times higher conductivity due to the nanojunction structure.

Based on the progress in g-C_3N_4 photoanode, a more challenging topic was explored which is to change g-C_3N_4 semiconductor from a photoanode to a photocathode. Developing g-C_3N_4 photocathode is of great importance because its negative conduction band position is favorable for water reduction, which has been widely proved in a suspension system. However, the intrinsic property of the g-C_3N_4 film as an n-type semiconductor limits hydrogen generation at the electrode/electrolyte interface as n-type semiconductors exhibit upward band bending and holes accumulate on the surface. In this thesis, it is demonstrated that surface trap states could effectively contribute to the photocathodic performance of a g-C_3N_4 film. Introducing nitrogen defects and C-OH terminal groups in the structure of g-C_3N_4 created a large portion of shallow trap states with 1000 times extended lifetime that could trap electrons for the water reduction reaction. This was further validated by hot H_2O_2 treatment that could transfer the g-C_3N_4 photoanode to a photocathode, confirming that shallow trap

states are the critical reason for synthesising a photocathode from an n-type polymer semiconductor. Overall this thesis provides an effective strategy for g-C_3N_4 polymer to be efficient photoanode and photocathode, forming strong basis for its application in solar to H_2 fuel production.

III. Impact statement

Solar-driven fuel synthesis by the photoelectrochemical (PEC) cell is a promising solution to current energy shortage and environmental issue. G-C_3N_4 as a polymer semiconductor is very popular due to its excellent light adsorption in the visible-light region, tunable band structure, facile synthesis process, chemical and thermal stability, environmental benignity and earth abundance. However, the photocatalytic efficiency of g-C_3N_4 photoelectrode is limited due to the lack of fabrication methods of high-quality polymer semiconductor films and very insufficient fundamental understandings. The extremely imbalance between its excellent H_2 and O_2 evolution ability and poor PEC performance inhibits the further application of g-C_3N_4 as a scalable device for water splitting in practice.

To solve this problem, I firstly successfully synthesised dense, uniform and highly crystallized g-C_3N_4 films with controllable thickness with a long electron diffusion length of 1000 nm. This provides a facile method for high-quality polymer films fabrication and stimulates the fundamental research on the charge kinetics in polymer films. Based on these findings, I developed a new nanostructure composed of B-doped g-C_3N_4/g-C_3N_4 which exhibited significantly higher PEC performance than g-C_3N_4 film. This surface nanojunction strategy can be extended to other semiconductors to efficiently improve their applications in the fields of solar fuel conversion and environmental purification. Finally, I demonstrated the key role of shallow trap states in converting n-type semiconductor films from photoanodes to photocathodes. Such discovery would contribute to exploring the potential of n-type polymer semiconductors as efficient hydrogen evolution photoelectrodes.

Overall, the investigation into the polymer films for PEC photosynthesis would contribute to the sustainable production of fuel and mitigating energy and environmental issues, beneficial to the entire societies of solar fuel, solar cell and photocatalysis.

IV. Publications

1. **Ruan, Q**., Luo, W., Xie, J., Wang, Y., Liu, X., Bai, Z., Carmalt, C. J., & Tang, J. (2017). A nanojunction polymer photoelectrode for efficient charge transport and separation. *Angewandte Chemie International Edition*, *56*(28), 8221-8225.

2. **Ruan, Q**., Bayazit, M., Kiran, V., Xie, J., Wang, Y., & Tang, J. (2019). Key Factors Dominating Photoelectrochemical Performance of g-C_3N_4 polymer films. *Chemical Communications*, 55, 7191-7194

3. **Ruan, Q**., Miao, T., & Tang, J. Insight on shallow trap states introduced photocathodic performance in n-type polymer photocatalysts. To be submitted.

4. Jiang, W., **Ruan, Q**., Xie, J., Chen, X., Zhu, Y., & Tang, J. (2018). Oxygen-doped carbon nitride aerogel: A self-supported photocatalyst for solar-to-chemical energy conversion. *Applied Catalysis B: Environmental*, *236*, 428-435.

5. Yaw, C. S., **Ruan, Q**., Tang, J., Soh, A. K., & Chong, M. N. (2019). A Type II nn staggered orthorhombic V_2O_5/monoclinic clinobisvanite $BiVO_4$ heterojunction photoanode for photoelectrochemical water oxidation: Fabrication, characterisation and experimental validation. *Chemical Engineering Journal*, *364*, 177-185.

6. Fu, Q., **Ruan, Q**., McKenzie, T. G., Reyhani, A., Tang, J., & Qiao, G. G. (2017). Development of a Robust PET-RAFT Polymerization Using Graphitic Carbon Nitride (g-C_3N_4). *Macromolecules*, *50*(19), 7509-7516.

7. Xie, J., Shevlin, S. A., **Ruan, Q**., Moniz, S. J., Liu, Y., Liu, X., Li, Y., Lau, C., Guo, Z., & Tang, J. (2018). Efficient visible light-driven water oxidation and proton reduction by an ordered covalent triazine-based framework. *Energy & Environmental Science*, *11*(6), 1617-1624.

8. Wang, Y., Bayazit, M. K., Moniz, S. J., **Ruan, Q**., Lau, C. C., Martsinovich, N., & Tang, J. (2017). Linker-controlled polymeric photocatalyst for highly efficient hydrogen evolution from water. *Energy & Environmental Science*, *10*(7), 1643-1651.

9. Wang, Y., Silveri, F., Bayazit, M. K., **Ruan, Q**., Li, Y., Xie, J., Catlow, A. C., & Tang, J. (2018). Bandgap engineering of organic semiconductors

for highly efficient photocatalytic water splitting. *Advanced Energy Materials*, *8*(24), 1801084.

10. Xie, J., Jin, R., Li, A., Bi, Y., **Ruan, Q**., Deng, Y., Zhang, Y., Yao, S., Sankar, G., Ma, D., & Tang, J. (2018). Highly selective oxidation of methane to methanol at ambient conditions by titanium dioxide-supported iron species. *Nature Catalysis*, *1*(11), 889.

11. Xu, K., Chatzitakis, A., Vøllestad, E., **Ruan, Q**., Tang, J., & Norby, T. (2019). Hydrogen from wet air and sunlight in a tandem photoelectrochemical cell. *International Journal of Hydrogen Energy*, *44*(2), 587-593.

12. Jiang, C., Lee, K. Y., Parlett, C. M., Bayazit, M. K., Lau, C. C., **Ruan, Q**., Moniz, S. A., Lee, A. F., & Tang, J. (2016). Size-controlled TiO2 nanoparticles on porous hosts for enhanced photocatalytic hydrogen production. *Applied Catalysis A: General*, *521*, 133-139.

13. Kong, D., Han, X., Xie, J., **Ruan, Q**., Windle, C. D., Gadipelli, S., Shen, K., Bai, Z., Guo, Z., & Tang, J. (2019). Tunable Covalent Triazine-Based Frameworks (CTF-0) for Visible-Light-Driven Hydrogen and Oxygen Generation from Water Splitting. *ACS Catalysis*, *9*, 7697-7707.

V. Table of Contents

VI. List of Figures

VII. List of Tables

VIII. Nomenclature

Acronyms & initialisms

APCE	Absorbed Photon-to-current Conversion Efficiency
AQY	Apparent Quantum Yield
CB	Conduction Band
CQD	Carbon Quantum Dots
CVD	Chemical Vapor Deposition
DCDA	Dicyandiamide
EIS	Electrochemical Impedance Spectroscopy
IMPS	Intensity Modulated Photocurrent Spectroscopy
IPCE	Incident Photon-to-electron Conversion Efficiency
MS	Mott-Schottky
RHE	Reversible Hydrogen Electrode
OCVD	Open Circuit Voltage Decay
OER	Oxygen Evolution Reaction
PEC	Photoelectrochemical
PS	Photosystem
PV	Photovoltaic
QY	Quantum yield
RHE	Reversible Hydrogen Electrode
STH	Solar to Hydrogen Efficiency
TPV	Transient Photovoltage Decay
VB	Valence Band
V_{fb}	Flat band potential

1 Introduction

1.1 Background

Nowadays, with an increasing population around the world, substantial energy consumption and environmental pollution cause serious concerns. To relieve these concerns, discovery of renewable and clean energy sources is crucial. Among renewable energy sources, solar energy is the most abundant. The average world's energy production (~16.5 TW in 2011) is a small fraction of the amount of solar energy reaching our planet ~173,000 TW, while the current energy production from solar energy is only 0.008TW.[1] Although the potential of using solar energy as the energy source is enormous, a big issue is the low efficiency of conversion and storage of solar energy at present because the worldwide energy demand does not correlate with the availability of sunlight. Artificial photosynthesis provides us with an alternative way to utilize solar energy like green plants to not only harvest energy but also store energy in the form of fuels.[2] For example, “Photocatalytic water splitting” is a method of converting and storing solar energy directly to hydrogen where photocatalysts absorb the light and generate electron-hole pair for H_2 and O_2 evolution. Photocatalytic water splitting is very attractive for several reasons. 1) This type of solar energy conversion alleviates the energy storage problem, since hydrogen can be stored much more efficiently than either electricity or heat. 2) Hydrogen is valuable as a potential fuel and energy carrier. It is non-polluting, renewable, inexhaustible, and very flexible concerning conversion to other forms of energy (heat via combustion or electricity via fuel cells). 3) Hydrogen is valuable in its own right as a primary chemical feedstock used in large

quantities for ammonia synthesis and petroleum refining. Since the primary current source of hydrogen is the steam reforming of natural gas, a new process based on water and sunlight would be an important advance[3].

1.1.1 Metal-based vs polymer photocatalysts

Mimicking the Photosystem II (PS II) in natural photosynthesis, semiconductors with valence band deeper than the water oxidation potential (1.23V vs. RHE, pH=0) could use photo-generated holes to generate O_2 while electrons can reduce water to H_2 if the conduction band is more negative than the water reduction potential (0V vs RHE, pH=0). Substantial studies have been carried out on solar water splitting over the last several decades. In the early 1970s, the TiO_2 electrode was firstly reported to be capable of generating oxygen and hydrogen in a photoelectrochemical (PEC) system.[4] However, TiO_2 can only operate with ultraviolet light, which accounts for a small amount of the incoming solar energy (4%). Therefore, considerable efforts have been put into developing photocatalysts capable of using the less energetic but more abundant visible light, which accounts for about 43% of incoming solar energy. More recently, a lot of visible-light-responsive photocatalysts, have been discovered, modified and showed great potential to water oxidation/reduction, such as doped TiO_2,[5] $BiVO_4$,[6] WO_3,[7] hematite,[8] and Ag_3PO_4[9]. However, the bottleneck of metal oxide photocatalysts is the mismatch between their band edge positions and the water redox potentials. In other word, there is a contradiction between the narrow bandgap which enables the absorption of a wide wavelength range of sunlight and the sufficient band edge for water reduction/oxidation. For example, the valence band of metal oxides mainly consists of O 2p orbit which locates around +3.0 eV vs RHE, while a narrow

bandgap that can absorb light wavelength below 420nm is approximate 3.0 eV, making the conduction band very close to the water reduction potential (0 V vs RHE). Considering that a ca. 0.5 eV overpotential usually needs to be overcome to drive the reaction, most traditional metal oxides are incapable of realising overall water splitting in the visible region. Therefore, other narrow bandgap metal-based photocatalysts with more suitable band positions are developed by introducing elements such as N, S instead of O to alter their valence band, forming GaInN, TaON, CdS. Although, the involvement of N and S up-shifts the valence band effectively, materials' stability appears to be a critical problem mainly due to the self-corrosion of sulfide or nitride materials under strong light irradiation. Despite intensive studies in exploring the potential of metal-based photocatalysts in photosynthesis, the difficulty in altering the band edges of metal-based photocatalysts limits their current applications.

Polymer photocatalysts have drawn intense attention since graphitic carbon nitride (g-C_3N_4) has firstly seen its water cleavage potential in 2009,[10] because of its excellent light adsorption in the visible light region (wavelength > 400nm), tuneable band structure, facile synthesis process, chemical and thermal stability, environmental benignity and earth abundance. The valence band of g-C_3N_4 mainly contributed by N 2p orbital locates around +1.7 eV vs RHE, while its conduction band mainly dominated by C 2p orbital sits around -1.0 eV vs RHE. Such a negative conduction band position, superior visible light absorption and outstanding chemical stability make g-C_3N_4 one of the most promising polymer photocatalysts, especially for H_2 production from water, evidenced by over 16000 articles in the last decade. Due to its flexible band structure covering the H_2 reduction potential ($E_{H2/H}^{+}$ = 0 eV) and O_2 production potential ($E_{O2/H2O}$ = 1.23

eV), even pure water splitting has been observed in carbon quantum dots (CQD) loaded g-C_3N_4 with a remarkable overall solar energy conversion efficiency of 2% (the reproducibility of this result is challenging).[11] Given the solar energy conversion efficiency in natural photosynthesis is mainly around 0.5%, g-C_3N_4 has proved a great potential to make the artificial photosynthesis more efficient than the natural system. More importantly, the conjugated polymer structure of g-C_3N_4 makes its band structure more tuneable than traditional metal-based semiconductors, which allows the valence band and conduction band to be easily adjusted by heteroatoms doping, defects introducing or structure distortion. It encourages the production of a library of polymer photocatalysts for more extensive applications in photosynthesis.

1.1.2 Suspension vs photoelectrochemical (PEC) system

Generally, there are two systems currently being used for photo-driven water splitting: a particle suspension system and a photoelectrochemical (PEC) system. In a particle suspension system, photocatalysts particles are dispersed in an aqueous solution usually with vigorous stirring to ensure uniform irradiation on the particles. The advantage of a suspension system is that photo-generated electron-hole pairs usually have a very short distance (depending on the particle size) to diffuse, making the "charge transport step" for photosynthesis short and leading to a high photocatalytic performance. However, the disadvantages are: 1) adjacent photo-generated electrons and holes tend to recombine unless an efficient co-catalyst is present, such as Pt for g-C_3N_4; 2) produced H_2 and O_2 are mixed in the same reactor, which will cause the back reaction, safety issue and high operational cost to separate the gases. In a PEC system, photoelectrodes are made by depositing photocatalysts onto

a substrate. When light is irradiating onto the electrode, because of the band bending effect in a non-intrinsic semiconductor, photo-generated electrons are driven to one electrode for reduction reaction, and holes accumulate on the other electrode for the oxidation reaction. The advantages of a PEC system are: 1) photo-generated electrons and holes are well separated, suggesting mitigated charge recombination and separated products; 2) photoelectrodes can be assembled into smart devices or scaled up for industry use very easily; 3) most importantly, multiple electrochemical techniques can be performed on photoelectrodes to understand the electron dynamics in a material to help further improve its performance, which can hardly be achieved in a particle suspension system. The main challenges of a PEC system lie on: 1) the complicated recipe to fabricate high-quality photoelectrode; 2) the demand for directional charge transport requires a long charge diffusion length in photoelectrodes.

1.2 Motivation, aims and objectives

To date, remarkable success of g-C_3N_4 in visible light driven water splitting has only been achieved in the particle suspension system. However, its application in a PEC system has rarely been investigated and the few reports show very limit photocurrent which is controversy to its performance in a particle suspension system. Therefore an in-depth investigation to g-C_3N_4 photoelectrodes is very crucial for both its fundamental undemanding and practical applications.

With great motivation to implant the success of g-C_3N_4 in a suspension system to a PEC system and more importantly to take the advantages of a PEC system

to investigate the relationships between its charge dynamics and PEC performance, this project aims to demonstrate facile strategies to fabricate low-cost, metal-free, efficient polymer films as highly efficient photoelectrodes and to develop a comprehensive understanding of charge dynamics in these photoelectrodes. However, there are several challenges existing, such as 1) minimal reports on high-quality g-C_3N_4 films fabrication; 2) scarce experience in charge dynamic study of g-C_3N_4 photoelectrode in this field; 3) much more inefficient charge transfer in a polymer film than in powder. A few objectives are promoted to overcome these barriers step by step towards high-efficient polymer photoelectrodes.

The key objectives include:

1) Developing facile methods for high-quality g-C_3N_4 films/photoelectrodes fabrication;

2) Investigating the key factors dominating the PEC performance of g-C_3N_4 photoelectrode by charge dynamics study;

3) Improving its PEC performance as an efficient photoanode basing on the comprehensive understanding of charge dynamics;

4) Exploring its potential as a PEC photocathode and understanding the mechanism.

A high-quality g-C_3N_4 film is not only of great interest in PEC photosynthesis but also can be extended to the area of the solar fuel cell, polymer batteries, catalysis supports etc.

1.3 Structure of the thesis

There will be seven chapters in this thesis, focusing on fabricating and investigation of high-quality g-C_3N_4 polymer photoelectrode for photosynthesis. Chapter 1 briefly introduces the background, motivations and aims of this project; Chapter 2 reviews remarkable achievements of g-C_3N_4 in photosynthesis, along with existing charge dynamic studies. Chapter 3 introduces the methods for film fabrication and characterizations. In Chapter 4, high-quality g-C_3N_4 film was synthesised by a rapid thermal condensation method. The critical factor dominating the PEC performance of the g-C_3N_4 film was investigated. Chapter 5 demonstrates a novel strategy of fabricating a B-doped CN / bulk-g-C_3N_4 nanojunction as an efficient photoanode. Chapter 6 reveals a strategy of altering the PEC behavior of g-C_3N_4 between photocathode and photoanode. The last chapter summarizes the principal conclusions and proposes future work.

2 Literature review

2.1 Semiconductors and water splitting

2.1.1 Semiconductors and bandgap

Semiconductors are materials which have a lower conductivity than metals but higher conductivity than insulators. Semiconductors are more like insulators than metals because, at a low temperature (e.g. 0 K), the semiconductors will transfer to insulators while the metallic conductivity of metals remains almost the same.[12] In this case, the real thing distinguishing semiconductors from metals is the temperature dependence of the conductivity. Semiconductors and insulators have some properties in common, that is the existence of an energy gap between occupied and empty states.

Energy bands can be thought of as a collection of a large number of individual but closely spaced energy levels existing in crystalline materials. The wavefunctions (the minimum energy needed to extract an electron from the metal equals $q\ \theta_M$, where θ_M is the wavefunction, q is the electron charge) of an individual electron overlap with those of electrons confined to neighboring atoms. The Pauli Exclusion Principle does not allow the electron energy levels to be the same in the same molecule so that a set of closely spaced energy levels are combined, forming an energy band. For example, the effect of a periodic arrangement on the electron energy levels in a carbon crystal with the atoms arranged in a face-centered cubic (FCC) structure (diamond) is illustrated in **Fig. 1**. Energy levels are plotted as a function of the lattice constant (a). When the distance between two atoms is large enough (the lattice constant of

the crystal is infinite), the energy levels of carbon atoms are isolated and decided by 2p and 2s orbitals. As the lattice constant is reduced, the wavefunction of electrons **Fig. 1** overlap due to the interactions with other adjacent atoms. As a result, the energy levels split according to Pauli Exclusion Principle to form energy bands, such as 2s band (containing 2N states) and 2p band (containing 6N states), where N is the number of atoms in the crystal. A further reduction of the lattice constant causes the 2s and 2p energy bands to merge and split again into two bands containing 4N states each.[13] At 0 K, the lower band filled with 4N electrons is the valence band and the upper band is empty labelled as the conduction band. In a polymer semiconductor, such as g-C_3N_4, its crystal structure can be easily distorted due to the flexibility of a polymer structure, which will result in a change of the lattice constant and thereby a change of its band structure. It makes the band position in g-C_3N_4 adjustable. Apart from band positions shift, heteroatoms in g-C_3N_4 usually narrows the bandgap by creating impurity energy levels between bandgaps. A combination of structure distortion and heteroatoms doping strategies makes g-C_3N_4 a promising photocatalyst with flexible band structure. The heteroatoms doping strategy will be discussed in the next section.

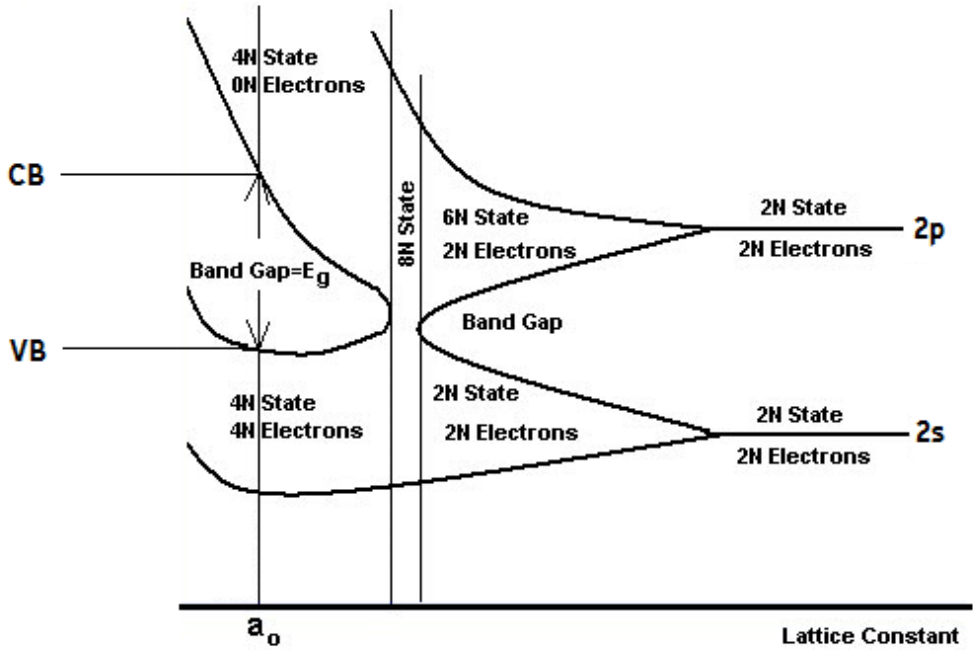

Fig. 1 Electron energy levels in a carbon crystal (diamond) reproduced from reference[13]

2.1.2 Intrinsic and extrinsic semiconductors

Intrinsic semiconductors are insulators at 0 K, because the valence bands are fully filled with electrons and no electron exists in the conduction band. A typical intrinsic semiconductor is Silicon. At room temperature, despite electrons in silicon's valence band can be thermally excited, the amount of generated charge carrier is orders of magnitude lower than that in a conductor. For example, the thermally excited electron density in the pure silicon is $1.5*10^{10}/cm^{-3}$ at 298k, compared with the charge carrier density of $10^{28}/cm^{-3}$ in a metallic conductor.[14] Such a small amount of electron density results in a high electrical resistivity of silicon at room temperature. However, the charge carrier density of intrinsic semiconductors can be easily changed by doping impurity atoms. The impurity-doped semiconductors are named extrinsic

semiconductors. A very tiny amount of impurity atoms can significantly improve the conductivity of semiconductors (e.g. n-type and p-type doped silicon).[15]

Silicon has four valence electrons for each atom. Doping arsenic (As) into silicon will introduce one additional valence electron into the semiconductor as each As atom has five valence electrons (**Fig. 2**a). These extra electrons are weakly bonded to their parent atoms and can be easily promoted to the conduction band. Energy levels of these extra electrons (donor levels) are formed just below the conduction band, as shown in **Fig. 3**. The dotted line represents the existence of additional electrons which may be easily excited into the conduction band. Semiconductors that have been doped in this way will have a surplus of electrons, and are called n-type semiconductors. In such semiconductors, electrons are the majority carriers. Conversely, if a group III element, such as boron (B), is used to substitute for some of the atoms in silicon, there will be a deficit in the number of valence electrons in the material (**Fig. 3**b). This substitution introduces electron-accepting levels just above the top of the valence band and causes more holes to be introduced into the valence band. Hence, the majority of charge carriers are positive holes in this case. Semiconductors doped in this way are termed p-type semiconductors.

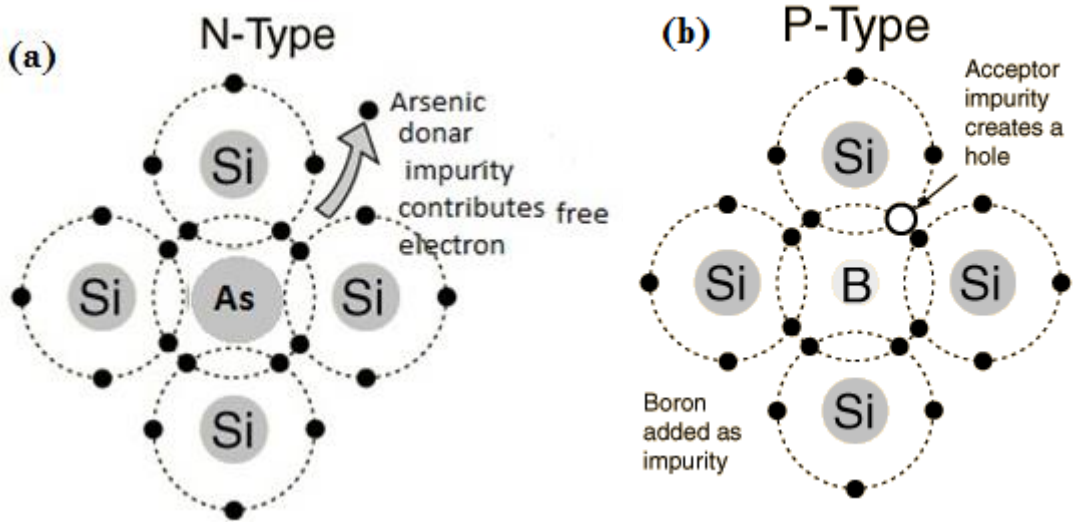

Fig. 2 Extrinsic semiconductors: (a) As doped n-type silicon and (b) B doped p-type silicon.

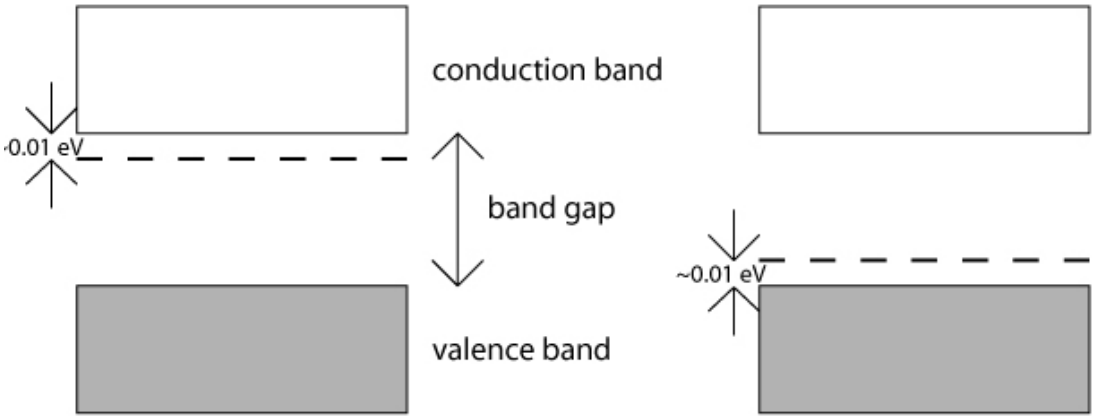

Fig. 3 Donor level formed by dopants in extrinsic semiconductors

In doped semiconductors, the activation energy for electrons to be donated or accepted by impurity states is usually so low that at room temperature, the concentration of majority charge carriers is similar to the level of impurities. A direct consequence of heteroatoms doping is the improvement of conductivity of materials due to improved charge carrier density, such as Phosphorus doped g-C_3N_4.[16] Especially in a PEC system where directional charge transport is vital,

heteroatoms doping is a crucial strategy to enhance the charge transfer in the film and therefore improve the PEC performance of a photoelectrode.

2.1.3 Band bending and Space charge layer

When a semiconductor is brought into contact with metal, another semiconductor or an electrolyte, a band bending occurs and the space charge layer forms.[17] Band bending refers to the local changes in the energy levels of semiconductors' band structure near a semiconductor-metal or semiconductor-electrolyte junction, due to space charge effects. Band bending is significant as it determines the direction of charge transport in a semiconductor.

Metal-semiconductor Junction

Band bending occurs as a result of different work functions (ϕ_{work}) or Fermi level between two materials. Fermi level can be defined as the highest energy state occupied by electrons in a material at absolute zero temperature. In an intrinsic semiconductor, the Fermi level sits in the middle of the bandgap. In a p-type semiconductor, there is an increase in the density of unfilled states; thus more electrons can be accommodated at lower energy states. The fermi level is near the valence band. In an n-type semiconductor, electrons locate at higher energy states, and the Fermi level is near the conduction band.

Schottky and Ohmic contacts can occur between a metal and a semiconductor (a metal/n-type semiconductor contact is displayed in **Fig. 4**). When contacted, the Fermi levels of the two materials must match. If the work function of a metal (ϕ_m) is larger than that of an n-type semiconductor (ϕs), the electrons in the n-type semiconductor can lower their energy by moving from the semiconductor into the metal. It causes a slightly negative charging of the

metal, thereby repelling further flow of electrons from the conduction band of the semiconductor into the metal. The Fermi-level in the semiconductor also falls along with band structure, as higher energy electrons have flowed into the metal. Since the band positions at the surface are fixed due to existence of surface states, downshifted fermi-level in bulk generated by charging the metal causes an upward bending of the energy bands in the semiconductor close to the metal-semiconductor interface. The Fermi level of the metal is not affected because there are much more electrons in the metal than in the conduction band of semiconductors. This is Schottky contact. The immediate consequence of making Schottky contact with the metal is that a region near to the metal-semiconductor interface is produced in the semiconductor which has no conduction electrons in it -- this region is depleted of electrons in the conduction band, therefore, called the “depletion layer”, or the “space charge region”. The depletion layer acts as a potential barrier to stop electrons further flow to the metal.

In contrast, if $\phi m < \phi s$, an accumulation layer forms at the interface due to the electrons transfer from metal to semiconductor. The band is bending downward, creating an Ohmic contact. An Ohmic contact has an unimpeded transfer of electrons from semiconductor to metal which is more favorable than a Schottky contact.

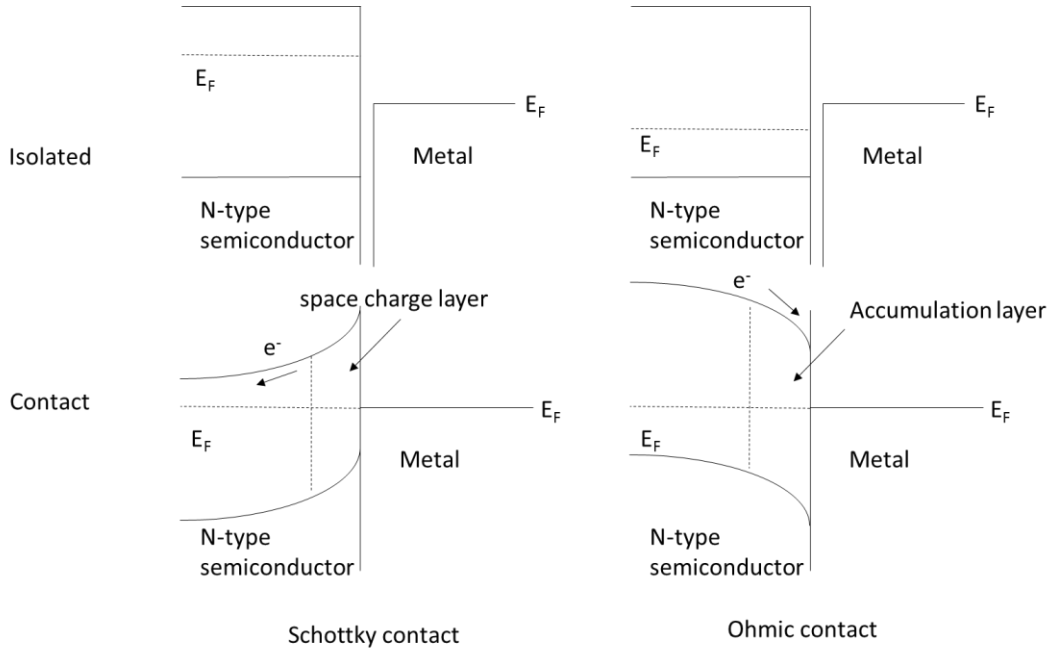

Fig. 4 Energy band diagrams of metal and n-type semiconductor contacts

Fermi level pinning

Surface states exist due to the termination of lattice periodicity at the surface, resulting in unsaturated bonds (also known as dangling bonds), which can rearrange themselves or might be saturated by a layer of atoms, sometimes oxygen.[18] The energies of these states usually locate inside the bandgap. Surface states can act as donors or acceptors. When the density of surface states is very high (e.g. 1 state per surface atom), the Fermi level becomes "pinned' at surface state energy. In other word, the Fermi level is fixed at the peak of surface states energy level regardless of the doping density in bulk. Taking an n-type semiconductor as an example in **Fig. 5**, the Fermi level of a doped n-type semiconductor free of surface states is determined by the dopant density, while energy levels of surface states only decide the Fermi level of an n-type semiconductor with a high surface state density. The peak of energy levels of surface states is usually lower than the E_F in an n-type semiconductor.

Excessive electrons flow into the surface states from the bulk, resulting in an upward band bending and a nature depletion layer. For p-type semiconductor where E_F is close to the VB, a downward band bending occurs as holes flow into the surface states and form an accumulation layer.

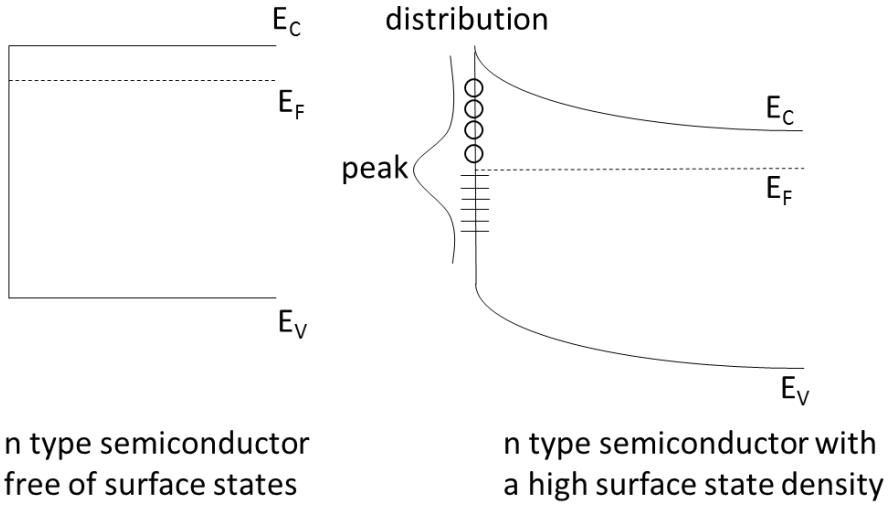

Fig. 5 Scheme of band bending caused by fermi level pinning

2.1.4 Semiconductors for water splitting in a suspension system

A significant amount of energy is required for water splitting ($H_2O \rightarrow H_2 + 0.5\ O_2$, ΔG_0= 237.13 kJ/mol). Photo-assist water splitting by means of a semiconductor provides us with a more sustainable way to do that, such process is denoted photocatalysis. Semiconductors with an appropriate bandgap are thermodynamically suitable for photocatalysis. Theoretically, the minimum bandgap for water splitting is 1.23 eV, corresponding to a wavelength of around 1100 nm. The relationship between these two values can be represented by the equation 1[19]: *Bandgap (eV) = 1240/λ (nm)* (Equation 1); λ is the wavelength of light. To realize the water splitting, the bottom of the conduction band of

semiconductor should be more negative than the potential of H^+/H_2 (0 eV, RHE) and the top of valence band should be more positive than the potential of O_2/H_2O (1.23 eV, RHE). The electrons in the conduction band will reduce H^+ to produce hydrogen, while holes left in the valence band can oxidize O^{2-} to produce oxygen. Kinetically, an extra potential needs to be overcome to realize water splitting, making the required bandgap larger than 1.23 eV. The mechanism for this photocatalysis process contains three steps and is illustrated in **Fig. 6**. 1) A light with equal or larger energy than the bandgap can be absorbed by the semiconductors to produce electron-hole pairs in the particles. 2) The electron-hole pairs will move to the particle surface. 3) On the surface, electrons can react with electron acceptors, and holes can oxidize the donor species. In a suspension system, charge migration from the bulk to the surface (step 2) is usually not a big concern because the short distance for charge transport in a particle always allows sufficient electron-holes pairs to reach the material/solution interface. However, light absorption and electron-hole generation (step 1) is the most important because it determines the maximum solar energy conversion efficiency of a material, thereby encouraging intensive studies to explore semiconductors with suitable band positions.

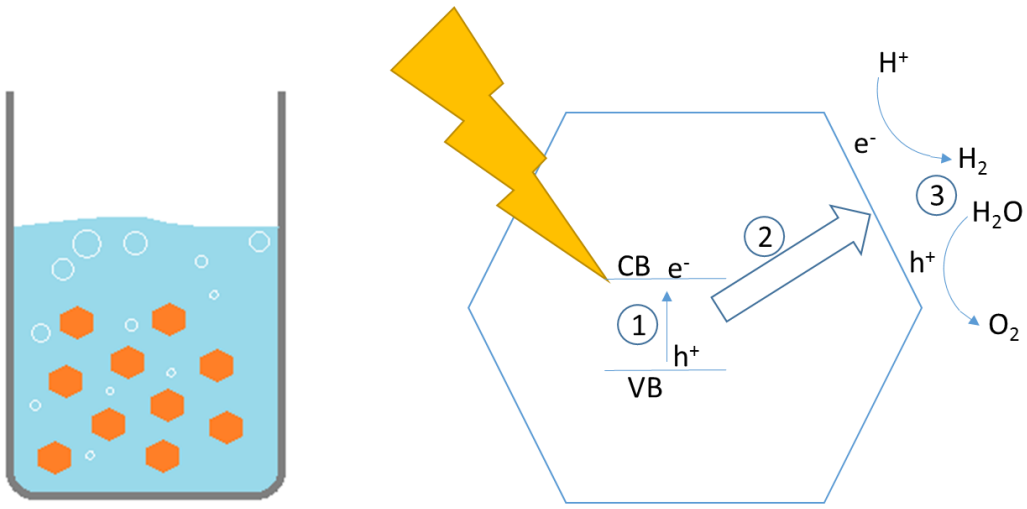

Fig. 6 Mechanisms for the photocatalysis process in a particle suspension system

Taking TiO_2 as an example, the studies of TiO_2 in photocatalytic application started from the 1970s. As a low cost, non-toxic and photochemical stable semiconductor, TiO_2 received intensive attention and became vital in lots of fundamental studies of photocatalysis. The application of TiO_2 is not only restricted to water splitting but organic degradation, carbon dioxide conversion and other photocatalytic reaction[20]. However, the wide bandgap of TiO_2 (3.2 eV for anatase and 3.0 eV for rutile[21]) limits its light absorption. Only the UV light can be utilized by TiO_2, which accounts for a small part of the solar spectrum. A theoretical solar to hydrogen efficiency (STH) is as low as 1.3% and 2.2% for anatase and rutile[22], respectively and a practical STH efficiency is less than 1%[23]. In an energy distribution within a solar spectrum, ultraviolet light (< 400nm) accounts for only 4% of solar energy reaching our planet, while the percentages of visible light (400 nm – 700 nm) and infrared light (> 700nm) are 43% and 53%, respectively. A narrow bandgap (smaller than 3.0 V) is favourable for visible-light-driven water splitting. To explore TiO_2 as a visible-light-driven

photocatalyst, substantial work has been performed on modifying properties of TiO_2, such as doping carbon[24], nitrogen[25], and Fluorine[26] to change its band position. For water oxidation application, TiO_2 has an exceedingly deep band position of +3.0 eV, which is formed by O 2p orbital. Doping impurities to replace oxygen atoms forms a new valence band and reduces the bandgap. Strategies used to manipulate the conduction band of TiO_2 includes doping metal atoms such as Ta[27], Nb[28].

There are also a few of narrow-bandgap semiconductors whose band edges allow overall water splitting, such as Ge_3N_4[29], Ta_3N_5,[30] TaON,[31] CdS,[32] CdSe[33] and g-C_3N_4[10]. However, the efficiency is moderate such as the average apparent quantum efficiency of $(Ga_{1-x}Zn_x)(N_{1-x}O_x)$ in the range of 300-480 nm was only 0.14%.[34] Some of them are suffering from self-photo-corrosion, such as nitrides and sulphides. G-C_3N_4 has been reported for overall water splitting, such as Pt/Co_3O_4-g-C_3N_4 with an apparent quantum yield (AQY) for overall water splitting of 0.3% at 405nm and long stability over 510 h;[35] and carbon quantum dots (CQD) loaded g-C_3N_4 has obtained an overall solar energy conversion efficiency of 2.0%.[36]

2.2 PEC system

Honda and co-workers[37-40] in the early 1970s firstly pointed out the potential application of PEC systems for solar energy conversion and storage. Fujishima & Honda, using illuminated n-type semiconducting titanium dioxide anodes, showed that the oxidation of water to oxygen could be achieved at a significantly more negative potential compared to the standard redox potential of the H_2O/O_2 redox couple. Fujishima & Honda called this effect

"photosensitized electrolytic oxidation," and suggested that it could be applied to splitting water into hydrogen and oxygen using sunlight. This process is now generally known as photoelectrolysis.

2.2.1 PEC configuration

A PEC cell usually contains a working electrode (WE), a counter electrode (CE) and an optional reference electrode (RE) and is shown in **Fig. 7** schematically. As illustrated, photon absorption of a semiconductor electrode generates hole-electron pairs in a region in semiconductors which light can penetrate. With the help of an external electronic circuitry, electrons are driven to the metal counter electrode via a metal wire, leaving holes accumulating on the surface layer of semiconductor anodes. In this sense, holes and electrons are efficiently separated. Oxidation and reduction reaction occurs at the working electrode and counter electrode, respectively.

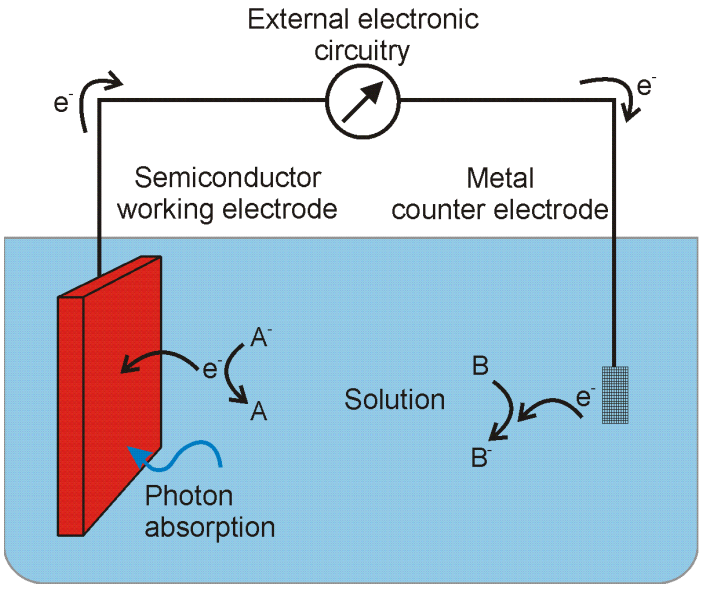

Fig. 7 The configuration of PEC cells

The selection of a CE is important to ensure that the reaction kinetics at the CE does not limit reaction occurring at the working electrode. For n-type

semiconductors, the large surface area of Pt foil or Pt net is a good option because of its excellent catalytic activity in reducing H^+ into H_2. However, for p-type semiconductors, RuO_2 and IrO_2 are better counter electrode candidates for water oxidation reaction than Pt as they can reduce over-potentials more effectively[41]. Since Pt, RuO_2 and IrO_2 are all expensive metals, the development of low-cost metal catalysts for HER and OER is desired for cost-effective PEC water splitting. REs are required in PEC measurement to measure the potential of the working electrode (WE) on a defined electrochemical scale, typically versus the normal hydrogen electrode (RHE). Regular REs includes saturated calomel electrodes (SCE, E_{SCE} = +0.241 V vs. RHE, 25°C), silver-silver chloride in saturated KCl (Ag/AgCl, $E_{Ag/AgCl}$ = +0.197 V vs. RHE, 25°C) and Hg/HgO reference electrode ($E_{Hg/HgO}$ = +0.097 V vs. RHE, 25°C). The SCE and Ag/AgCl reference electrodes can be used in a wide range of pH values, while Hg/HgO reference electrode is preferred in basic solution.

2.2.2 Electrode/electrolyte interface

All phenomena associated with the photoelectrochemical system are based on the formation of a semiconductor-electrolyte junction. A space charge layer (SCL) develops in the semiconductor adjacent to the interface with the electrolyte, due to the equilibrium between two phases with different chemical potentials. For semiconductors, the chemical potential of electrons is given by the Fermi level in the semiconductor. For liquid electrolytes, it is determined by the redox potential of the redox couples present in the electrolyte.

The band bending at the electrode/electrolyte interface is shown in **Fig. 8**. When semiconductor is brought into contact with an electrolyte that contains a redox couple (acceptors A and donors A^-), a difference in potential (between

Fermi energy in semiconductor E_F and the Nernst potential of the redox pair of donor/acceptor $E_{A/A-)}$ is introduced. Electrons will flow between the semiconductor and the solution until equilibrium is established. Charge transfer results in an interfacial electric field, where electrostatic potential balances the initial difference in electrochemical potentials between the solution and semiconductor. After equilibration, the electrochemical potential (Fermi level) is the same everywhere. The conductivity even of doped semiconductors is usually well below that of an electrolyte solution; so practically potential drop occurs in the boundary layer of the electrode and very little on the solution side of the interface.

For a typical n-type semiconductor photoanode in equilibrium with a redox species in solution (e.g., O_2/H_2O), the electrode will have excess positive charges, and the solution will have excess negative charges. The positive charges are spread out over the depletion layer in the semiconductor, whereas the negative charges spread over a much narrower region (the Helmholtz layer) in solution, close to the electrode. An n-type semiconductor is traditionally used as a photoanode because the electric field that develops in equilibrium with a redox couple results in band bending that directs photogenerated free minority charge carriers (holes, for n-type semiconductors) to move into the solution. P-type semiconducting electrodes behave analogously, except that the ionized dopants are negatively charged and the solution is positively charged. Therefore, p-type semiconductors favor electron flow into the positively charged acceptor species at the interface.

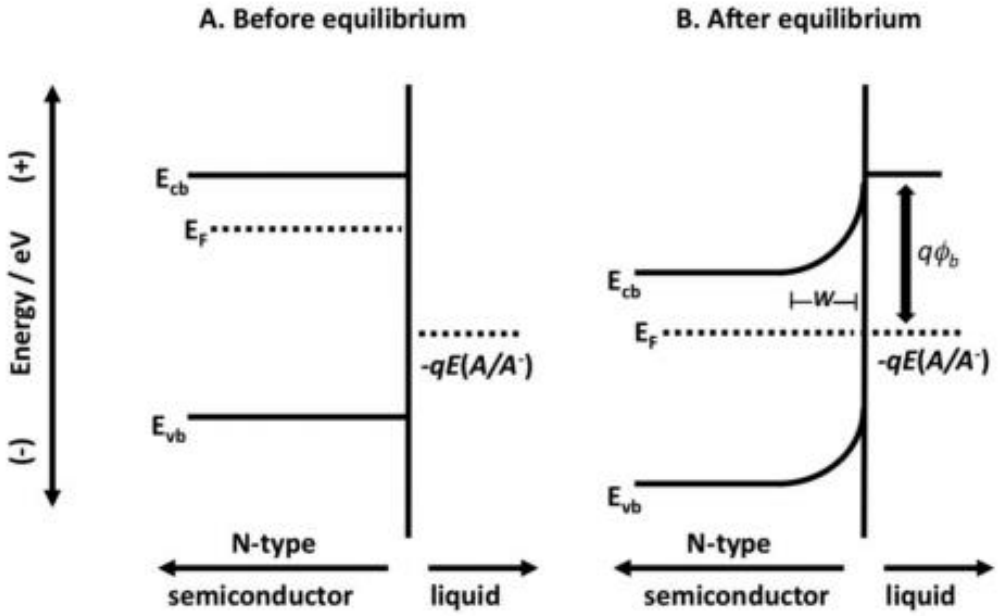

Fig. 8 The band bending at the semiconductor-electrolyte interface. Reproduced from the reference[42]

2.2.3 Electrode/electrolyte interface under illumination

In dark condition, equilibrium achieves when the rate of thermal charge generation of electron-hole pairs equals to that of electron-hole pairs recombination. When the electrode/electrolyte junction is illuminated with light (**Fig. 9**), photons having energy larger than E_{gap} (the bandgap of semiconductors) are absorbed and create electron-hole pairs in the semiconductors. Photons absorbed in the depletion layer produce electron-hole pairs that separate under the influence of the electric field present in the space charge region. Electron-hole pairs produced by absorption of photons beyond the depletion layer will separate if the minority carriers can diffuse to the depletion layer before recombination with majority carriers occurs.

As discussed earlier, a potential barrier exists in the space charge layer which tends to separate the photogenerated electron-hole pairs in such a way

that excess majority carriers move toward the bulk while the excess minority carriers are swept to the surface where they are subsequently injected into the electrolyte to drive a redox reaction. For n-type semiconductors, minority holes are injected to the electrolyte for an anodic oxidation reaction, while minority electrons are driven to the counter electrode for a cathodic reduction reaction. The photogenerated majority carriers in both cases are swept toward the semiconductor bulk, where they subsequently leave the semiconductor via ohmic contact, traverse an external circuit to the counter electrode and are then injected at the counter electrode to raise a redox reaction inverse to that happening at the semiconductor electrode. The production and subsequent separation of photogenerated electron-hole pairs in the depletion layer force the Fermi level in the semiconductor back toward its original position (before contact).

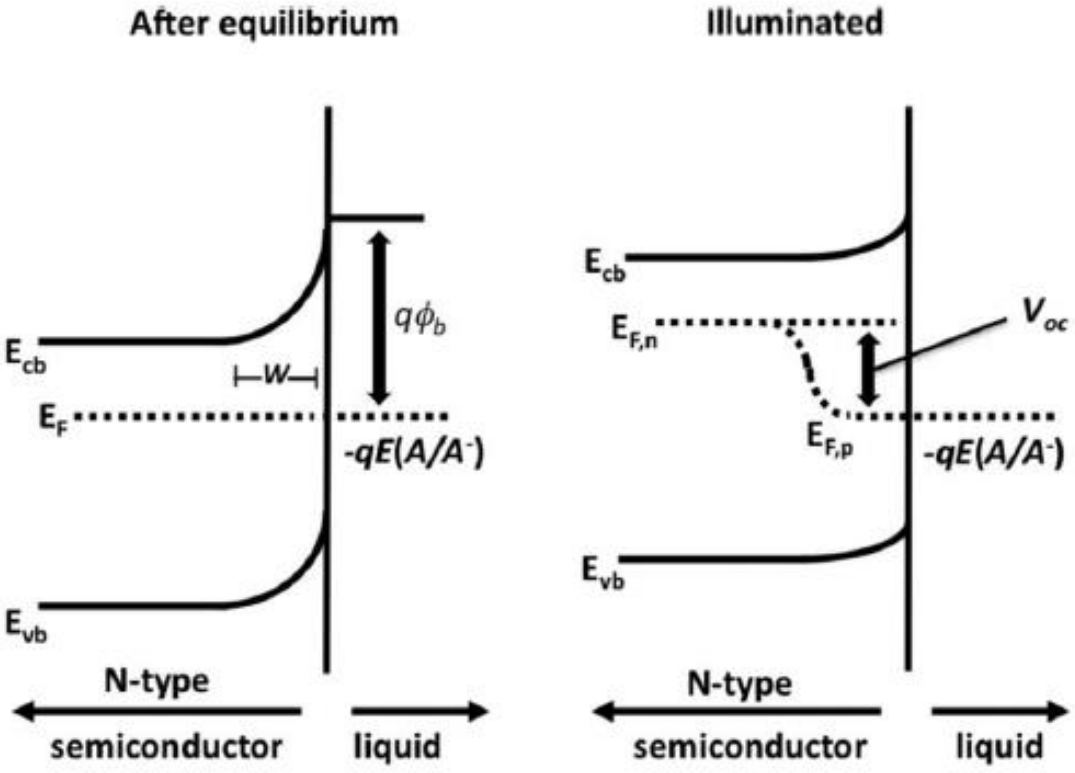

Fig. 9 Band bending at semiconductor/electrolyte interface under illumination condition, reproduced from the reference[42]

2.2.4 Nanostructure of the electrode

The nanostructure of a semiconductor electrode is favorable in an efficient PEC cell, as it allows the electrolyte to easily diffuse within materials' network, increasing the contact area between the electrolyte and electrode and shortening the hole diffusion distance[43]. However, band bending condition near the electrode-electrolyte interface can be different.

Debye length is defined as a scale over which charge carriers screen out an electric field in plasma physics. In other word, significant charge separation occurs within Debye distance. In a semiconductor where band bending happens at material/electrolyte interface, Debye length can be calculated by equation 2:

$$L_D = \left(\frac{\varepsilon \varepsilon_0 k_B T}{2q^2 N} \right)^{1/2} \quad \text{(Equation 2)}$$

where N is the dopant concentration, ε_0 is the permittivity of free space (ε_0=8.854 × 10^{-12} F·m^{-1}), ε is the dielectric of semiconductors, K_B is the Boltzmann's constant, q is the electron charge.

In a nanostructure semiconductor electrode, if particles have a smaller size than Debye length, band bending will become insignificant, and complete depletion of charge carriers occurs. An example of band bending in a nanostructure semiconductor particle is illustrated in **Fig. 10**. The potential distribution (equation 3) was derived by Albery and Bartlett[44].

$$\phi(r) = \frac{r^2 qN}{3\varepsilon\varepsilon_0}$$ (Equation 3)

From the equation, a smaller radius of particles results in smaller band bending. Giving a doping density of 10^{17} cm^{-3} and a relative permittivity of 30, a 20 nm fully depleted anatase particle exhibit a 2 mV band bending while the maximum band bending of a 50 nm diameter particle is 13 mV.

Higher band bending can be obtained by increasing the doping density. Increase the doping density in anatase particle results in one order of magnitude increase of band bending. In this sense, detectable band bending can be created by heavily doping semiconductors to separate charge carriers.

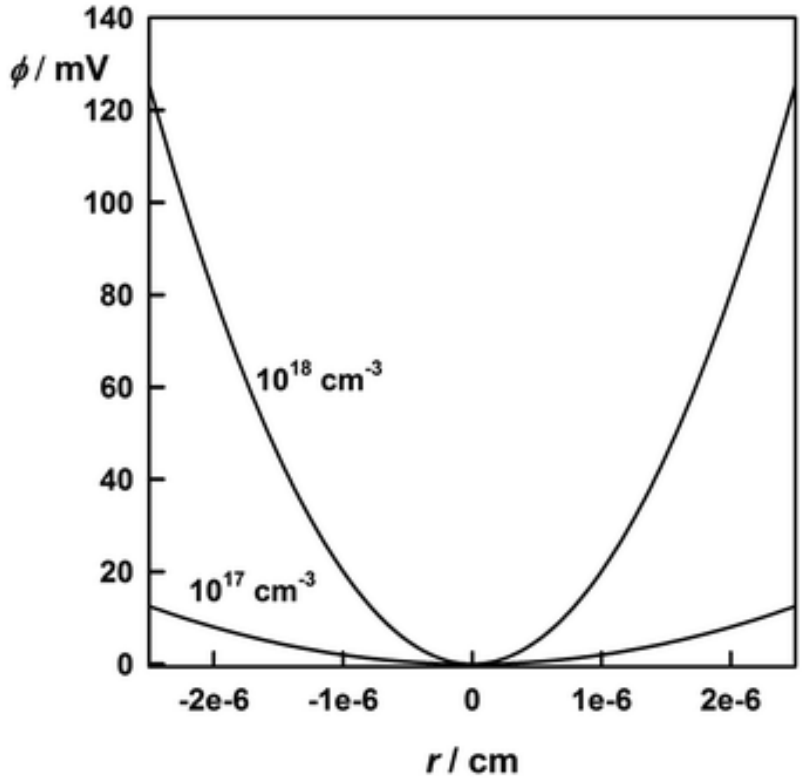

Fig. 10 Band bending for complete depletion in spherical anatase particles with different doping densities (r = 25 nm, ε = 30, doping density as shown). Reproduced from reference[45].

2.2.5 The band diagram of a PEC cell

After the discussion of band bending in semiconductors in an electrolyte, an overall energy diagram of a PEC cell, taking an n-type semiconductor as an example, is illustrated in this section (**Fig. 11**).

As a result of electrode/electrolyte junction, a charged layer known as Helmholtz layer also exists in the electrolyte adjacent to the electrode/electrolyte interface. This layer consists of charged ions from the electrolyte adsorbed on the solid electrode surface, which have the opposite sign to the charge induced in the solid electrode (space charge layer). As shown in **Fig. 11**, there is a potential drop over the Helmholtz layer, because the inner Helmholtz layer (the thin layer near the semiconductor) contains lots of negative ions while the outer Helmholtz layer (the layer away from the semiconductor) contains many positive ions. The existence of the potential drop over the Helmholtz layer can affect the band structure. For metal oxide, the band structure will shift by 0.059 V per pH value due to the absorption of protons and hydroxide ions on the semiconductor surface which also changes the potential drop over Helmholtz layer by 0.059 V per pH value.[46] Without the Helmholtz layer, the band bending would equal the difference in initial Fermi levels between the two phases.

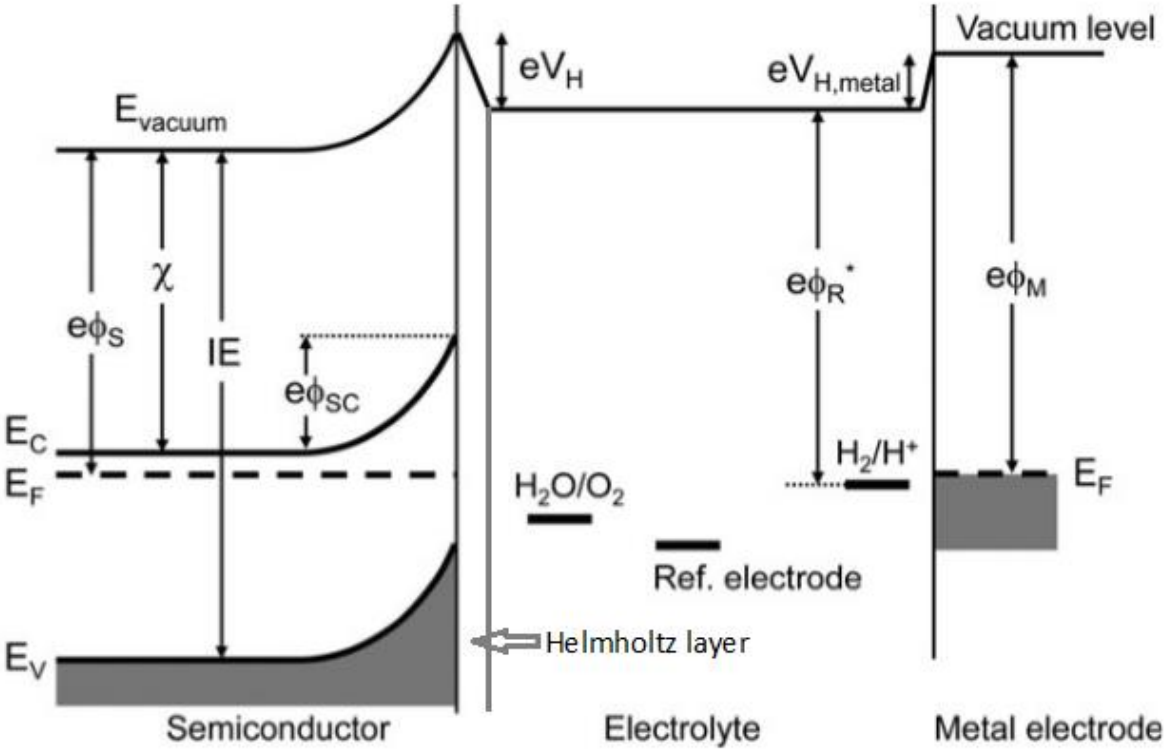

Fig. 11 Energy diagram for a PEC cell based on an n-type semiconductor and a metal counter electrode; the vacuum energy level is taken as a reference, reproduced from reference[46].

2.2.6 Applying Bias Potential

The band diagram can be considerably influenced by applying an external bias potential in a PEC system. As illustrated in **Fig. 12**, when the bias is applied to a RE, the potential difference will be distributed over the space charge layer and the Helmholtz layer (Equation 4). These layers act as two capacitances in series[47].

$$\frac{1}{C_{total}} = \frac{1}{C_{SC}} + \frac{1}{C_H} \quad \text{(Equation 4)}$$

Since space charge layer contains the same charge Q with Helmholtz layer (the amount of negative ions in Helmholtz layer equals to the positive charge in

space charge layer), the potentials over space charge layer (ΔV_{SC}) and Helmholtz layer (ΔV_H) are given by the equation 5:

$$\frac{\Delta V_{SC}}{\Delta V C_H} = \frac{C_H}{C_{SC}} \quad \text{(Equation 5)}$$

Fig. 12 illustrates the effect of applying a positive/negative bias voltage (VA) to an n-type semiconductor electrode more precisely. Since $C_H >> C_{SC}$, any change in applied potential falls across the space charge layer, whereas V_H remains constant[48]. When a positive potential is applied to the semiconductor electrode, ΔV_{SC} becomes larger, and the depletion layer becomes significant, while a sufficiently negative applied bias can remove the band bending.

Using external bias to change the band bending in a semiconductor electrode is a quite useful technique to characterize semiconductors. Properties such as the flat banding position of materials can be determined from this technique, which will be discussed later.

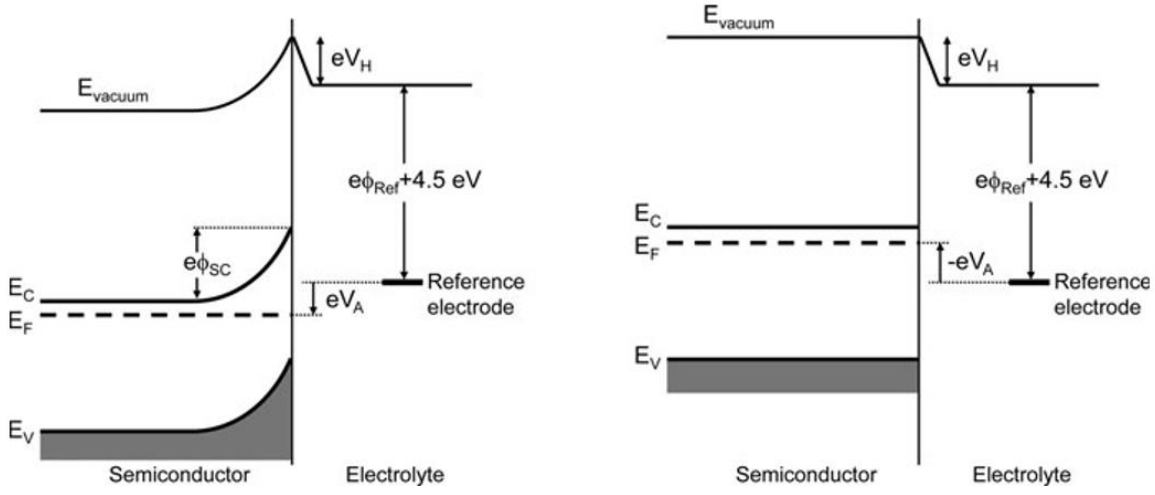

Fig. 12 Effect of applying a positive (left) and negative (right) bias voltage (V_A) to an n-type semiconductor electrode. Reproduced from reference[49].

2.2.7 PEC water splitting

Fig. 13 shows a scheme of a PEC water splitting cell used an n-type semiconductor and a metal as a working electrode and counter electrode, respectively. Water splitting reaction is an uphill reaction, which requires minimum Gibbs free energy of 237 KJ/mol. Therefore, the overall water splitting reaction can be expressed as equation 6, and the potential difference (ΔV) between water oxidation and reduction reaction is 1.23 V.

$2H_2O = 2H_2 + O_2$, ΔG=237 kJ/mol (Equation 6)

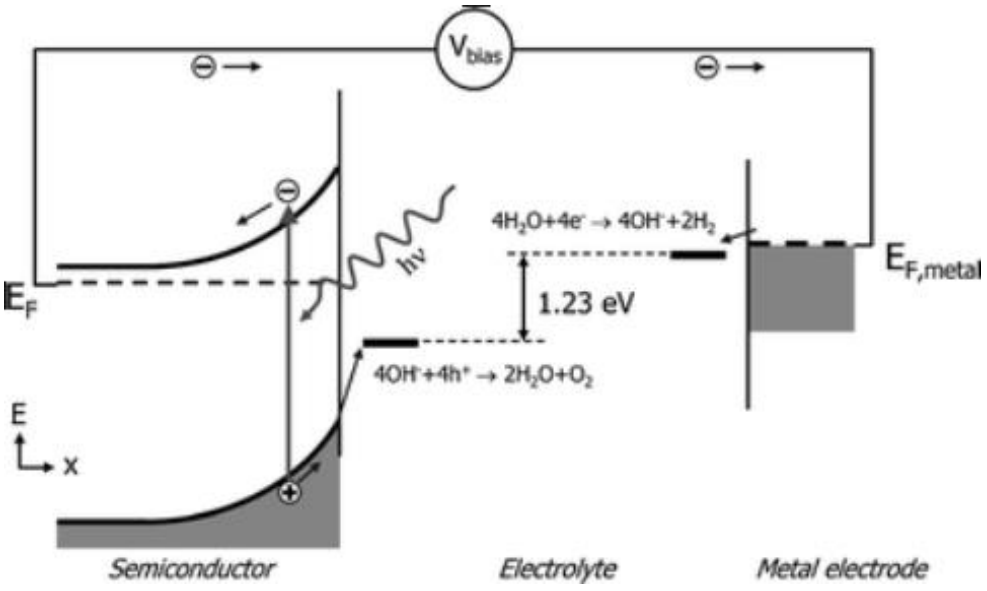

Fig. 13 Schematic diagram of a PEC cell, reproduced from reference[50]

A complete PEC water splitting reaction contains three processes. The first process is light absorption from a light source (simulated one sun -- 100mW/cm^2) to generate electron-hole pairs in the semiconductor. Upon illumination, electron-hole pairs are generated in bulk. Ideally, as long as the bandgap of the semiconductor straddle two lines of the redox potential of H^+/H_2 (0 V vs RHE) and O_2/H_2O (+1.23V vs RHE), the photo-generated charge carriers allow water oxidation reaction at semiconductor surface and water

reduction reaction at the counter electrode surface. In other words, the valence band (VB) potential must have more positive potential than 1.23 V (vs RHE) and the conduction band (CB) potential must have more negative potential than 0 V (vs RHE). However, in reality, extra overpotential is needed due to the energy loss while hole passing through the surface charge region and electron transferring through external circuits to counter electrode (e.g. Platinum). The second process is the separation and transportation of photo-generated electron-hole pairs. At this step, charge carries can either recombine in bulk or at the surface and hence an efficient separation and high mobility of charge carries is desired. The last process is the surface reaction, where the redox reaction occurs. Both potential of the charge carriers and reaction kinetics are crucial for an efficient water-splitting reaction.

Efficiencies

The efficiency of each steps limits the overall Solar to Hydrogen efficiency (STH) of a PEC water-splitting cell. Therefore, the STH efficiency can be expressed as equation 7, where η_{abs}, η_{Sep}, η_{cat} are light absorption, charge separation and catalytic efficiency.

$$\eta_{STH}=\eta_{abs}\eta_{Sep}\eta_{cat} \quad \text{(Equation 7)}$$

STH efficiency can also be defined as the ratio of total energy generated and total energy input by sunlight illumination (equation 8):

$$\eta_{STH}=\text{Total energy generated / Total energy input}= \Delta G \times R_{H2} / P \times A \quad \text{(Equation 8)}$$

Where ΔG is the Gibbs free energy (237 KJ/mol); R_{H2} is the rate of Hydrogen production in mole/s; P is the light intensity (100 mW/cm^2), and A (cm^2) is the illuminated area of the photoelectrode.

However, in most cases, equation 9 is used to calculate the STH in a PEC cell

$\eta_{STH}=J_{ph}\,(V_{redox}-V_{bias})\,/\,P_{light}\times\eta_{faraday}$ (Equation 9)

Where J_{ph} is the photocurrent density, V redox is the redox potential for water splitting (1.23 V vs RHE); V bias is the applied bias added between the working electrode and reference electrode; P light is light intensity (100 mW/cm^2); $\eta_{faraday}$ is the faraday efficiency. J_{ph} is the generated photocurrent density.

Quantum efficiencies such as incident photon-to-current conversion efficiency (IPCE) and absorbed photon-to-current conversion efficiency (APCE) are often used to identify performance-limiting factors in PEC cell. The IPCE is the fraction of the incident photons that are converted to electrons (equation 10).

IPCE (λ) = Total energy of converted electrons / Total energy of incident photons $= \frac{\frac{J}{e}*\frac{hc}{\lambda}}{P} * \mathbf{100}\%$ (Equation 10)

Where J is the photocurrent density in the particular wavelength of incident light (mA/cm^2); e is the electric charge of one electron (1.602 *10^{-19} C); h is the Planck constant (6.626 *10^{-34} J·s); C is the speed of the light (3.0*10^8 m/s); λ is the wavelength of the incident light (m); P is the incident light power at that wavelength (mW/cm^2).

In IPCE, optical losses such as reflection and transmission are involved. To correct these optical losses, absorbed photon-to-current conversion efficiency (APCE) is often used to define the quantum efficiency, which is called internal quantum efficiency and can be expressed as equation 11:

APCE (λ) =$IPCE$ (λ)/ A (λ)=$IPCE$ (λ)/(1−R−T)*100% (Equation 11)

Where A, R, T are the optical absorption, refection, and transmission, respectively.

Faraday efficiency (equation 12) is the only way to prove that the photocurrent is due to the PEC water splitting rather than photo-corrosion of the electrodes. It is the ratio of experimental gas evolved to the theoretical gas evolved based on the measured photocurrent.

Faraday efficiency = Oxygen evolution measured / Gas evolution based on the photocurrent = $n_{O2} * 4e / [(J_{photo} * A * t) / N_A] * 100\%$ (Equation12)

Where n_{O2} is the mole amount of measured oxygen (mol); J_{photo} is the photocurrent density (A/cm^2) generated during the measurement time period (h) ; A is the illumination area of photoelectrode (cm^2); t is the time (s); e is the electric charge of one electron ($1.602 *10^{-19}$ C); N_A is the Avogadro constant ($6.02*10^{23}$ mol^{-1}).

2.2.8 Photoelectrolysis configuration and strategies

The wide bandgap of semiconductors limits the application of a single material for unbiased water splitting. For example, semiconductors such as SrTiO3 (3.2eV)[51] and $KaTO_3$ (3.5eV)[52] have large enough band to generate sufficient photovoltage for water splitting. However, the poor light absorption in the visible-light region leads to low STH efficiency of them. Narrow bandgap semiconductors have more efficient light absorption, therefore, possessing a higher theoretical STH value. The insufficient band potential of narrow bandgap semiconductors can be compensated by an external bias in a PEC system. In this single light absorber PEC system, overall water splitting can be obtained at the cost of electricity supply, which is not favorable for renewable energy source

development. There are some strategies for developing scalable and economical unbiased photo-assist water-splitting devices.

Z-scheme PEC devices

To harvest the solar spectrum more efficiently, a z-scheme PEC device is designed by combining two semiconductors with different energy levels. In such a configuration (**Fig. 14**), electron-hole pairs generate at both semiconductors. Water is oxidized by holes in the valance band of an n-type semiconductor, while electrons in the conduction band of a p-type semiconductor transfer to the surface to do water reduction reaction. The substrate between n-type and p-type semiconductors acts as a conductive layer to transfer electrons between two semiconductors. It is worth noticing that electrons can recombine with holes before they transfer to the other semiconductor. The reverse reaction competes with water splitting, whose effect should be minimized.

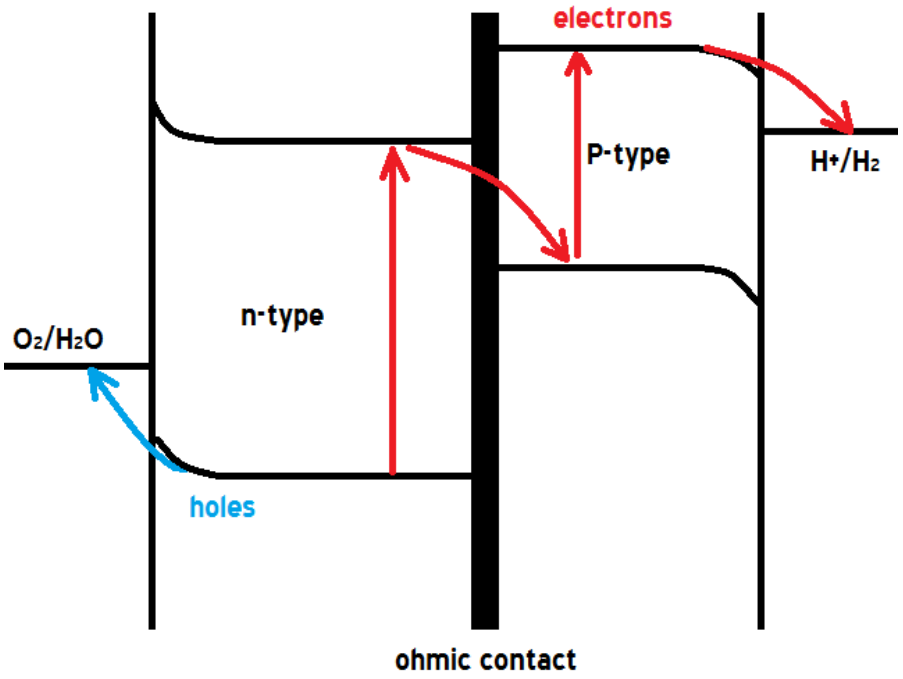

Fig. 14 Configuration of Z-scheme PEC device

This configuration has the advantage of excellent light absorption, but the challenge is achieving efficient charge transfer between two semiconductors and suppressing the reverse reactions[53].

Successful Z-scheme pure water splitting device was firstly reported by Domen and Co-workers[53]. They synthesised a Z-scheme device by embedding $SrTiO_3$:La,Rh and Mo-doped $BiVO_4$ powders into a gold layer. An apparent quantum yield of over 30% at 419 nm was obtained for the resulting device, along with a 1.1% STH efficiency. The gold layer acts as a conductive substrate, allowing electrons to transfer freely between semiconductors. A further work reported by the same group utilized carbon sheet to substitute the gold layer[54]. The conductive carbon sheet was proved to be a better substrate for charge transfer.

Integrated PEC-photovoltaic cell (PV)

J. Turner and co-workers reported a direct water electrolysis system based on an integrated photoelectrochemical PEC/PV device[55]. A schematic diagram of the PEC/PV cell is shown in **Fig. 15**. P-$GaInP_2$ was used as the photocathode due to its sufficient conduction band potential to reduce water. A p-GaAs/n-GaAs PV cell was connected to a $GaInP_2$ top cell through a tunnel diode interconnect. The p-n junction provided an extra voltage to help oxidize water. The $GaInP_2$ layer with a bandgap of 1.83 eV was used for visible light absorption, while p-n junction (1.42 eV bandgap) can absorb the near-infrared portion of the sun spectrum transmitted through the $GaInP_2$ layer. This PEC-PV cell generates one electron in an external circuit by consuming two photons. It is essential to match the photon absorption characteristics to maximum the efficiency of each material.

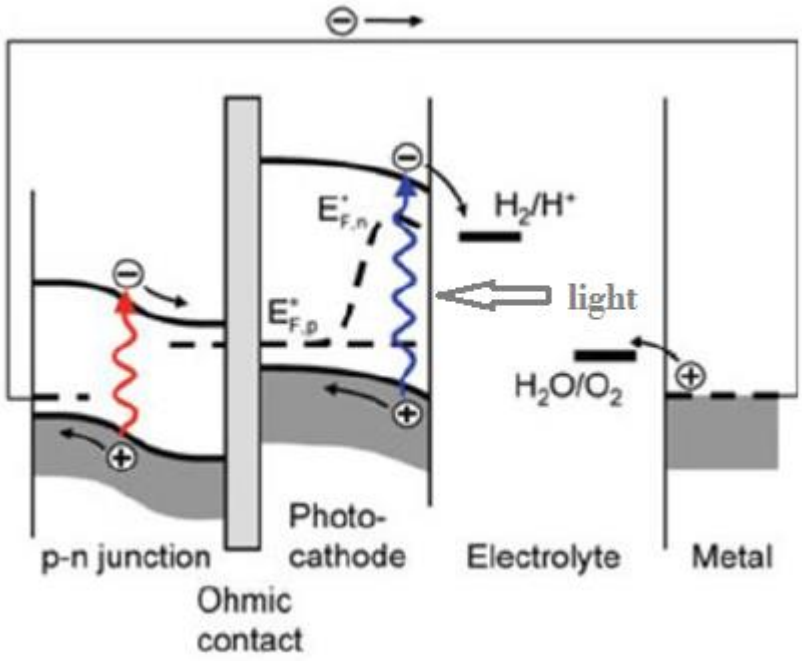

Fig. 15 PV-PEC devices based on a photoanode, reproduced from reference[56]

In summary, the configuration of a PEC cell consists of a photoelectrode, a metal counter electrode and a reference electrode. Band bending occurs in a semiconductor when it contacts with the electrolyte due to their different Fermi levels. Several factors influencing the band bending are summarized, including pH change, illumination condition and nanostructure design of electrodes. Band diagram of PEC cells illustrates the effect of Helmholtz layer and space charge layer on band bending. Thermodynamic and kinetic requirements for PEC overall water splitting are stated. Different strategies of optimizing PEC configuration are summarized to realize pure water splitting, such Z-scheme PEC design, the monolithic PEC-PV cell and tandem cell.

2.3 g-C_3N_4 based powder photocatalysts for photosynthesis

Nowadays, photo-assist water splitting with polymer semiconductors, represented by graphic carbon nitride (g-C_3N_4, in fact, it should be $C_3N_xH_y$ as many protons are incorporated in the commonly prepared carbon nitride samples[57]), becomes increasingly popular. Compared with metal oxides, g-C_3N_4 has advantages of simple composition, facile synthesis, low cost and earth abundance[58]. As an analogue of graphite, g-C_3N_4 has layer structures consisting of C-N bond rich tri-s-triazine rings, which had been proposed as the basic building blocks of g-C_3N_4[59]. The tri-*s*-triazine rings are cross-linked by trigonal nitrogen atoms to form extended networks, as seen in **Fig. 16**. The high degree of condensation of tri-*s*-triazine ring structure results in an appealing electronic structure as well as thermal and chemical stability[60].

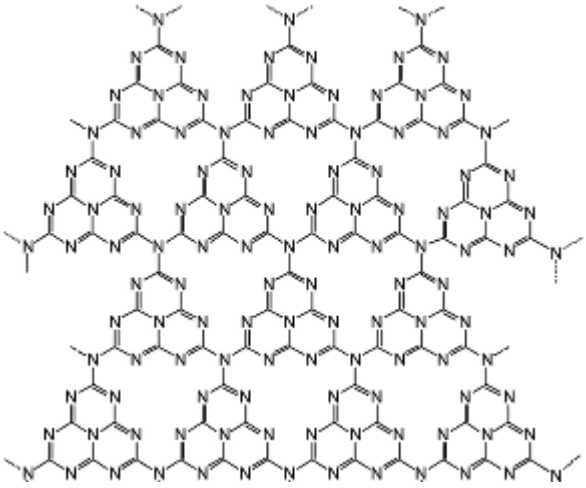

Fig. 16 Structure of graphite carbon nitride (g-C_3N_4)

G-C_3N_4 is an indirect semiconductor with a medium bandgap of *ca.* 2.7 eV. The conductive band (CB) and valence band (VB) positions are, respectively, at

ca. −0.85 eV and *ca.* +1.85 eV *vs.* reversible hydrogen electrodes (RHEs), underlying its potential use for visible-light-driven water splitting. However, the band position is flexible, depending on preparation methods. In g-C_3N_4 synthesis, different precursors or condensation temperatures result in different local structure or defects in g-C_3N_4, which may influence its absorption edge[10]. For example, sulfur-doped carbon nitride leads to a blue-shift of the adsorption edge[61], while boron and fluorine doping result in a red-shift of the adsorption edge[62]. G-C_3N_4 has excellent thermal stability which is better than most organic materials. The thermal decompose temperature of g-C_3N_4 is above 600°C, and complete decomposition of carbon nitrides occurs up to 750 °C[63]. The thermal stability of g-C_3N_4 would be slightly different in terms of various preparation procedures, which is caused by the varying degrees of condensation. The excellent chemical stability against acid corrosion was also revealed in the study of other properties. Zhang and coworkers found out that the dispersion of g-C_3N_4 in strong acid could form a true solution[64]. The recovered material g-C_3N_4 from acid solution still possessed a predominant (002) peak in the X-ray diffraction spectrum, indicating that g-C_3N_4 could easily restack. In addition, g-C_3N_4 nanosheets or single-layered quantum dots in neutral water were usually negatively charged (with a zeta potential of around −40 mV).[65-66] The highly negative surface charge endowed the stable suspension of g-C_3N_4 nanostructures in aqueous solution, which could standstill for several weeks without aggregation or precipitation.

2.3.1 g-C_3N_4 based powder photocatalysts for H_2 production half-production

Efficient water reduction into hydrogen can be realized by loading a small weight percentage of co-catalyst (such as 3 wt% Pt) on g-C_3N_4 in the presence of suitable sacrificial reagent such as TEOA. The role of Pt is usually recognized as the co-catalyst to reduce the overpotential of hydrogen reduction. As the hydrogen evolution efficiency of bulk g-CN is initially low, strategies, investigated to improve its quantum efficiency, mainly focus on elements doping, structure optimization, and bandgap engineering.

Heteroatoms doping

'Structural doping' strategy has been applied in g-C_3N_4 to improve its visible light absorbance and enhance its conductivity. Effective heteroatoms doping in g-C_3N_4 includes P, B, F, S, O etc. For example, phosphorous heteroatoms were doped in g-C_3N_4 in carbon sites using a mild phosphorus source (1-butyl-3-methyl-imidazolium hexafluorophosphate) showed 4 orders of magnitude enhancement of conductivity due to significantly increased charge carrier density[16]. Phosphorous doping also introduced a color change of g-C_3N_4 from yellow to brown and a narrowed bandgap due to distorted lattice of g-C_3N_4, resulting into an AQY of 5.68% at 420nm.[67] Oxygen doping into the linker between heptazine chains by substituting N atoms could extend the light absorption of g-C_3N_4 to near-IR region (λ=800nm) and increase the charge separation efficiently, resulting in an AQY of 10.3% at 420nm and 2.1% at 500nm.[68] Treating fresh g-C_3N_4 in a gaseous H_2S atmosphere leaded to the substitution of sulfur for lattice nitrogen[61]. An increased valence bandwidth in combination with a high conduction band minimum and a slightly reduced

absorbance leads to *ca.* 8 times higher H_2 evolution rate than g-C_3N_4 under λ> 420nm. Sulfur could also substitute carbon in mesoporous g-C_3N_4 by directly calcining thiourea, which exhibited enhanced and extended light absorbance in the visible light region and a much lower density of defects compared to the native g-C_3N_4, leading to 30 times higher hydrogen evolution rate than the native g-C_3N_4[69].

Structure optimization

Structure optimization strategies include increasing the polymerization degree[70], building porous structure[71], expanding g-C_3N_4 stacking layers into nanosheets[72] and so on. All these methods could effectively enhance the H_2 evolution efficiency of bulk g-C_3N_4. For example, a careful control of polymerization degree of g-C_3N_4 has increased the H_2 evolution efficiency dramatically with an AQY of 26 % at 400nm due to a pronounced negative shift of conduction band position and enhanced charge separation determined by DFT calcultion.[70] However, as-synthesised g-C_3N_4 bulk material usually has a minimal surface area (generally less than 10m^2g^{-1}) which allowed limited actives sites to be exposed to reactants. Introducing porosity at the nanoscale in g-C_3N_4 is an attractive strategy to enlarge the surface area, which could explore its potential to be highly active photocatalysts[63]. The synthesis of mesoporous g-C_3N_4 could be obtained by using hard or soft template.[73-74] The resulting g-C_3N_4 yellow powder showed a flexible surface area from 86 m^2g^{-1} to 439 m^2g^{-1}. Apart from the large surface area, porous g-C_3N_4 could also introduce shallow trap states by structure distortion and, therefore, increase the electron lifetime and promote H_2 evolution rate by 17 times than bulk g-C_3N_4.[72] Another strategy to enlarge the surface area of g-C_3N_4 was preparing the bulk material into

nanosheets. G-C_3N_4 has a layered structure which is highly possible to form graphene nanosheets because of the weak van der Waals forces between layers. P Liu *et al*. synthesised 2 nm-thick g-C_3N_4 nanosheets via a thermal oxidation etching of carbon nitride in air[72]. Remarkably, photocatalytic hydrogen generation and OH radical generation of g-C_3N_4 nanosheets have been improved due to the high specific surface area ($306 m^2 g^{-1}$), improved conductivity along the in-plane direction and prolonged photogenerated charge carriers lifetime.

Other strategies

A series of different strategies have been applied to modify the g-C_3N_4, such as coordinating g-C_3N_4 with metal cations to induce metal-to-ligand charge transfer[75]; loading carbon quantum dots as sensitizers to extend the light absorption to vis-NIR region[76]; changing the surface properties of g-C_3N_4 using K_2HPO_4 to enhance charge separation[77]; introducing cyanamide groups by KSCN treatment to promote fast in-situ electron transfer[78] and so on. The highest AQY achieved in g-C_3N_4 was 60% at 420nm by treating urea-derived g-C_3N_4 with molten salts, which has been believed to modify the polymerization pathway of g-C_3N_4 and leaded to well-developed donor-acceptor structure[79]. As a summary, **Table 1** lists the most efficient strategies for g-C_3N_4 modifications for H_2 evolution in a suspension system.

Table 1 Hydrogen evolution efficiency of high-performance g-C_3N_4 photocatalysts

strategies	methods	Bandgap	HER [µmol h^{-1}	QY	Light source	Surface area m^2	ref

			g^{-1}]			g^{-1}	
doping	Linker O-doping	1.5	1020	10.3%@420nm; 2.1%@500nm	300W Xe, λ >420nm	32.9	[68]
	Linker O-doping	1.9	772	8.6%@420nm; 2.5%@500nm	300W Xe, 710nm>λ >420nm	12.1	[80]
	I doping	2.69	760	2.4%@420nm	300W Xe	23	[81]
	S-doping, Nitrogen vacancies	2.5	1210	NA	300W Xe, λ >420nm	72.8	[82]
	S-doping	2.85	~750	NA	300W Xe, λ >420nm	63	[61]
	P-doping	2.69-2.84	506	NA	300W Xe, λ>420nm		[83]
	Br doping	2.82	480	NA	300W Xe	54	[84]
	O-doping	2.49	375	NA	300W Xe, λ >420nm	47	[85]
	F doping	2.63	~130	NA	500W HBO, λ >420nm	38	[62]
Structure optimization	Polymerization degree control	2.85	3327.5	26.5%@400nm	300W Xe, λ >395nm	43.8	[86]
	Crystalline	2.1	8160	15%@400nm	300W Xe, λ >420nm	93	[87]
	Nanoshe	2.8	5222	11.3%@405nm	300W Xe,	210	[88]

	ets				λ >420nm		
	Crystalline nanosheet	NA	1060	8.57%@420nm	λ >420nm	203	[89]
	Nanosheets	2.65	1860	3.75%@420nm	300W Xe, λ >420nm	384	[90]
	Crystalline nanosheet	2.2	1750	1.3%@400nm	300W Xe, λ >420nm	NA	[91]
	Porous	2.73	590	NA	300W Xe	69.6	[92]
	Nanosheets	2.97	660	NA	300W Xe, λ >400nm	306	[93]
Doping + Structure optimization	O-doping, Porous network	2.61	1204	7.8%@420nm	300W Xe, >420nm	36.1	[94]
	S doping, mesoporous	2.61	1360	5.8%@440nm	300W Xe, >420nm	128.4	[69]
	P-doping, Micro-nanostructure	2.5	670	5.68%@420nm	300W Xe, λ >420nm	22.95	[95]
	P-doping, nanosheet	2.91	1596	3.56%@420nm	300W Xe, λ >400nm	122.6	[96]

	O-doping, 2D porous	2.95	3786	NA	300W Xe, >400nm	109	[97]
	B-doping, nanostructure	2.83	5560	NA	300W Xe, λ >420nm	144	[98]
Others	Salts Post-calcination	2.6	11720	60%@420nm	LED, >420nm	74	[99]
	Co-condensation	2.6	3000	57%@420nm	LED, >420nm	85	[100]
	phosphorylation	2.6	18940	45.7%@380nm; 26.1%@420nm	300W Xe, λ >400nm	NA	[101]
	Metal-to-ligand coordination	1.8	604.9	NA	300W Xe, λ >400nm	NA	[102]

2.3.2 g-C_3N_4 based powder photocatalysts for overall water splitting

In theory, the suitable band structure of g-C_3N_4 (CB=-0.85eV, VB=+1.85eV) is thermodynamically favorable for overall water splitting. However, very few reports have claimed successful overall water splitting on single g-C_3N_4

because the oxygen evolution side is very challenging. In kinetics, oxygen evolution reaction is much slower than hydrogen generation from the water because it involves 4 holes ($4OH^- + 4h^+ = 2H_2O + O_2$) while only 2 electrons are needed for H_2 generation ($2H^+ + 2e^- = H_2$). Also, a large driving force for water oxidation is required, which is not fully satisfied by the valence band of g-C_3N_4. Suitable co-catalysts are usually loaded to lower the activation energy to enhance the water oxidation efficiency. For example, RuO_x,[103] Co_3O_4,[104] $Co(OH)_2$[96] have been proved to assist water oxidation of g-C_3N_4 in the presence of sacrificial scavenger. However, the progress of oxygen production from water by polymer photocatalysts is much lags behind H_2 production. For example, the AQY of Co_3O_4-g-C_3N_4 water oxidation was only 1.1% at 420 nm in the presence of a $AgNO_3$ electron scavenger.[105] Overall water splitting was also realized by loading suitable co-catalysts on g-C_3N_4. For example, Pt and CoO_x were found to be excellent H_2 and O_2 photocatalysts that could decrease the activation energy barrier and accelerate the reaction kinetics of the g-C_3N_4 polymers, leading to an AQY of 0.3% at 405 nm.[35, 103] Also, g-C_3N_4 loaded only with Pt was found to produce H_2 and H_2O_2 because the four-hole process (O_2 generation) was less kinetically favorable than two-hole process (H_2O_2 generation).[106] To date, the highest efficiency for g-C_3N_4 water splitting is using CQD to facilitate charge separation and decompose generated H_2O_2 to O_2.[36] In this way, the step-wise two-hole pathway allowed the water cleavage more easily than the four-hole process, which claimed an excellent STH of 2%. However, such an important achievement still needs to be repeated in other laboratories around the world. Apart from g-C_3N_4, other conjugated polymer photocatalysts have also been found active for overall water splitting. For

example, 1,3−diyne−linked conjugated microporous polymer nanosheets (CMPN) exhibited an AQYs of 10.3% for overall water splitting at 420nm, with a total STH of 0.6%.[107] A summary of polymer photocatalysts for overall water splitting is listed in **Table 2** as well as remarkable inorganic photocatalysts.

Table 2 Overall water splitting by polymer photocatalysts.

Materials		H_2 co-catalyst	O_2 co-catalyst	AQY	STH	ref
g-C_3N_4		/	CQD	16%@420nm, 6.29%@580nm, 4.42%@600nm	2%	[36]
CMPN		/	/	10.3%@420nm	0.6%	[107]
In plane g-C_3N_4		Pt	Pt	5%@420nm	/	[108]
g-C_3N_4		Pt, PtO_x	CoO	0.3%@405nm	/	[35, 109]
3D g-C_3N_4		Pt	IrO_2	1.4%@420nm	/	[110]
ZrO_2/TaON	WO_3	Pt	Pt	6.3%@420nm	/	[111]
$SrTiO_3$:La/Rh	Au(carbon)/Mo-$BiVO_4$	Ru	/	30%@419nm	1.1%	[112-113]
g-C_3N_4	Fe_2O_3/rGO	Pt	/	/	/	[114]
g-C_3N_4	BiVO4/WO3	Pt	Pt	/	/	[115]

2.4 g-C_3N_4 based film photoelectrodes for photosynthesis

Low cost and efficient polymer semiconductors are desired for scalable and economic photo-assist fuel synthesis. Since great achievements have been made on artificial photosynthesis by g-C_3N_4 powders, fabrication of g-C_3N_4 film becomes crucial to bring its favorable properties and performance into practice. Making a film out of g-C_3N_4 enables the separated generation of hydrogen and oxygen in a water-splitting system which is difficult for a particle suspension system. However, the development of polymer photoelectrodes or devices is still at their early stage due to challenges in polymer film fabrications and limited understanding of charge transfer in a polymer film.

2.4.1 Synthesis strategies

An ideal way to prepare a film out of powder is to place the as-synthesised g-C_3N_4 powder on the desired substrate by drop coating or spinning coating techniques, followed by the sintering process. However, it is difficult to obtain uniform, repeatable, robust and orientated thin film with these techniques, resulting in the unsatisfactory photocatalytic performance of final devices. Other physical techniques such as pulsed laser deposition or spurting are qualified for high-quality thin film synthesis. However, this technology requires special precursor for oxide film synthesis, which is not suitable for g-C_3N_4.. Many researches on g-C_3N_4 film preparation were performed and can be classified into two groups: top-down and bottom-up strategies.

Top-down strategy

A top-down strategy is making the as-synthesised g-C_3N_4 powder into a film, mainly by disperse coating from suspension. The most advantage of a top-down strategy is that the properties of the photocatalysts could be well preserved during the film fabrication process. Also, disperse coating is very facile and cost-effective. The disadvantage of that is poor contact between photocatalysts and substrate, which usually lead to a problematic charge transfer at the material/substrate interface. g-C_3N_4 colloids were used for dispersing coating to make uniform and firm contact. For example, Zhang *et al.* discovered a facile approach to fabricate g-C_3N_4 film directly from as-prepared bulk materials by depositing exfoliated carbon nitride nanosheet in a cellulose membrane by vacuum filtration[116]. A free-standing g-C_3N_4 film could be obtained after dissolving the cellulose membrane template in acetone, which was thought to be transferrable to other conductive substrates. Another approach was dissolving g-C_3N_4 with hot nitric acid (80ºC) to form a stable colloidal suspension, which could be processed into thin-film via a high temperature (300ºC) recrystallization process on a Fluorine doped Tin Oxide (FTO) substrate[117]. The resulting film showed a remarkably enhanced photo-electrochemical performance as a photocathode because the defects and grain boundaries have been dramatically reduced during the recrystallization process. A concentrated sulfuric acid solution has also been found to enable the formation of a colloidal suspension of g-C_3N_4 due to the synergistic protonation and intercalation,[64] which could be a feasible way to synthesise g-C_3N_4 thin film.

Bottom-up strategies (in situ growth of g-C_3N_4 film)

In situ growth of g-C_3N_4 on desired substrates intimates the contact between materials and substrate, which ensures a reliable electrical conductivity of the

devices. Xu *et al.* reported a general liquid-mediated pathway for the growth of continuous polymeric g-C_3N_4 thin films by using of supramolecular complexes that transform to the liquid state before direct thermal condensation into g-C_3N_4 solid films.[118] Typically, precursor powder was placed in a crucible with a substrate at the bottom before it was covered with a lid and heated at 550 °C for 4 h in a nitrogen atmosphere. The resulting films exhibited continuous porous g-C_3N_4 networks on various substrates. The direct synthesis of g-C_3N_4 in a continuous layered architecture on different functional substrates opened new possibilities for the fabrication of many energy-related devices. J Bian *et al*. used a similar strategy to synthesise g-C_3N_4 films with different monomers, leading to a significant improvement of the optical, electronic, and PEC properties[119]. Liu *et al.* developed an economic and facile method to 'print' carbon nitride film onto the substrates via in situ chemical vapor deposition (CVD)[120]. A remarkable photoanode current density of 30.2 μA/cm^2 at 1.23 V_{RHE} was achieved. Due to the regular and periodic structure of the porous template, the as-obtained film could possess a structural color and could be processed as a two-dimensional photonic crystal, adding to the functionality of the film.

2.4.2 Heterojunctions

Single g-C_3N_4 suffers from severe charge recombination, short charge diffusion length and poor charge transfer. The performance of a pristine g-C_3N_4 photoelectrode was quite limited, such as a porous g-C_3N_4 with excellent active surface area only showing a photocurrent density of ~12 μA/cm^2.[121] Heterojunction is a promising strategy for film fabrication to enhance the charge separation dramatically and elongate its charge diffusion, thereby improving its efficiency in fuel synthesis. For example, my work has reported doping boron on

the surface of a compact-g-C_3N_4 to form a B-CN (surface) / CN (bulk) heterojunction. The charge recombination rate has been significantly reduced by the heterojunction with improved charge transfer rate, leading to a remarkable photocurrent density of 103.2 μA/cm^2 at 1.23 V vs RHE under 100 mW/cm^2 solar illumination and an IPCE of 10% at 400nm.[122] Peng *et al*. mixed rGO with highly porous g-C_3N_4 to obtain an extreme long charge diffusion length in the whole film up to 36 μm. A photocurrent density of 72 μA/cm^2 was obtained at 1.23V vs RHE under one sun condition with an IPCE of 5.3% at 400nm. Further adding TEOA as a scavenger boosted the photocurrent density to 660 μA/cm^2 and an IPCE of 60% at 400nm. A total amount of 0.8 mol/g/h H_2 was generated from the PEC cell, proving g-C_3N_4 to be a promising photoelectrode for H_2 generation.[123] More heterojunction designs including g-C_3N_4/TiO_2[124], g-C_3N_4/ZnO[125], g-C_3N_4/Fe_2O_3[126] all showed enhanced charge separation efficiency and boosted PEC performance.

2.4.3 Surface Kinetics

As discussed earlier, water oxidation is the bottleneck of overall water splitting as oxygen evolution is a four-hole process.[127] Co-catalyst loading could reduce the overpotential of oxygen evolution reaction (OER) and supply as active sites, thereby enhancing the OER performance.

Cobalt and nickel inserting into the g-C_3N_4 structure has been found to beneficial for water oxidation by lowering the overpotential, increasing the light absorption and extracting holes, thereby increasing the photocurrent density.[128-129] Metal oxide such as CoO_x, FeOOH, NiOOH loading on the g-C_3N_4 surface have been proved to be more effective in lowering the overpotential and accelerating the interface charge transfer.[130-132] For example, FeOOH was

chosen to be the co-catalyst to help the charge separation on g-C_3N_4 surface, improving its photocurrent density from 89 μA/cm^2 to 122 μA/cm^2 at 1.1 V vs RHE.[131] In situ assembly of N-deficient porous g-C_3N_4 nanosheets and NiFe-layered double hydroxide into a 3D N-doped graphene framework architecture leaded to a high photocurrent density of 162.3 μA/cm^2 at 1.4 V vs RHE, with an IPCE of 2.5% at 350nm.[132]

Table 3 Promising g-C_3N_4 films as photoanodes

strategies	Materials	potential	Photocurrent density μA/cm^2	Light source	IPCE	ref
Pure g-C_3N_4	g-C_3N_4	1.23 vs RHE	63	AM1.5	/	[133]
	g-C_3N_4 nanorods	1.23 vs RHE	30.2	/	/	[134]
	Porous g-C_3N_4	1.23 vs RHE	12	/	/	[121]
	g-C_3N_4	1.55 vs RHE	120 (with Na_2S scavenger)	AM1.5	/	[135]
Heterojunction	g-C_3N_4/Carbon	1.23 vs RHE	100 (with Na_2S scavenger)	AM1.5	16%@400nm	[136]
	B-CN/CN	1.23 vs RHE	103.2	AM1.5	10%@400nm	[122]
	g-C_3N_4/rGO	1.23 vs RHE	72(without scavenger) /660(with TEOA	AM1.5	5.3%@400nm (without scavenger)/ 60%@400nm(	[123]

			scavenger)		with TEOA scavenger)	
	g-C_3N_4/Graphdiyne	0 vs RHE	-98 / -133 (with Pt co-catalyst)	AM1.5	2.6%@365nm	[137]
Co-catalyst	g-C_3N_4/FeOOH	1.1 vs RHE	122	AM1.5	/	[131]
	g-C_3N_4/N-graphene/Ni-FeOOH	1.4 vs RHE/ 1.22 vs RHE	162.3/72.9	AM1.5	2.5%@350nm	[132]
	g-C_3N_4/Ni	1.23 vs RHE	69.8	AM1.5	/	[129]

In summary, **Table 3** lists the most promising g-C_3N_4 films as photoanodes. The photocurrent density is limited within several hundred μA per centimeter square due to 1) poor conductivity; 2) unfavorable water oxidation kinetics. As the 2-D layer structure and delocalized π-bond of g-C_3N_4 theoretically ensure a good electron transport, the poor conductivity could be due to either excessive electron trap defects or low charge carrier density. Reducing the defects and enhancing the doping level in g-C_3N_4 could be solutions. Doping strategies could also alter the band edge of g-C_3N_4, which also helps modify the driving force for water oxidation.

2.5 Charge dynamics in traditional metal oxide and g-C_3N_4

Understanding charge dynamics of materials such as charge lifetime, charge diffusion length, charge recombination rate constant, charge transfer rate constant etc. are critical in improving their PEC performance. Traditional metal oxides such as TiO_2, Fe_2O_3 have been well studied, developed and applied especially in the area of PEC and solar cell. In this chapter, charge dynamics in traditional metal oxide and their influence in photocatalytic performance will be briefed. The charge dynamics in g-C_3N_4, which has rarely been investigated is also considered to guide the development of high-performance polymer photoelectrode.

2.5.1 Traditional metal oxide: TiO_2, α-Fe_2O_3, $BiVO_4$

Charge diffusion length

The charge diffusion length is essential for a high-performance photoelectrode. A long electron diffusion length relative to the film thickness can guarantee the efficient collection of charge in a photoelectrode. The diffusion length of TiO_2 has been determined to be ~10 μm as observed in both the PEC system and the dye-sensitized solar cell[138], which allows a sufficient charge transport across the film with thickness less than 10 μm. Hematite (α-Fe_2O_3) is a promising photo-electrode material due to its long-wavelength light absorption, favorable chemical stability and earth abundance. Hematite has a bandgap of 1.9 - 2.2 eV, which corresponds to a theoretical STH efficiency of 13%[139]. The near-infrared light absorption of hematite is due to d–d transition states between electron energy levels of the Fe^{3+} ion[140]. Although hematite has visible-light

response, its performance as an efficient photoanode is limited by the slow majority charge carriers mobility, fast photoexcited electron-hole pair recombination in the bulk and large overpotential required for photo-assisted water splitting[8]. A comprehensive investigation by Grätzel *et al*. revealed that the critical issue is the short charge diffusion length (~2-4 nm).[43, 141] Typically, the optical penetration depth for visible wavelengths into a-Fe_2O_3 is more than an order of magnitude greater than the width of the space charge region, so that a significant fraction of the photogenerated electron-hole pairs recombine in the bulk of the material. The lifetime of charge carrier is an order of 10 ps due to the fast photo-excited hole electron pairs recombination in the bulk[142]. These problems have been addressed by nanostructures design such as nanostructured, dendrite α-Fe_2O_3 photoelectrode to overcome short diffusion length of holes and to facilitate hole transportation to the surface[143].

Doping strategy is an efficient method to modify the electronic structure, charge lifetime and charge diffusion length in a semiconductor. For example, $BiVO_4$ is an n-type semiconductor, with a direct bandgap of *ca.* 2.4 eV. Theoretically, the maximum photocurrent and STH efficiency of BVO_4 are 7.4 mA/cm^2 and 9.1% respectively[144]. The efficiency of $BiVO_4$ is limited by fast charge carriers recombination due to short electron diffusion length and reduced surface water oxidation kinetics. Mo doped $BiVO_4$ showed a longer electron diffusion length, resulting in insignificant charge carrier recombination in the bulk and higher photocurrent density. The electron diffusion length in Mo-$BiVO_4$ has been determined to be *ca.* 300 nm compared with 10nm in pure $BiVO_4$[144]. An earth-abundant water oxidation electrocatalyst (Co-Pi) was

deposited on W-doped BiVO4 photoanode to get a near-complete suppression of surface recombination[145].

However, high concentration dopants result in a detrimental effect on photocatalytic performance as recombination centers are introduced. To avoid the bulk charge recombination and ensure efficient transfer of charges to the semiconductor surface, surface doping strategies have been developed. For example, V-doped TiO_2 exhibited superior photocatalytic performance when vanadium was only doped on the surface lattice of anatase than in the bulk[146]. High concentrations of the surface charges could promote recombination. Surface V^{3+}/V^{4+} ions could trap charge carriers to reduce the density of the space charges, thereby extending the lifetime of the charge carriers for efficient interfacial transfer. On the contrary, bulk V^{3+}/V^{4+} ions formed in the interstitial anatase lattice inhibited charge diffusion to the surface through deep trapping[146].

Four-hole chemistry

Due to the complex of four-hole chemistry, the kinetics of oxygen evolution reaction (OER) is quite slow. Tang *et al*. found evidence for four-hole chemistry in TiO_2 water oxidation, and determined the photogenerated hole lifetime to be ~1s in TiO_2.[147] Efficient water oxidation co-catalysts were developed to overcome the poor OER kinetics, such as IrO_2[148], Co^{2+}[43] and cobalt-phosphate (CoPi)[149], resulting in a considerable reduction of the photocurrent onset potential. For example, a remarkable photocurrent for hematite (4.32 mA cm^{-2} at 1.23 V vs. RHE) has been achieved by depositing CoPi on a highly crystalline worm-like hematite photoanode.[150] However, even the best OER catalyst leaves a significant overpotential remaining (0.3–0.4V) due to the surface trapping states[151].

2.5.2 Polymer photocatalyst g-C_3N_4

Investigation on charge dynamics of g-C_3N_4 is inadequate compared with traditional metal oxide photocatalysts. G-C_3N_4 has a 2-D layer structure with a delocalized giant π-bond, which should allow fast in-plane electron transport. However, the g-C_3N_4 has suffered from its poor conductivity, especially for g-C_3N_4 electrodes, leading to limited PEC performance. The reasons could be 1) there are too many deep trap states acting as recombination centers in the bulk which barrier the charge transport. 2) the charge carrier density is too low in g-C_3N_4.

Investigations into the trap states conditions and photocatalytic performance of g-C_3N_4 powder revealed that deep trap states, whose energy levels are much lower than the conduction band, is detrimental to the surface hole accumulation and remains inactive for water oxidation.[152] It was also reported that the structural disorder in g-C_3N_4 could introduce both shallow trap states and the deep trap states, and the shallow trap states positively contributed to its photocatalytic performance.[153] Studies into the charge diffusion length suggested that g-C_3N_4/rGO film could have an extraordinary charge diffusion length up to 36 μm; but without rGO, diffusion length would be a limiting factor of g-C_3N_4's PEC performance.[154] The diffusion length of pristine g-C_3N_4 is challenging to measure even it is imperative. I have synthesised highly crystallized, uniform g-C_3N_4 with different thicknesses and determined the electron diffusion length to be ~1000 nm using a transient photovoltage decay (TPV) method. The electron diffusion length is an intrinsic property of g-C_3N_4 and is not affected by the film thickness. Such an impressive electron diffusion

length allowed efficient photo-generated charge collection across a thin film smaller than 1000 nm.

2.5.3 Strategies for developing high performance g-C_3N_4 polymer photoelectrode

g-C_3N_4, though, has a great potential to PEC application due to its thermal and chemical stability, appealing band structure, and low cost, performance on carbon nitride photoelectrode is very moderate due to several problems, such as a high charge recombination rate, slow charge transfer, and high electrical resistance. Charge dynamics investigations into typical metal oxide semiconductors such as TiO_2, Fe_2O_3 and $BiVO_4$ suggest several strategies, which could be used to improve the PEC performance of g-C_3N_4, including:

(1) To avoid the deep trap states in bulk and achieve long charge diffusion length in pure g-C_3N_4, a high-crystalline g-C_3N_4 thin film with a low defects density could enable efficient charge collection across the film.

(2) Doping heteroatom at the surface could not only enhance conductivity without introducing defects in the bulk but also promote charge separation on the surface. The surface/bulk heterojunction could facilitate the charge transfer and inhibit the charge recombination.

(3) Creating nanostructure of a g-C_3N_4 film which has an extremely short distance for charges to migrate from the bulk to the surface and large surface area for surface reaction.

(4) Loading a co-catalyst on surface speeds up the surface water oxidation/reduction reaction and thus suppresses the surface recombination. Typically, these co-catalysts are deposited on the

electrode as a thin layer or islands (nanoparticles) to avoid light absorption.

These strategies will be applied in my project and discussed in the following chapters.

3 Experimental

3.1 Films fabrication

The fabrication of g-C_3N_4 films is very challenging. Different synthesis methods would give rise to various film qualities including crystallinity, defects condition and morphology. In this report, four film-fabrication methods were developed and presented below. Typical synthesis recipe of each method was clarified, and the appearance of resultant films was presented with its microstructure.

3.1.1 (Seed layer) thermal evaporation method

Thermal Evaporation method is a traditional method of making g-C_3N_4 films. This method could produce porous but non-uniform g-C_3N_4 films on FTO substrate. In a typical run, an FTO substrate was firstly pre-treated with Dicyandiamide (DCDA) by a rapid thermal vapor condensation method at 600 °C for 25 min to make it a more suitable place for carbon nitride nucleation and polymerization. After treatment, there is no visible g-C_3N_4 left on the substrate. The treated FTO was then placed on a 10 ml crucible (FTO side downward) filled with 2 g Dicyandiamide (DCDA). A flat crucible lid was placed above FTO to prevent the precursor vapour leaking. The crucible was calcined at 600 °C for 4h with a heating rate of 5 °C/min and cooled to room temperature naturally. The experiment set up and a photo of a typical as-prepared sample is displayed in **Fig. 17**. SEM image of a typical sample showed a porous and non-uniform microstructure in **Fig. 18**. G-C_3N_4 prepared from this Thermal Evaporation method was labelled as porous-g-C_3N_4 in this report.

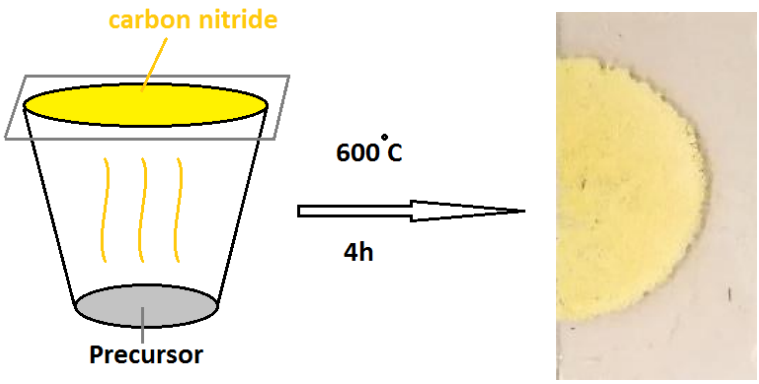

Fig. 17 Experiment set up and the photo of a typical as-prepared sample of thermal evaporation method

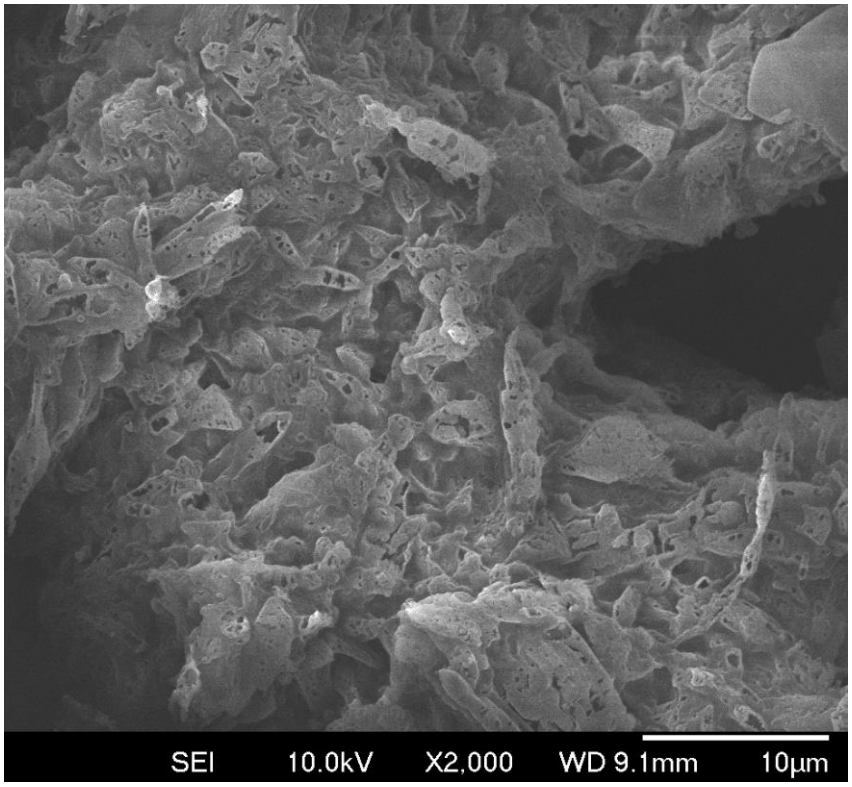

Fig. 18 SEM top view of a typical porous-g-C_3N_4 sample

3.1.2 Rapid thermal condensation method

Rapid Thermal Condensation method is a very efficient method of fabricating high-quality g-C_3N_4 film with high crystallinity, low defects density and uniform

morphology reported by my previous paper. In a typical run, 50mg Dicyandiamide (Alfa Aesar, 99%) was dissolved with DI water in a Φ35mm petri dish. After drying at 70°C for 1h, the precursor was crystallized and adhered to the internal surface of the petri dish. A piece of 20mm × 20mm FTO glass used as the substrate was placed on a slightly concave crucible lid holder and covered by the petri dish, as shown in **Fig. 19**. The sample was calcined in a 600°C preheated Muffle furnace (Carbolite, CWF 1300) for 20min and quenched to the room temperature in air. The key to successfully fabricating the high-quality film was using a slight concave crucible lid as the sample holder. Using a flat sample holder would only result in non-compact, low-quality films. The appearance of the g-C_3N_4 film was presented in **Fig. 19**. The g-C_3N_4 covering the edge of the FTO substrate was easily to be removed, while the central area is the desirable, high-quality g-C_3N_4 film which was so robust that could hardly be scratched from the FTO substrate. The top and side microstructure view of the central part was shown in **Fig. 20**, from which a very uniform and dense morphology was observed. The thickness of this film could be well controlled by either adjusting the precursor amount or manipulating the calcination time. The g-C_3N_4 film synthesised by this Rapid Thermal Condensation method was denoted as compact-g-C_3N_4 in this report.

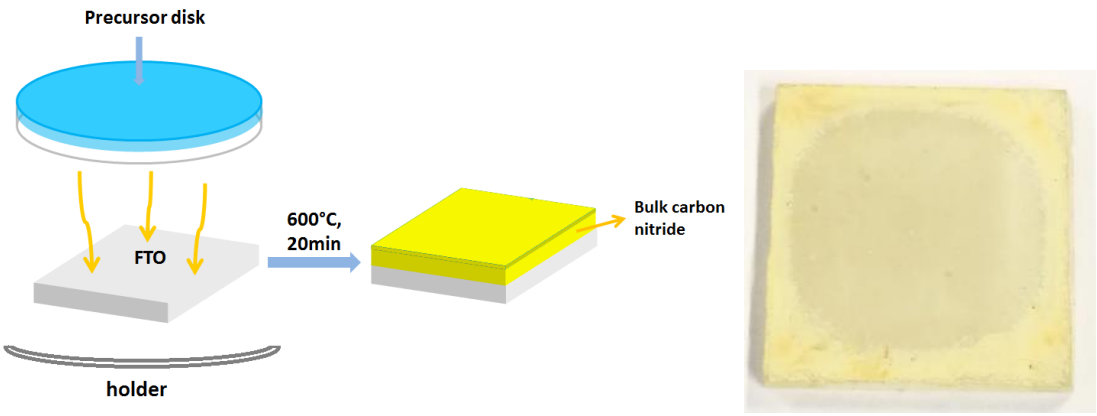

Fig. 19 Experiment set up and a photo of a typical as-prepared sample of rapid thermal condensation method

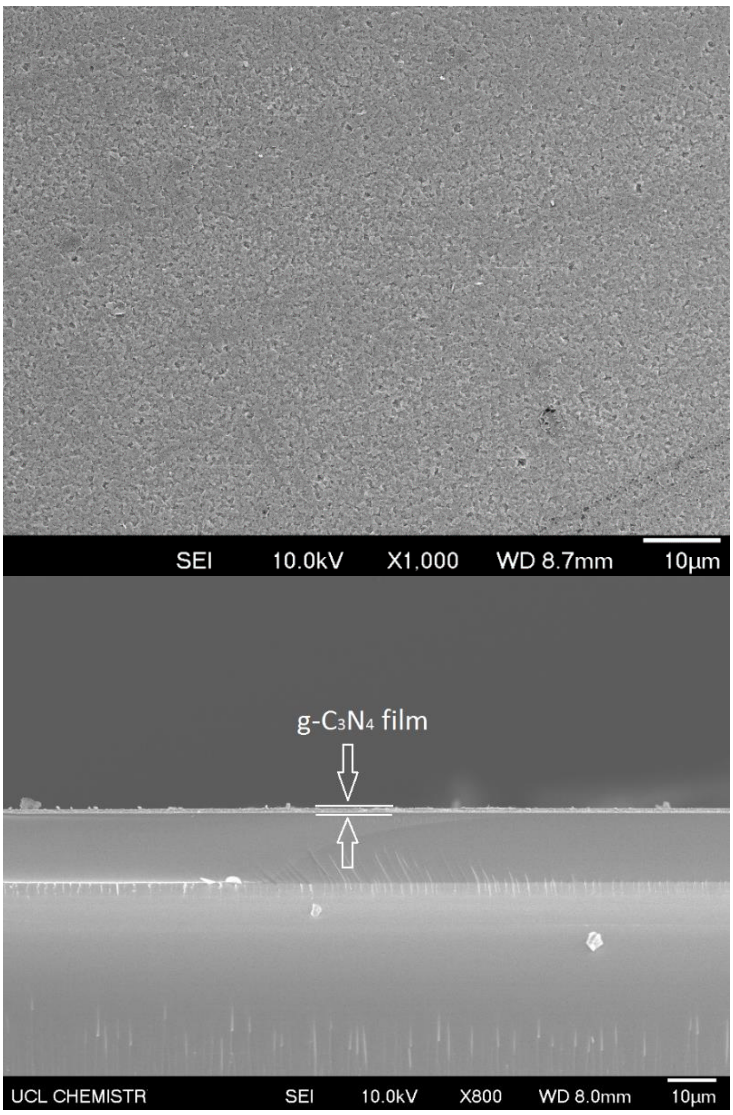

Fig. 20 SEM top and side view of a compact-g-C_3N_4 film

3.1.3 HCl assisted thermal evaporation method

The compact-g-C_3N_4 film has excellent photocatalytic performance as a photoanode. However, synthesising a photocathode out of g-C_3N_4 is more attractive due to its negative energy level of the conduction band. The problem is that g-C_3N_4 is an n-type semiconductor where holes trend to accumulate on the surface of the materials and prevent the electron from transferring to the aqueous solution for the reduction reaction. It makes the synthesis of g-C_3N_4 photocathode very challenging. Considering the great success people have achieved in suspension system using g-C_3N_4 for water reduction, introducing defects on the surface of g-C_3N_4 might be a promising solution to a photocathode.

HCl-assisted thermal evaporation method is invented here in an attempt to introduce defects on the surface of g-C_3N_4. The DCDA precursor treated by a various amount of HCl (laboratory reagent grade, ~37%, Fisher Chemical) was fabricated on FTO glass substrate using a rapid thermal evaporation method. In a typical run, 50mg (0.6mmol) DCDA ($C_2H_4N_4$, 99%, Alfa Aesar) and 0.6mmol HCl were dissolved with 2ml distilled water. After thorough stirring, 2 ml of the well-mixed solution was spread on a 4 cm × 4 cm FTO glass substrate by the pipette and dried in the Advantage-Lab drying oven at 70°C for 1h. The dried precursor (Dicyandiamide with hydrochloride) adhered to the surface of the FTO glass substrate. The substrate was place onto a Φ35mm petri dish with the precursor downward. The sample was placed in a 550°C preheated Carbolite muffle furnace and calcined for 20 min and quenched to the room temperature in air. This method gave a porous film as shown in **Fig. 21**. The microstructure showed a sponge-like morphology probably caused by the evaporation of HCl

during the polymerization in **Fig. 22**. G-C_3N_4 films prepared by the HCl assisted thermal evaporation method was labelled as HCl-g-C_3N_4 in this report.

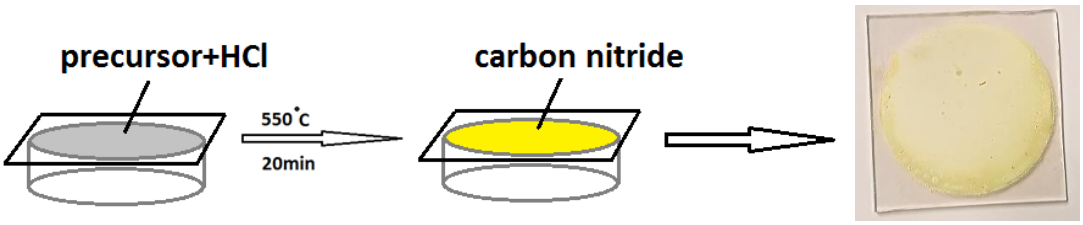

Fig. 21 Experiment set up and a photo of a typical as-prepared sample of HCl assisted thermal evaporation method

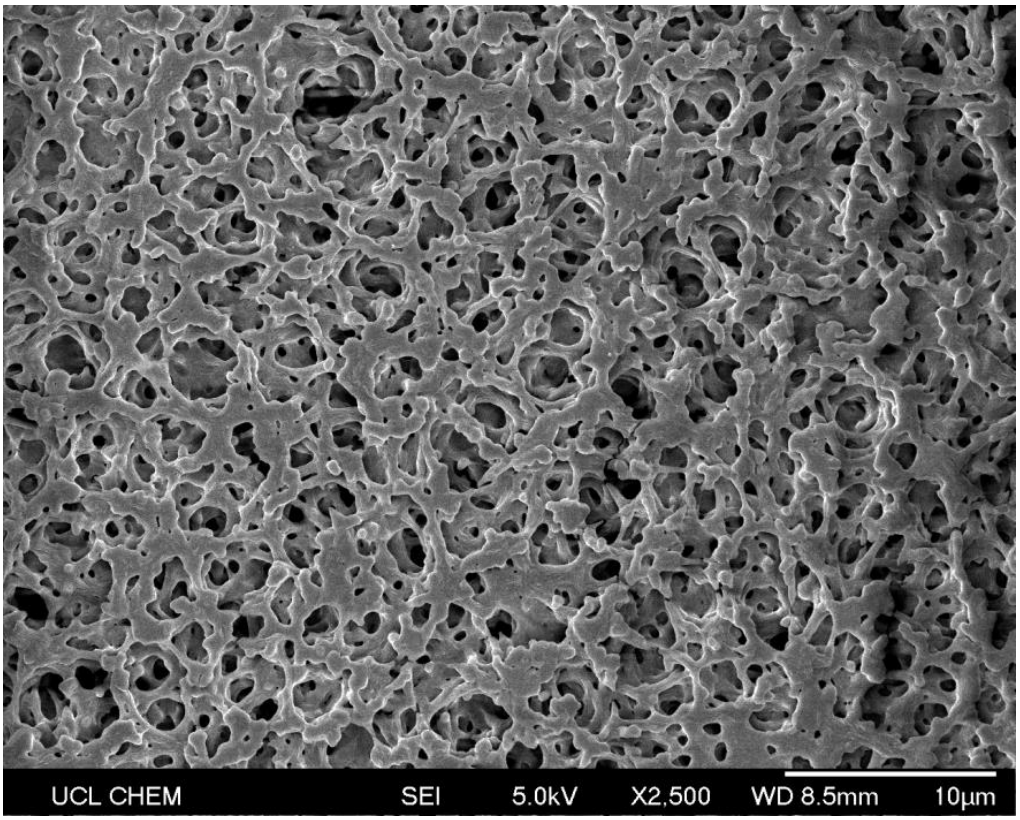

Fig. 22 SEM top view of a typical HCl-g-C_3N_4 sample

3.1.4 Nanosheet g-C_3N_4 drop-casting method

Unfortunately, HCl assisted thermal evaporation method was not an ideal approach to introduce the –OH groups on g-C_3N_4 as its photocathodic performance is quite poor. An alternative way is to mimic the g-C_3N_4 suspension

by sonicating the g-C_3N_4 powder into nanosheet and drop-casting it into a film. In this method (**Fig. 23**), a typical g-C_3N_4 film was fabricated by drop-casting 1ml of sonicated g-C_3N_4 suspension (10 mg g-C_3N_4 in 30ml aqueous solution) onto a 2 cm * 2 cm FTO substrate, followed by drying at 70°C for 1h. The synthesised film was robust and could not be easily removed from the FTO substrate. In **Fig. 24**, the microstructure showed a rough morphology formed by the aggregation of g-C_3N_4 particles. Characterizations have shown that a large amount of defects exist in this g-C_3N_4 film and it exhibited obvious photocathodic performance. G-C_3N_4 films prepared by this method were labelled as defect-introduced g-C_3N_4 in this report.

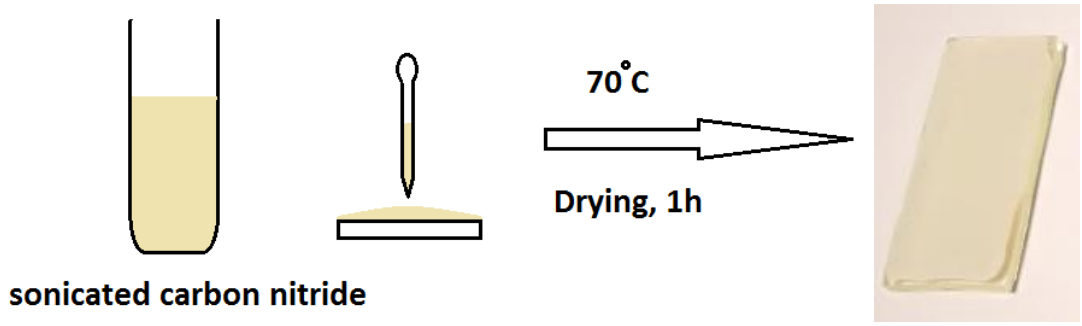

Fig. 23 Experiment set and a photo of a typical deficit introduced g-C_3N_4 sample prepared by the nanosheet drop casting method

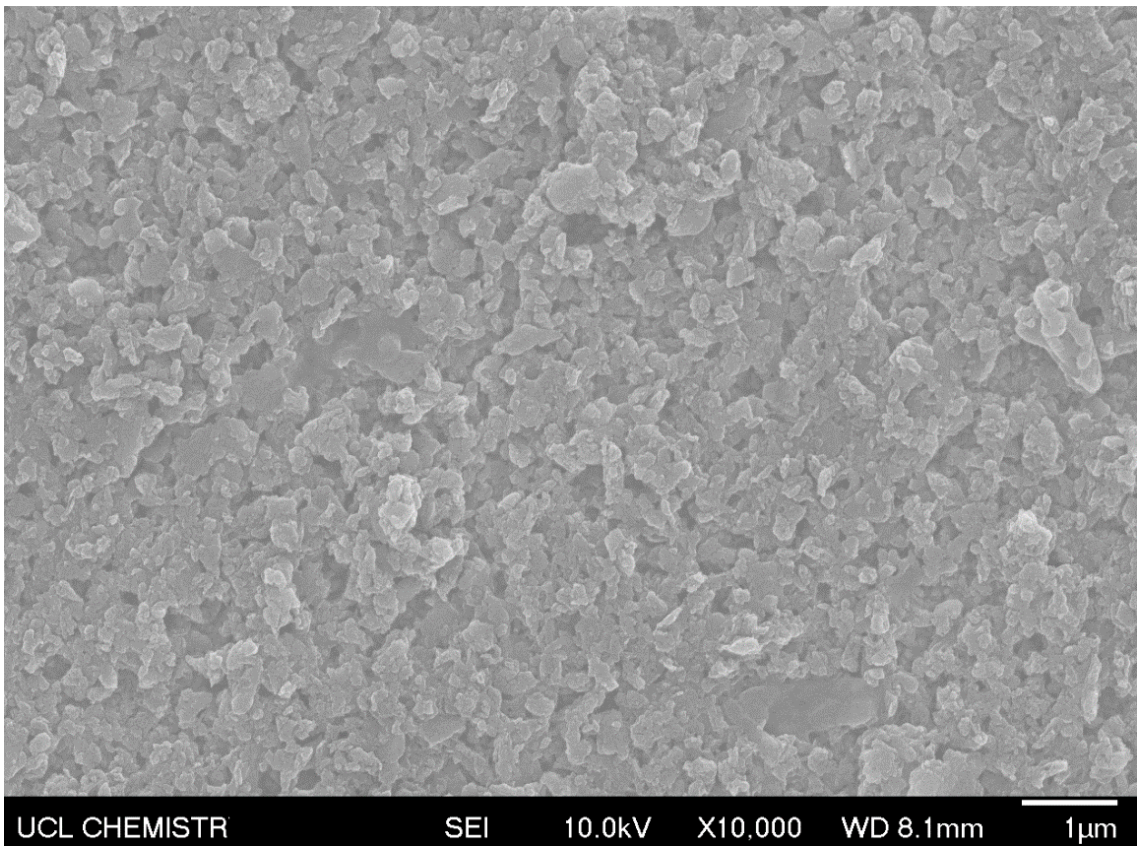

Fig. 24 SEM top view of a typical deficit introduced g-C_3N_4 sample

3.2 Material characterisation

3.2.1 X-ray diffraction (XRD)

XRD short for X-ray powder diffraction is a rapid analytical technique for crystalline material phase identification based on constructive interference of monochromatic x-rays. Structural properties of the crystals such as lattice parameters, strain, grain size, preferred orientation and phase composition can also be roughly determined by XRD pattern analysis.

The constructive interference happens when the interaction of the incident rays with the sample satisfy Bragg's Law:

$n\lambda = 2d \sin \theta$

where λ means the wavelength of the X-rays, d is the atomic d(hkl) spacing, θ is the incident angle, n is an integer, and λ is the wavelength of the X-ray.

This law indicates a relationship between the wavelength of electromagnetic radiation and the diffraction angle (the lattice spacing) in a crystalline sample. By scanning the sample through a range of 2θ angles, all possible diffraction directions of the lattice will be obtained due to the randomly orientated powder of the material. As each crystalline material and framework structure produces a unique diffraction pattern, XRD patterns of samples can be used to identify the phase if a standard pattern is known.

The X-ray source is a cathode ray tube that produces radiation with a characteristic wavelength of its target material. A Cu radiation X-ray source has a wavelength of 1.54 Å while a Mo radiation has the wavelength of 0.71073 Å. Cu radiation is not suitable for compounds containing Cr, Mn, Fe, Co, Ni and so on, because x-ray will be absorbed by these materials and strong fluorescence is generated and affects the quality of spectra. In this sense, Mo radiation with a shorter wavelength is used for substitution. Generally, $Z_{target} > Z_{sample} + 1$, where Z_{target} is the atomic number of target materials (Cu, Co, Mo) and Z_{sample} is the atomic number of elements in samples.

3.2.2 Ultraviolet and visible (UV-Vis) spectroscopy

UV-Vis absorption spectroscopy is the measurement of the attenuation of a beam of light after it passes through or reflection from a sample. When a sample is exposed to light energy that matches the energy difference between possible electronic transitions within the molecule, fraction of the light energy would be absorbed by the molecule, and the electrons would be promoted to

the higher energy state orbital. When a bond formed between molecules, the atoms in a bond have their atomic orbitals merged to form molecular orbitals which are occupied by electrons of different energy levels. Ground state molecular orbitals can be excited to anti-bonding molecular orbitals (*). These electrons when imparted with energy in the form of light radiation get excited from the highest occupied molecular orbital to the lowest unoccupied molecular orbital and the resulting species is known as the excited state or anti-bonding state.

In UV spectroscopy, molecule undergoes electronic transition involving σ, π and n electrons. Four types of electronic transition are possible, including σ - σ* transition, n -σ* transition, n -π* transition and π -π* transition. Most organic compounds are undergoing transitions for n -π* and π -π* transition.

UV-Visible spectroscopy enables an analysis of light absorption of materials over a wavelength range. Molecules often undergo electron transitions at these frequencies, since those molecules here are semiconductors, which have indiscrete energy levels corresponding to allowed electron states, one can determine the size and type of bandgap (direct or indirect) by using the equation 13[155]:

$(\alpha h\nu)^n = A(h\nu - E_g)$ (Equation 13)

Where α is the absorption coefficient, hv is the energy of the incident radiation, A is the constant which is based on effective masses of electrons and holes, E_g is the optical bandgap, and n can take the values of 0.5 and 2, for a direct or indirect bandgap transition.

The bandgap of a semiconductor is approximately equal to the absorption edge, and so one can also find this from extrapolating towards the x-axis on a plot of wavelength (x-axis) versus absorption (y-axis), then using the following equation 14, calculate the bandgap:

$E = hc / \lambda = 1240 / \lambda$ (Equation 14)

It should be noted that the absorption edge can be blue shifted by decreasing the particle size, and is often attributed to either a quantum size effect or a direct charge-transfer transition. If the bandgap region possesses a long tail and appears to be red shifted, then this would conclude that there are additional sub bandgap states present[156].

3.2.3 X-Ray Photoelectron Spectroscopy (XPS)

XPS short for X-ray photoelectron spectroscopy is usually employed to analyze the surface chemistry of a material, such as elemental composition, empirical formula, chemical state and electronic state, by irradiating the surface with an X-ray beam and simultaneously measuring the kinetic energy and electrons that are emitted from the top 1-10 nm of the material. When an atom or molecule absorbs an X-ray photon, an electron can be ejected. By measuring the kinetic energy of the emitted electrons which depends on the photon energy (hv) and the binding energy (BE) of the electron, it is possible to determine elements near the surface of materials, their chemical states and their chemical environment. It is worth noticing that XPS can only determine the elements components on the surface of materials. To characterize the elements ratio in the bulk, such as g-C_3N_4, CHN techniques may be more suitable.

3.2.4 Microscopes (SEM, TEM)

Scanning Electron Microscopy (SEM) is a useful technology for imaging the surface features of a semiconductor, surface morphology (shape and particles size which making up the semiconductor), and the composition of the semiconductor and their relative amount. To get the composition information, SEM must have an Energy Dispersive-X-ray (EDX) attachment. The SEM generates a high energy electron beam by the electron gun that interacts with the semiconductor surface resulting in electrons with different energy ejected from the sample. The common mode of SEM only collects secondary electrons within a few nanometres from the surface, which has energy as low as 50 eV.

Transmission Electron Microscopy (TEM) is another important technology for imaging samples involving the transmission of a high energy electron beam (>100kV) through a thin sample (<100nm). After the interaction between the atoms and electrons, the magnified image is generated by using of optical lens and then projected onto a photographic film or CCD camera. Unlike SEM, TEM images are produced base on transmitted electrons that are directly pointed toward the sample and thus be able to see what inside the surface. In addition, TEM produces a two-dimensional image with the resolution as high as 0.5 angstroms.

3.2.5 Raman spectroscopy

Raman spectroscopy is a light scattering technique usually to identify the structural fingerprint of a material by observing the vibration and rotation in a structure. When light is irradiated on molecules, it is scattered. Some fraction of light experiences a change in frequency because of the interaction between

light oscillation and molecular vibration and rotation. It is possible to analyse the composition of material or crystal lattice by analysing Raman scattering spectrum.

3.2.6 Fourier-transform infrared (FTIR) spectroscopy

Fourier-transform infrared spectroscopy (FTIR) is a technique used to obtain an infrared spectrum of absorption or emission of a material. The obtained spectra represent the fingerprint of samples, which can be used to identify the chemical structure of different materials.

3.3 Photoelectrochemical (PEC) characterization

3.3.1 Electrochemical Impedance Spectroscopy (EIS)

Electrical impedance is an effective technique to investigate the electrode/electrolyte interface condition in a PEC cell along with the conductivity of the electrode.

Impedance measures the ability of a circuit to resist the flow of electrical current and can be applied to alternating current (AC) which is different from resistance in direct current (DC) only. In impedance in AC circuits, there are two more components besides the resistance in DC circuits: Inductance (the induction of voltages in conductors self-induced by the magnetic fields of currents[157]) and Capacitance (the electrostatic storage of charges induced by a voltage between conductors). The impedance caused by these two effects is regarded as reactance and forms the imaginary part of complex impedance, whereas resistance forms the real part.

An example of an impedance spectrum of an illuminated n-GaAs electrode is illustrated in **Fig. 25**. The appearance of a small semicircle at high frequency and the peak of capacitance is accounted for recombination of photogenerated holes with CB electrons at the semiconductor surface[158]. The recombination mechanism consists of the successive capture of an electron in an empty surface state and a hole in an occupied surface state. An equivalent circuit corresponding to the electrochemical impedance spectrum is also shown. The overall impedance of the semiconductor/electrolyte interface consists of the parallel connection of the surface-recombination impedance and the space charge layer capacitor (C_1), because the photocurrent density (dis)charges the space charge layer of the semiconductor. At high frequencies, the recombination impedance reduces to the resistor R_1. Hence, the high-frequency impedance of the interface corresponds to the parallel connection of R_1 and C_1. This parallel combination accounts for the experimentally observed high-frequency semicircle.

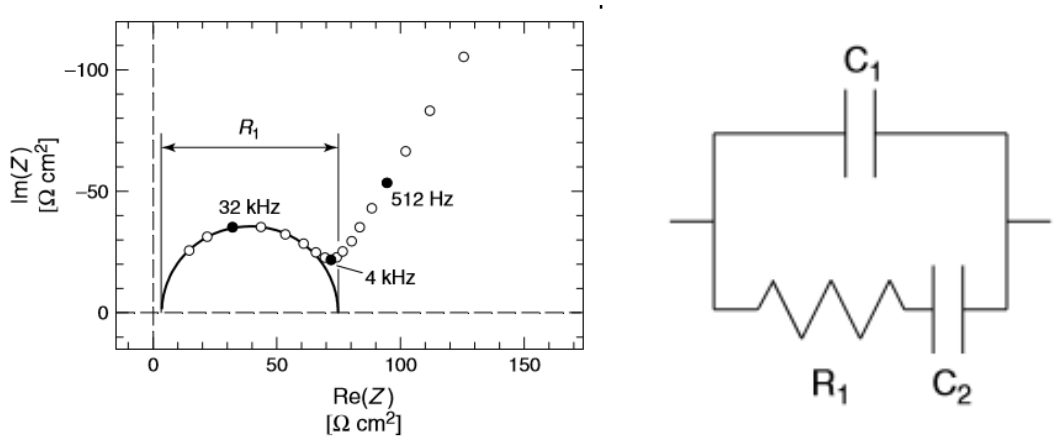

Fig. 25 High-frequency electrochemical impedance spectrum and equivalent circuit obtained for surface recombination at a semiconductor/electrolyte interface. Reproduced from reference[159].

3.3.2 Mott-Schottky (MS) analysis

M-S spectrum analysis is an important technique which reveals the physic properties of electrodes in PEC cells, such as n-/p-type features, the minority carrier density in semiconductors and the flat band potential. An illustration of M-S plots of n-type carbon nitride electrode is shown in **Fig. 26**. The positive slope of the Mott-Schottky plot means that carbon nitride is an n-type semiconductor. On the contrary, a negative slope of the Mott-Schottky plot reveals a p-type feature of a semiconductor.

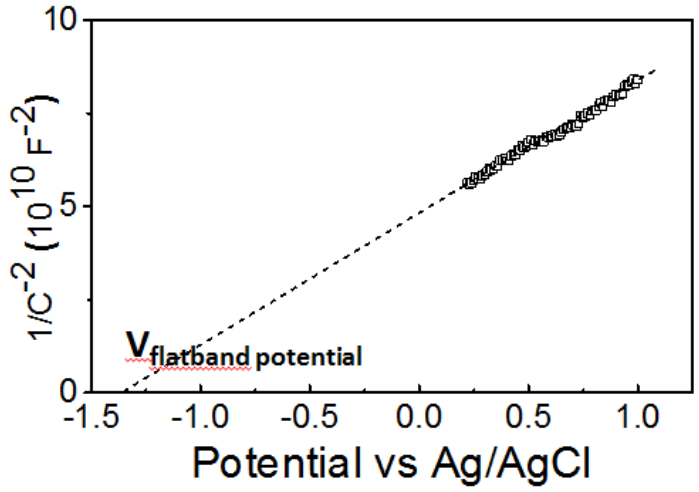

Fig. 26 M-S plots of n-type carbon nitride electrode

Flat band potential

Flat-band potential (Vfb) is the voltage applied when there is no band bending or charge depletion, or charge depletion. One approach to determine the flat band potential of a semiconductor in the PEC cell is measuring the capacitance of the space charge region as a function of potential under depletion condition. It can be described by the Mott-Schottky relationship (equation 15)

$$\frac{1}{C^2} = \frac{2}{\varepsilon\varepsilon_0 A^2 e N_D}\left(V - V_{fb} - \frac{k_B T}{e}\right) \qquad \text{(Equation 15)}$$

where C_{sc} is the capacitance of the space charge region; ε is the dielectric constant of the semiconductor; ε_o is permittivity of free space; N is donor density; E is applied potential; E_{fb} is the flat-band potential

The flat-band potential can be determined by extrapolation to C = 0. The capacitance values are calculated from impedance measurements. The model required for the calculation is based on two assumptions: a) the capacitance value is assumed to be the value of the space charge capacitance. b) The equivalent circuit used in this model is a series combination of a resistor and a capacitance (the space charge capacitance). The capacitance is calculated from the imaginary component of the impedance (Z") using the relationship Z" = 1/2πfC.

Charge carrier density

The slope in the quasi-linear regions of the M-S plots near the flat-band potential (V_{fb}) where the depletion layer remains very thin can be used to calculate the carrier density by equation 16:

$$slope = \frac{2}{\varepsilon\varepsilon_0 A^2 e N_D} \qquad \text{(Equation 16)}$$

where e_0 is the electron charge; ε is the dielectric constant of Carbon Nitride; ε_0 is the permittivity of free space; N_d is the donor density, and V is the applied bias at the electrode.

With this equation, a positive correlation between charge carrier density in a semiconductor and the slope of the M-S plot is determined.

3.4 Charge dynamic study

3.4.1 Intensity-modulated photocurrent spectroscopy (IMPS)

In PEC cells, IMPS is a powerful technique to study the mechanism and kinetics of charge carrier at electrode/electrolyte interface by measuring the space charge, surface states and Helmholtz capacitances on the IMPS response[160].

In a photoanode, holes manage to reach the electrode/electrolyte interface where 4-hole chemistry water oxidation (charge transfer) competes with the surface recombination of electrons and holes. **Fig. 27** illustrates the competition between charge transfer and recombination at the electrode/electrolyte interface. Hole flux into the surface (jh) can either be captured by reducing agents or recombining via surface state or defects. K_t and K_r, respectively represent the charge transfer and surface recombination rate.

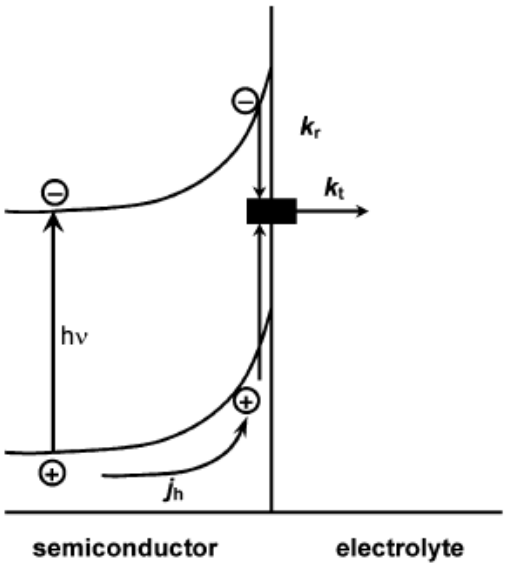

Fig. 27 Generalized reaction scheme showing competition between charge transfer and recombination, reproduced from reference.[161]

The time-dependent photocurrent response of a semiconductor electrode to a square illumination pulse is shown in **Fig. 28** to understand the charge carrier behaviours macroscopically. When the electrode is illuminated, an almost instantaneous hole-current (j_h) flows into the surface.

The capture of holes by surface states leads to a build-up of trapped holes, and as consequence, an electron current is induced as electrons recombine with the trapped holes. The photocurrent measured in the external circuit, therefore, falls from its initial value as the electron current increases towards its steady-state value. Now when the illumination is interrupted, the hole current ceases virtually instantaneously, and the remaining holes trapped in the surface recombine with electrons, giving a current of opposite sign to that observed during the illumination phase.

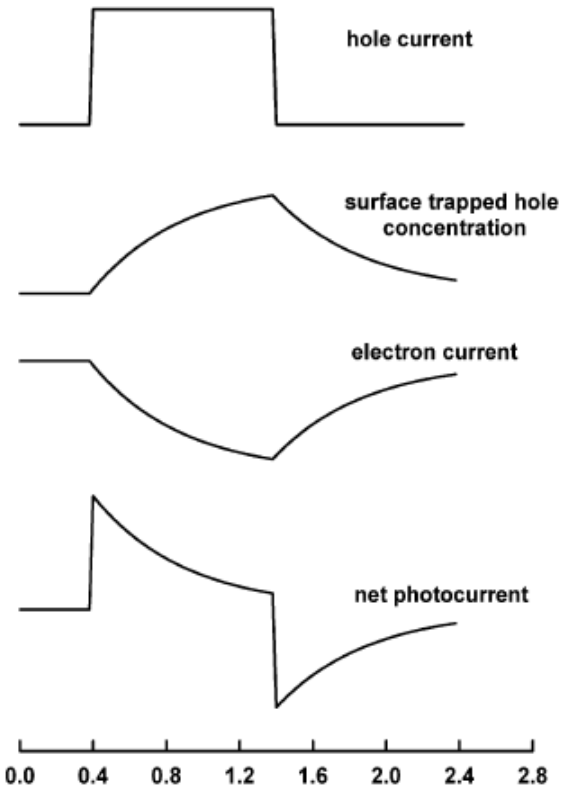

Fig. 28 Origin of the characteristic shape of the photocurrent response to square wave illumination, reproduced from reference.[161]

The time constant associated with the decay of the photocurrent is given by $k_r + k_t$, and the ratio of the steady-state photocurrent to the instantaneous photocurrent observed when the illumination is switched on is given by the ratio $k_t/(k_r + k_t)$ (**Fig. 29**).

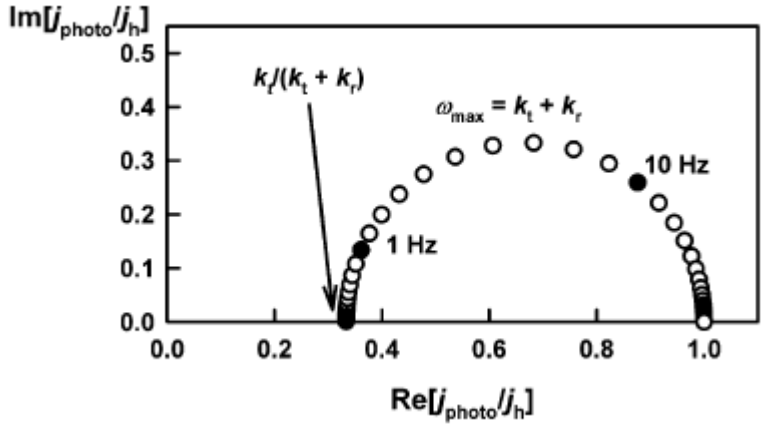

Fig. 29 Typical IMPS plot, K_r is the rate constant of surface charge recombination, K_t is the rate constant of surface charge transfer. Reproduced from reference.[161]

The high-frequency intercept of the low-frequency semicircle should occur at unity since the measured current is equal to the hole current (i.e. no recombination). The normalized low-frequency intercept of the low-frequency semicircle corresponds to the fraction of the hole flux that undergoes interfacial electron transfer, $k_t/(k_r + k_t)$]. The radial frequency at the maximum of the semicircle is given by the sum $k_t + k_r$.

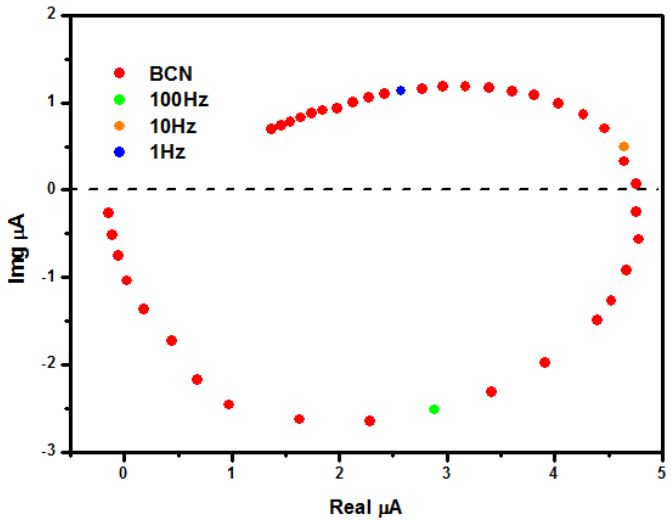

Fig. 30 IMPS plots of boron-doped carbon nitride photoanode

As shown in **Fig. 30**, the high-frequency IMPS response should correspond to the AC component of the hole flux j_h into the surface, since the effects of surface recombination are effectively 'frozen out'. The high frequency (HF) plot, therefore, provides a direct measure of hole collection, which is given by j_h/qI_0. By contrast, the low frequency intercept should correspond to the DC photocurrent, which is determined by the product $j_h(k_t/(k_t + k_r)$, where the ratio $k_t/(k_t + k_c)$ corresponds to hole transfer, the fraction of hole flux from the space charge region that is involved in the charge transfer reaction.

3.4.2 Open Circuit photoVoltage Decay (OCVD)

Open circuit voltage decay is an efficient technique to estimate the average lifetime of charges in the photoelectrode and its trap states condition.[162-165] The target photoelectrode was firstly placed in the electrolyte in the dark condition to ensure equilibrium voltage was obtained. When the light was turned on, photovoltage was generated. After a stable photovoltage was achieved, the illumination was cut off, resulting in a fast decay of the photovoltage with time.

The obtained photovoltage decay curve could be fitted into a biexponential function (equation 17):

$$\boldsymbol{V = A_0 + A_1 e^{-t/\tau_1} + A_2 e^{-t/\tau_2}} \quad \text{(Equation 17)}$$

Where τ_1 and τ_2 are time constants.

The average charge lifetime could be calculated by equation 18:

$$\boldsymbol{\tau_m = 2(\tau_1 \tau_2)/(\tau_1 + \tau_2)} \quad \text{(Equation 18)}$$

Where τ_m is the average charge lifetime.

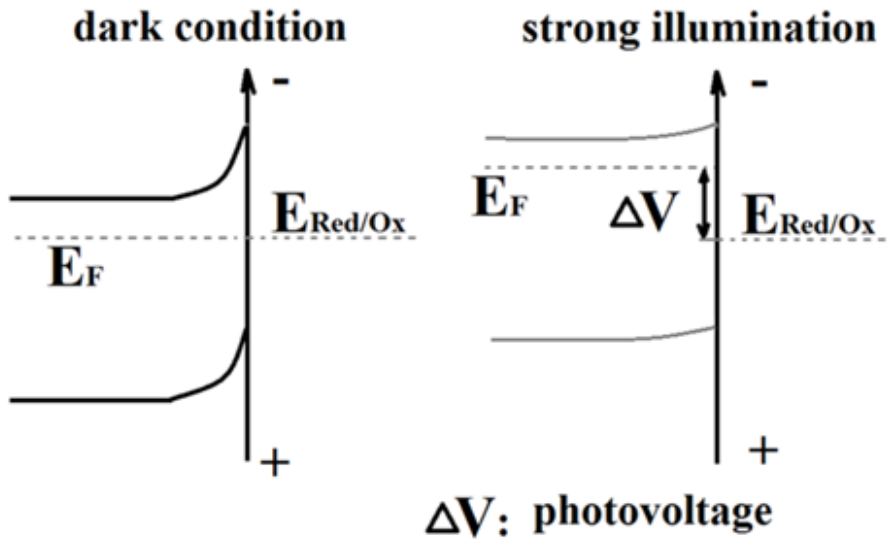

Fig. 31 Scheme of photovoltage generation for an n-type semiconductor.

The generated-photovoltage could be understood as the recovery of the band banding. In dark condition, the fermi level of an n-type semiconductor (as shown in **Fig. 31**) is at the same level as the redox potential in the electrolyte. With strong illumination, photo-generated electrons are promoted to the condition band, therefore, shifting the Fermi level upward. As the Fermi level becomes more negative, a negative photovoltage is observed in a PEC system. An

example of OCVD plot of an n-type g-C_3N_4 film is displayed in **Fig. 32**. a -290mV photovoltage is generated, and the average electron lifetime is estimated to be 0.9s.

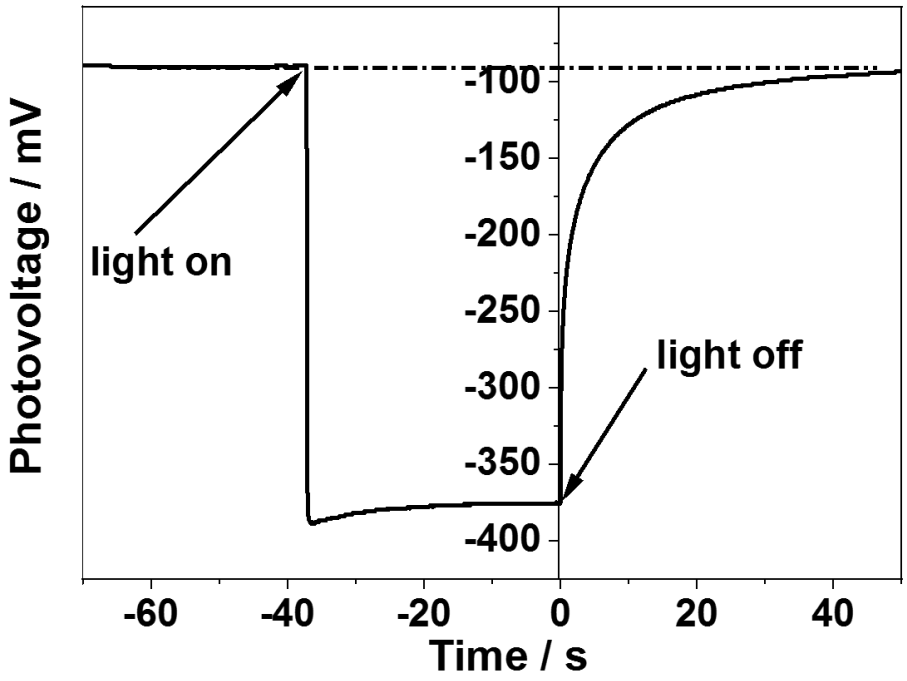

Fig. 32 OCVD plot of an n-type g-C_3N_4 film

A p-type semiconductor such as Cu_2O will generate a positive photovoltage (as shown in **Fig. 33**). The OCVD is another method to determine the n-type/p-type characteristic of a semiconductor.

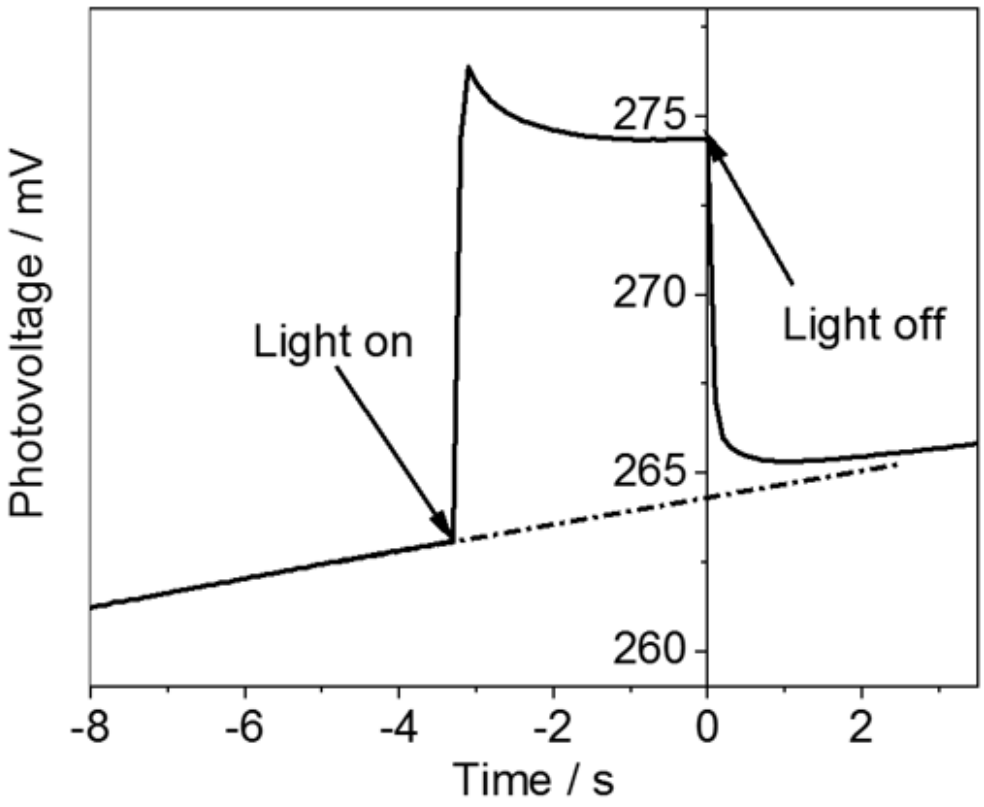

Fig. 33 Photovoltage of a p-type Cu_2O film prepared by electrodeposition (electrolyte: 15 g of Cu_2SO_4 was dissolved in 25 mL of 88% lactic acid to form the copper lactate complex. A total of 75 mL of a 5 M NaOH aqueous solution was added in small portions to the copper solution; pH was adjusted to 9, the voltage applied for electrodeposition: -0.1V vs Ag/AgCl

3.4.3 Transient Photovoltage decay (TPV)

TPV method has been used to determine the charge diffusion length in a semiconductor such as TiO_2[138]. In this method, a continuous strong light was irradiated onto the sample to generate electron-hole pairs. The generated electrons were promoted to trap states energy levels and then the conduction band. After the equilibrium between charge generation and charge consumption (recombination) was achieved, a single pulse light (1μs) was applied onto the EE side of the electrode. The photovoltage rise and decay corresponding to the

pulse light was recorded. An example of TPV of g-C_3N_4 under different pulse light intensity is shown in **Fig. 34**. The photovoltage rise and decay are due to the single pulse light. The electron diffusion length is derived by the following equations 19-21.

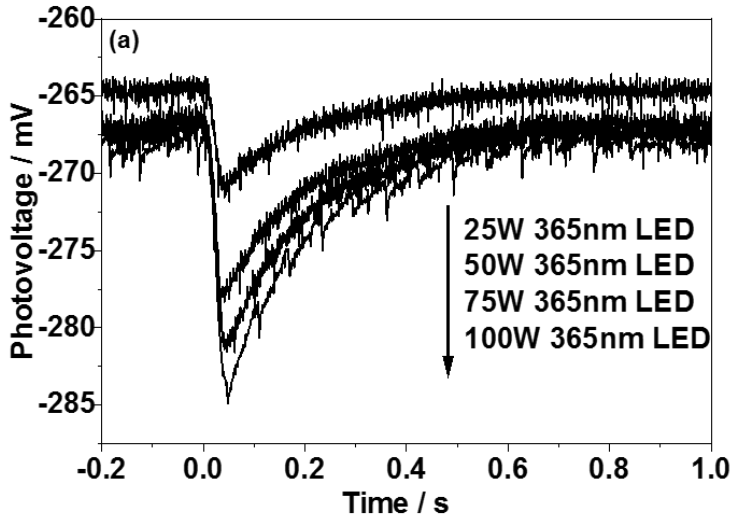

Fig. 34 TPV of g-C_3N_4 under different pulse light intensity

$$\boldsymbol{\tau} = -\frac{\boldsymbol{K_B T}}{\boldsymbol{q}}\left(\frac{\boldsymbol{dV_{oc}}}{\boldsymbol{dt}}\right)^{\boldsymbol{-1}} \quad \text{(Equation 19)}$$

$$\boldsymbol{D_n} = \frac{\boldsymbol{d^2}}{\boldsymbol{\pi^2}}\left(\mathbf{1} + \frac{\mathbf{3}}{\mathbf{1}+\left(\frac{\mathbf{3}}{\sqrt{\mathbf{2}}}-\mathbf{1}\right)\frac{\boldsymbol{C_{C3N4}}}{\boldsymbol{C_{sub}}}}\right)\left(\frac{\mathbf{1}}{\boldsymbol{\tau_{rise}}} - \frac{\mathbf{1}}{\boldsymbol{\tau_n}}\right) \quad \text{(Equation 20)}$$

$$\boldsymbol{L} = \left(\boldsymbol{D_n \tau_n}\right)^{\mathbf{1/2}} \quad \text{(Equation 21)}$$

Where d is the thickness of the film; C_{c3n4} is the capacitance of carbon nitride film; C_{sub} is the capacitance of FTO substrate; τ_{rise} is the time constant of photovoltage rise; τ_n is the time constant of photovoltage decay, D_n is the diffusion coefficient, and L is the charge diffusion length

4 Key Factors Dominating Photoelectrochemical Performance of g-C_3N_4 Polymer Films

This chapter would mainly study key factors that dominate the photocatalytic performance of g-C_3N_4 as an efficient photoanode. I investigated the relationship between crystallinity, deep trap states and PEC performance of g-C_3N_4 photoelectrodes. Long-lived charge carriers were present in the more poorly crystalline samples, due to deeper trap states, which inversely correlated with photoelectrochemical performance. The charge diffusion length in a compact g-C_3N_4 film as one of the most important factors dominating its PEC performance was determined.

4.1 Introduction

Development of polymer photocatalysts have been triggered after the discovery of g-C_3N_4 as population of materials due to ease of processing, readily tunable band structure, promising activity and composed of abundant elements.[166-167] Especially, the benchmark polymer photocatalyst g-C_3N_4 at present, has attracted considerable attention due to its thermal and chemical stability, appealing band structure and low cost. A wide range of photocatalytic applications of g-C_3N_4 has been reported, such as water splitting[10, 68, 70], CO_2 conversion,[168] organic pollutants degradation[169] and even in polymer synthesis.[170] Tremendous efforts have continuously been made to improve the performance of g-C_3N_4, such as by doping heteroatoms to extend its light absorption and manipulate the band structure to make it thermodynamically more favorable for redox reactions, or by controlling the microstructure and electronic properties of g-C_3N_4 to kinetically improve its charge transfer,[16, 80, 171-

[172] building upon the great success of g-C_3N_4 powder photocatalysis in suspension systems. To fabricate active g-C_3N_4 film is a subsequent preferred research area which is very attractive due to large-scale industrial and commercial use. Although there have been some attempts,[173-174] the prepared g-C_3N_4 films show very moderate photoelectrochemical performance, leading to a low photocurrent density of around 100 μA/cm^2 at 1.23 V under AM 1.5 illumination.[175-176] This is far inconsistent with the powder suspension systems reported so far.[177] It is rather different from metal oxide based photocatalysts which always show both excellent photocatalytic activities in suspension systems and photocurrent in a PEC cell, e.g. $BiVO_4$,[178-179] WO_3,[180] TaON[31] etc. There are some guesses about this extremely moderate photoelectrochemical performance of g-C_3N_4 e.g. due to poor charge separation, low electronic conductivity and small charge diffusion length.[174] Obviously, a clear and comprehensive insight into this dilemma is highly sought after.

It has been observed that the charge diffusion length plays a pivotal role in dictating photocurrents and photoelectrochemical performance. For instance, in case of α-Fe_2O_3 a well-known and well-studied benchmark oxide film suffers with poor and unsatisfactory photocurrents though it has very good light absorption as observed .[181] A comprehensive investigation by Grätzel *et al*. reveals that the key issue is the short charge diffusion length (~2-4 nm) in this benchmark oxide, which interpreted the very good performance of nanostructured, dendrite α-Fe_2O_3 films due to their shorter charge diffusion distance compared to bulk α-Fe_2O_3 films.[43, 141, 182] In the similar lines, it is quite obvious that the charge diffusion length is also an important factor in g-C_3N_4 in terms of charge separation, migration and surface reaction; the other factor

heavily influencing the photoelectrodes performance is charge separation and recombination dominated by trap states in the bulk or on the surface of a semiconductor.[96, 153]

The previous study related to the charge trapping in g-C_3N_4 powders in a suspension system described that a high concentration of electrons was deeply trapped by electron acceptors in g-C_3N_4 and remained unreactive.[152] These photogenerated separated electrons with a long lifetime could not participate in both photocatalytic reactions and photoluminescence. In other words, the density of long-lived electrons was correlated inversely with the photocatalytic activity. It was also reported that the structural disorder in g-C_3N_4 could introduce shallow trap states that compete with the deep trap states.[153] The impact of trap states on g-C_3N_4's activity is, to some extent, very informative although this useful information was achieved in a powder-suspension system. In a PEC system where the directional charge migration is vital, a large number of deep trap states will prohibit the directional charge transport and affect the charge diffusion length although they can prolong the lifetime of charges generated. Also, as reactions always happen at the semiconductor/electrolyte interface. The fast charge transfer at the interface would benefit the photoreaction while surface recombination would be detrimental. Massive surface trap states would also act as recombination centers.

The influences of both charge diffusion length and trap states on the performance of g-C_3N_4 photoelectrodes are very important which is currently less clear. It is speculated that deep trap states in g-C_3N_4 may be caused by terminal groups or defects which mainly appear on g-C_3N_4 surfaces.[152] The desired closely-packed and well-crystallized g-C_3N_4 thin film in principle is

expected to reduce the deep trap states which in turn facilitate the charge transfer with suitable charge diffusion length. To explore the influence of trap states on PEC performance of g-C_3N_4 films, here I fabricated three kinds of g-C_3N_4 films with different trap state conditions, including bulk-g-C_3N_4 film, porous-g-C_3N_4 film and the compact-g-C_3N_4 films. X-ray diffraction (XRD), Ultraviolet–visible spectroscopy (UV-vis), X-ray photoelectron spectroscopy (XPS) and Fourier-transform infrared spectroscopy (FTIR) have been used to characterize the structure of three g-C_3N_4 films. The electron decay lifetime and trap conditions were determined by the open circuit photovoltage decay (OCVD) technique. A three-electrode PEC system was applied to examine the PEC performance of these g-C_3N_4 films. Furthermore, charge diffusion length was measured by a small perturbation photovoltage transient (TPV) measurement to elucidate the key intrinsic factor of g-C_3N_4 films.

4.2 Experimental

Sample synthesis

The bulk-g-C_3N_4 film, compact-g-C_3N_4 film and porous-g-C_3N_4 film have been fabricated by three different methods. The compact-g-C_3N_4 film was synthesised by a rapid thermal condensation method referring to the method in section 3.1.2. The precise experimental condition was shown below: 50 mg Dicyandiamide (Alfa Aesar, 99%) was dissolved with DI water in a Φ35 mm petri dish. After drying at 70 °C for 1 h, Dicyandiamide precursor was recrystallized and adhered to the internal surface of the petri dish. A piece of 2 cm × 2 cm FTO glass used as the substrate was placed on a slightly concave crucible lid and covered by the petri dish. The sample was calcined in a 600 °C preheated Muffle furnace (Carbolite, CWF 1300) for 23 min and quenched to the room temperature in air.

The bulk-g-C_3N_4 film was synthesised by a drop-casting method. G-C_3N_4 powders were synthesised by heating Dicyandiamide (Alfa Aesar, 99%) at 600°C for 4h in the air in a Muffle furnace (Carbolite, CWF 1300) with a rate of 5°C/min. 10 mg as-prepared g-C_3N_4 powders were mixed with 750 ml DI H_2O, 250 ml 2-propanol (Fisher Chemical, HPLC grade) and 10 µl Nafion perfluorinated resin solution (Sigma-Aldrich). The suspension was sonicated for 1h and drop-casted onto a 2 cm * 2 cm FTO substrate on a 250 °C preheated hotplate. The as-synthesised film was calcined at 400 °C for 30 min to remove the organic residues.

The porous-g-C_3N_4 film was synthesised by a thermal evaporation method referring to the method in Section 3.1.1. To be precise, a FTO substrate was firstly pre-treated by a rapid thermal vapor condensation method at 600 °C for 25 min to make it a more suitable place for carbon nitride nucleation and polymerization. After treatment, there is no visible carbon nitride left on the substrate. The treated FTO was then placed on a 10 ml crucible (FTO side downward) filled with 2 g DCDA. A flat crucible lid was placed above FTO. The crucible was calcined at 600 °C for 4 h with a heating rate of 5 °C/min.

Photoelectrochemical measurements

The photoelectrochemical properties were investigated in a conventional three-electrode cell using an electrochemical analyser (IVIUM Technologies). The as-prepared film, a Pt net and an Ag/AgCl electrode were used as the working, counter and reference electrodes, respectively. The photocurrent of samples was measured in 0.1 M Na_2SO_4 aqueous solution under 150 W Xenon lamp (Newport). Samples were illuminated from the SE side (FTO substrate/semiconductor interface). Electrochemical impedance spectra (EIS)

were measured from -0.3 V to 0.5 V vs. Ag/AgCl. A sinusoidal ac perturbation of 5 mV was applied to the electrode over the frequency range 0.1 Hz−10 kHz.

In the open circuit voltage decay (OCVD) measurement, electrodes were placed in dark condition until the voltage became stable. 150 W Xenon lamp (Newport) was illuminated to the EE side of the electrode. After the stable photovoltage was observed, the light source was turned off to obtain the photovoltage decay.

In the small perturbation photovoltage transient (TPV) measurement, a continuous light source (150 W Xenon lamp) was irradiated to the sample to excite electron-hole pairs continuously. After the equilibrium between charges generation and charge consumption (recombination and reaction) was achieved, a one-shot pulse light (duration of 1ms) was irradiated to the EE side of the electrode. The photovoltage rise and decay corresponding to the pulse light was recorded and used for electron diffusion length calculation. The time constant for photovoltage rise and decay τ_{rise} and τ_n was calculated using the initial phase of photovoltage rise and decay with equation 19.

$$\tau = -\frac{K_B T}{q}\left(\frac{dV_{oc}}{dt}\right)^{-1} \quad \text{(Equation 19)}$$

Where k_B is the Boltzmann constant, T is the temperature (in Kelvin), and q is the unsigned charge of an electron.

The electron diffusion coefficient was used to calculated using equation 20[138]:

$$D_n = \frac{d^2}{\pi^2}\left(1 + \frac{3}{1+\left(\frac{3}{\sqrt{2}}-1\right)\frac{C_{C3N4}}{C_{sub}}}\right)\left(\frac{1}{\tau_{rise}} - \frac{1}{\tau_n}\right) \quad \text{(Equation 20)}$$

Where d is the thickness of the film; C_{c3n4} is the capacitance of carbon nitride film; C_{sub} is the capacitance of FTO substrate; τ_{rise} is the time constant of photovoltage rise; τ_n is the time constant of photovoltage decay.

The diffusion length L was calculated using the equation 21.

$L = (D_n \tau_n)^{1/2}$ (Equation 21)

4.3 Result and discussion

The bulk-g-C_3N_4 film prepared by drop-casting pre-synthesised g-C_3N_4 powder on an FTO substrate could represent the properties of pristine carbon nitride powders widely used in the photocatalytic suspension system, thus used as a reference sample. The compact-g-C_3N_4 film was fabricated by a rapid thermal vapor condensation method,[173] which is known to produce a uniform film with closely-packed microstructure. The porous-g-C_3N_4 film was synthesised via a thermal evaporation method, producing a rough surface and porous structure. To display the morphologies of g-C_3N_4 films prepared by different methods, SEM techniques have been applied,

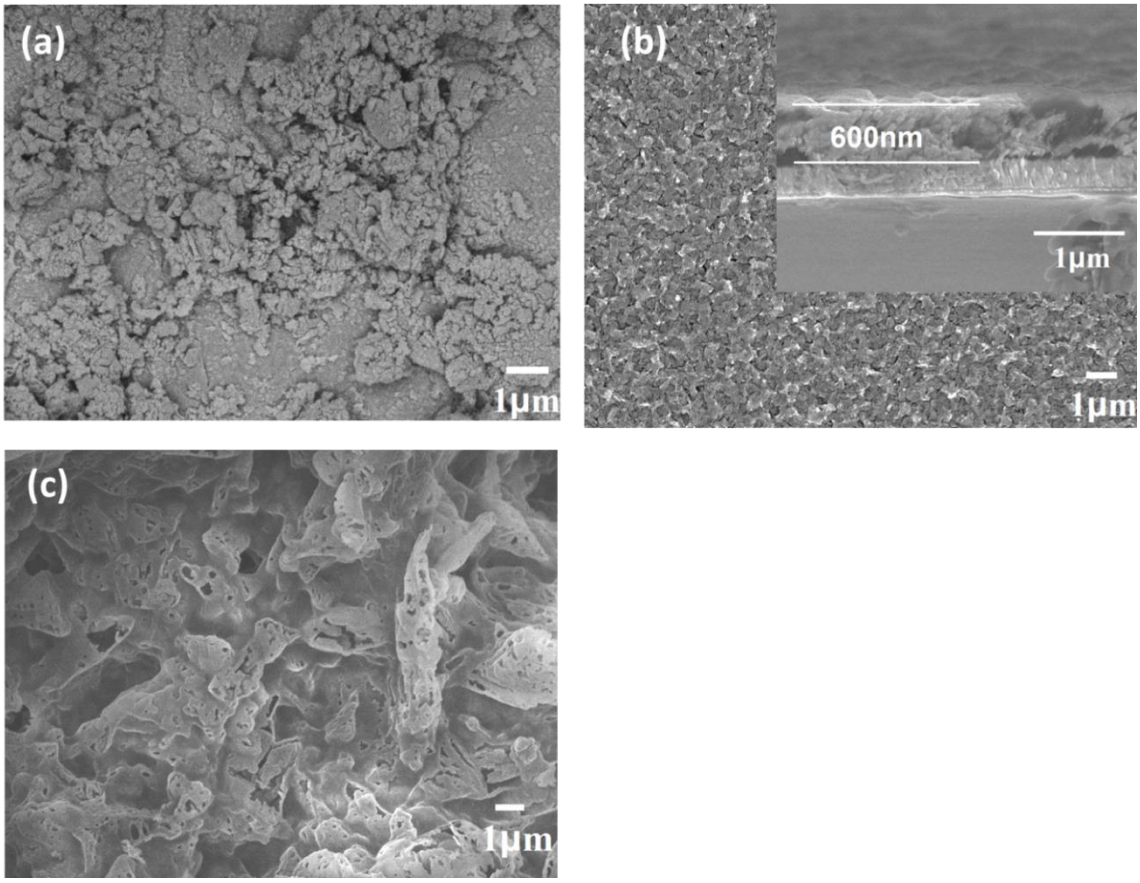

Fig. 35 SEM images of (a) bulk-g-C_3N_4 film top view, (b) compact-g-C_3N_4 film top view and side view (inset), (c) porous-g-C_3N_4 film top view.

SEM images show significantly different morphologies for bulk-g-C_3N_4 film, compact-g-C_3N_4 film and porous-g-C_3N_4 film as represented in **Fig. 35** a, b and c respectively. Apparently, the bulk-g-C_3N_4 film is composed of an aggregation of small particles with uneven distribution (**Fig. 35**a). The compact-g-C_3N_4 film exhibits a very uniform morphology and dense microstructure (**Fig. 35**b). The thickness of the compact-g-C_3N_4 film is determined to be 600 nm from its cross-section image (**Fig. 35**b, inset). The uniform and low thickness films are beneficial for charge migration and collection across the film in a PEC photocatalytic reaction. The porous-g-C_3N_4 film shows a rough surface with a hollow structure (**Fig. 35**c). The porous structure possesses a likely large

surface area, more defects and surface states which have a complicated influence on charge trap, transfer and recombination process.[183]

SEM images of different g-C_3N_4 samples have shown obvious differences. The XRD patterns of bulk-g-C_3N_4, compact-g-C_3N_4 and porous-g-C_3N_4 films are shown in **Fig. 36**a in order to examine the difference in their crystallinities. All samples show a main peak located around 27.5° which is due to the interlayer arrangement of a graphite-like structure. The weaker peak at 13.0° is attributed to the heptazine units in the g-C_3N_4 structure.[184] The extra peak at 26.7° is assigned to the (110) plane of SnO_2 from an FTO substrate. The full width at half maximum (FWHM) of XRD peak at 27.5° is calculated among the three samples to illustrate the crystallinity of the graphite-like layer structure.

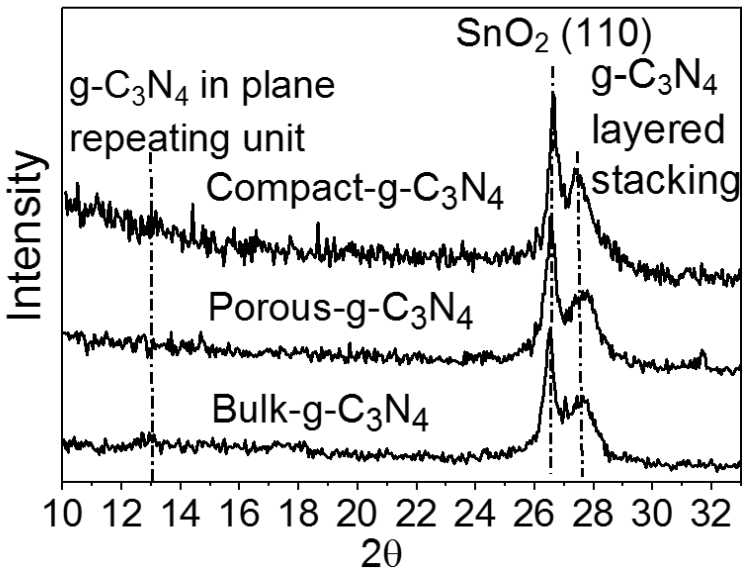

Fig. 36 XRD patterns of the bulk-g-C_3N_4 film, compact-g-C_3N_4 film and porous-g-C_3N_4 film.

In **Fig. 37**, the FWHM of the peak at 27.5° for bulk-g-C_3N_4 film, compact-g-C_3N_4 film and porous-g-C_3N_4 film are analyzed and determined to be around 1.0°, 0.7° and 1.1°, respectively. Smaller FWHM indicates higher crystallinity of

a material,[185] so the compact-g-C_3N_4 film possess relatively higher-ordered layer structure than bulk-g-C_3N_4 and porous-g-C_3N_4 films. The order of the crystallinity is compact-g-C_3N_4 > bulk-g-C_3N_4 > porous-g-C_3N_4 with all films prepared at 600 °C.

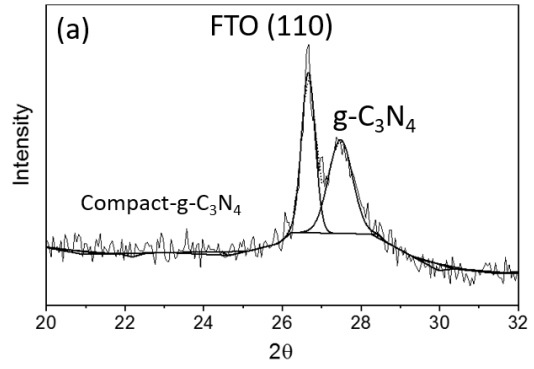

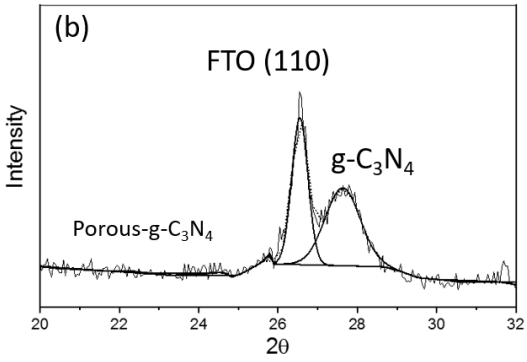

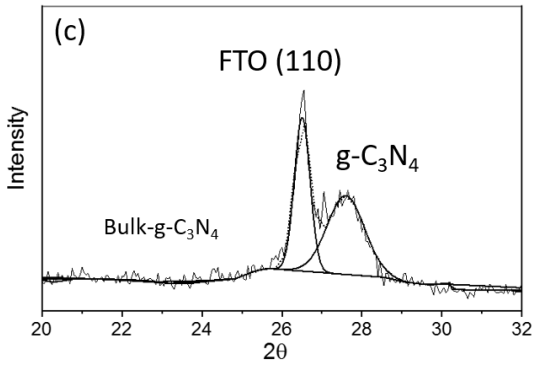

(d)

sample	FTO (110) FWHM	G-C_3N_4 FWHM
Compact-g-C_3N_4	0.41	0.7
Porous-g-C_3N_4	0.48	1.1
Bulk-g-C_3N_4	0.46	1.0

Fig. 37 XRD patterns showing peaks of FTO (110) plane and g-C_3N_4 stacking layer structure of (a) compact-g-C_3N_4, (b) bulk-g-C_3N_4 (c) porous-g-C_3N_4, (d) FWHM of peaks of all three samples

To further evidence the order of their structure, Raman spectra of all three samples are displayed in **Fig. 38**. From 1200-1700 cm^{-1} a series of peaks are attributed to C-N stretching vibrations, specifically “G and “D” band profiles of structurally disordered graphitic carbon and other carbon/nitrogen layered compounds. The peak at 980 cm^{-1} can be assigned to the symmetric N-breathing mode of heptazine, whilst the peak at 690 cm^{-1} corresponds to the in-plane bending vibrations of the tri/heptazine C-N-C linkages. All peaks,

therefore, confirm the local structure of the g-C_3N_4. The ratio of D band (locates at 1405 cm^{-1}) to G band (at 1570 cm^{-1}) could illustrate the distortion of the crystal structure and the defects density.[186]

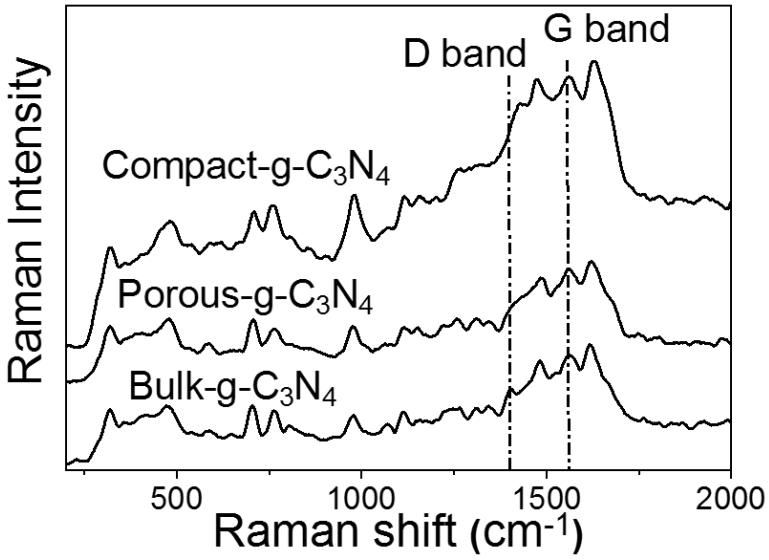

Fig. 38 Raman spectra of bulk-g-C_3N_4 film, compact-g-C_3N_4 film and porous-g-C_3N_4 film

The analysis of Raman spectra displayed in **Fig. 39** suggests that the I_D/I_G value increases in the order of compact-g-C_3N_4, bulk-g-C_3N_4 and porous-g-C_3N_4. The smallest I_D/I_G value (I_D/I_G=0.13) of the compact-g-C_3N_4 suggested that it has least defects among all three samples, while larger I_D/I_G values porous-g-C_3N_4 samples (I_D/I_G=0.55) indicates high defects density in bulk and more distorted structures with bulk-g-C_3N_4 (I_D/I_G=0.41) in the middle, which is consistent with the XRD analysis. The summary of XRD HWFM (with errors) and Raman analysis is displayed in **Table 4**.

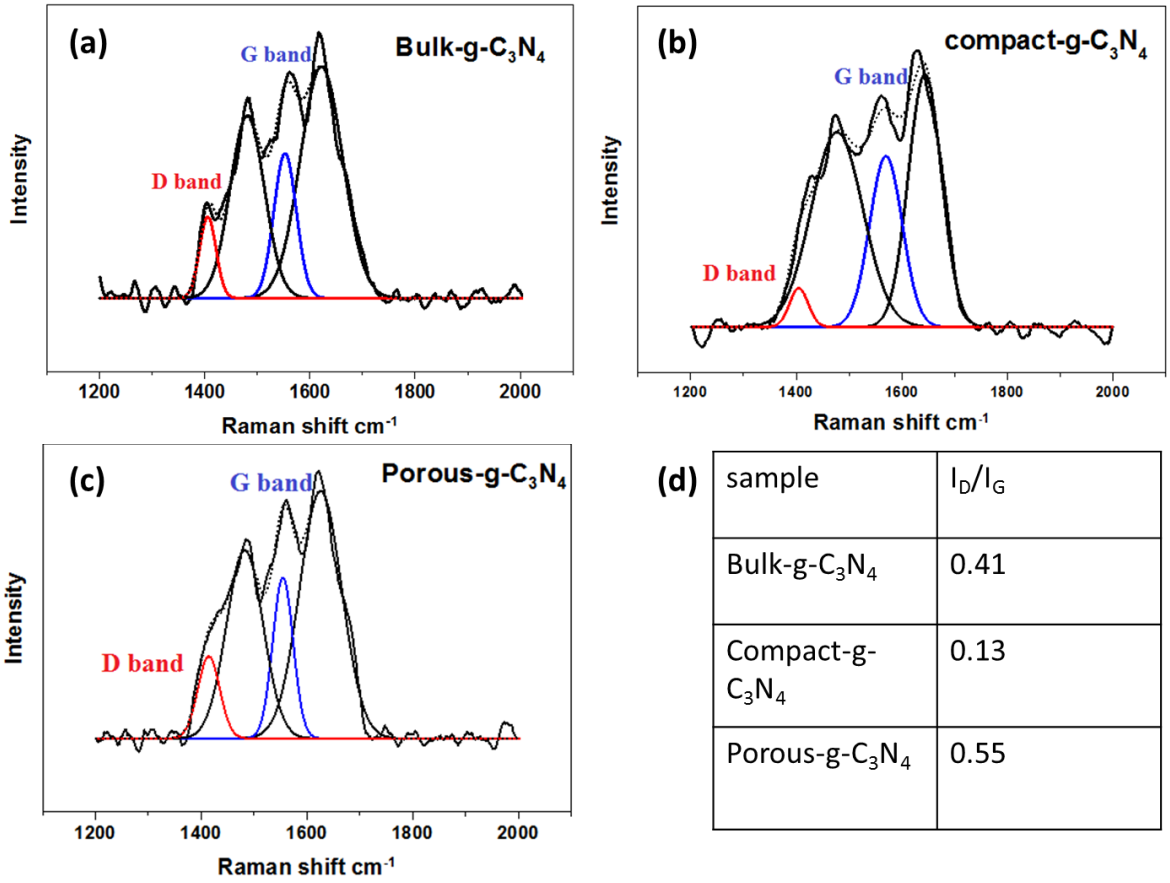

(d)

sample	I_D/I_G
Bulk-g-C_3N_4	0.41
Compact-g-C_3N_4	0.13
Porous-g-C_3N_4	0.55

Fig. 39 Raman spectra films showing different degrees of structural distortion of (a) bulk-g-C_3N_4, (b) compact-g-C_3N_4 (c) porous-g-C_3N_4; (d) the value of I_D/I_G of all three g-C_3N_4 samples. The Raman spectra were recorded with an exciting laser at 325 nm.

Table 4 FWHM with errors of peaks at 27.5° within XRD patterns (**Fig. 36**) and ratios of D band to G band within Raman spectra (**Fig. 38**) of three g-C_3N_4 films.

	Porous-g-C_3N_4	Bulk-g-C_3N_4	Compact-g-C_3N_4
XRD(FWHM)	1.07±0.05°	1.02±0.06°	0.70±0.04°
I_D/I_G	0.55	0.41	0.13

Although the differences in morphology and crystallinity, UV-vis spectra of all samples show a similar light absorption edge around 440 nm (**Fig. 40** a, c, e) and a similar bandgap of 2.8 eV, derived from the Tauc plot (**Fig. 40**b, d, f) which is in good consistency with pristine carbon nitride as reported earlier.[63]

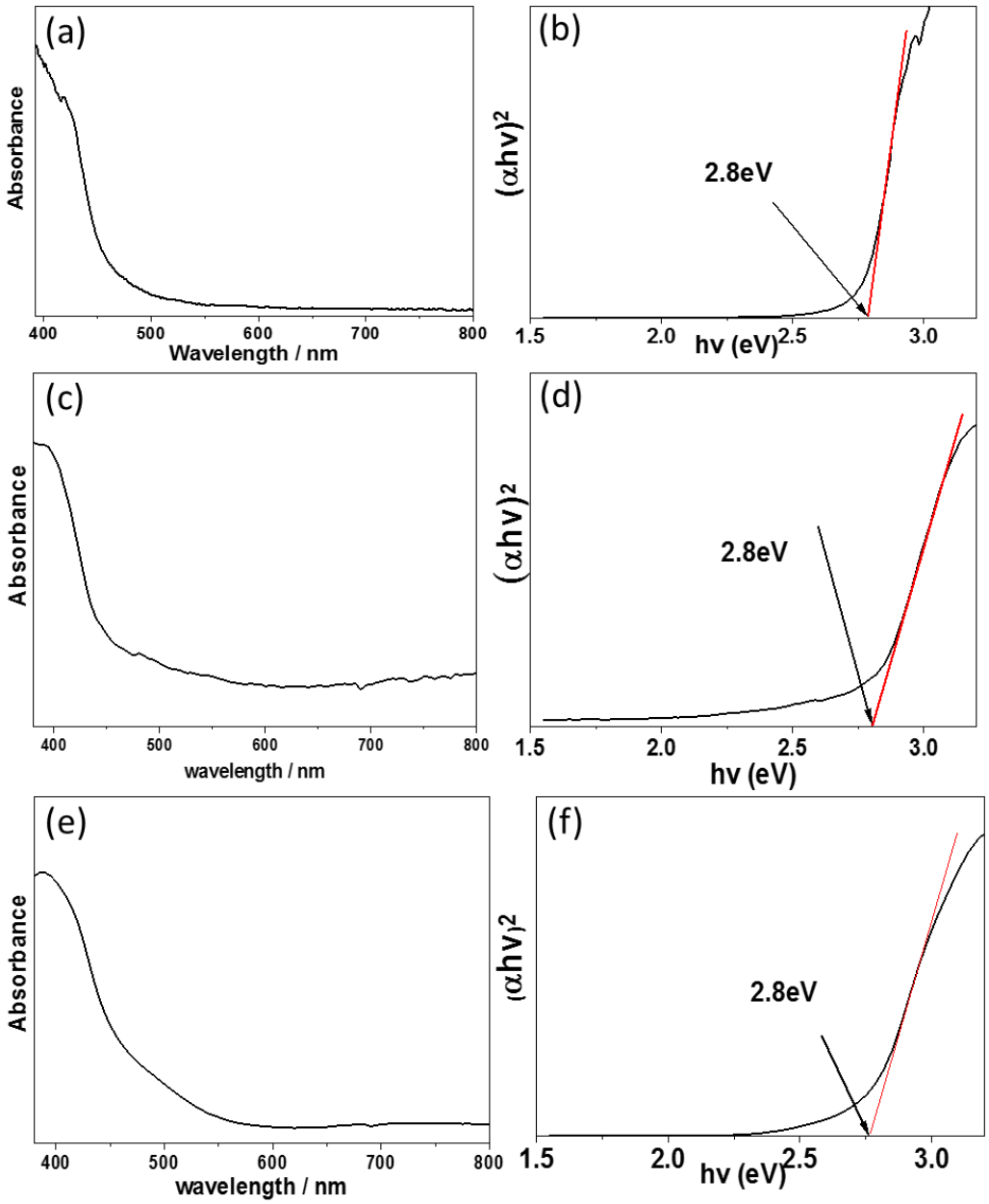

Fig. 40 (a) bulk-g-C_3N_4 UV-vis spectrum, (b) Tauc plot of bulk-g-C_3N_4 UV-vis spectrum; (c) compact-g-C_3N_4 film UV-vis spectrum (d) Tauc plot of compact-g-

C_3N_4 film UV-vis spectrum (e) porous-g-C_3N_4 film UV-vis spectrum and (f) Tauc plot of porous-g-C_3N_4 film UV-vis spectrum.

To further investigate the local structure of three samples, the FT-IR spectra (**Fig. 41**) of all samples are displayed. The intense band at 806 cm^{-1} is attributed to the out-of-plane bending vibration, characteristic of heptazine rings. The bands at 1311 and 1226 cm^{-1} could be assigned to stretching vibration of C–N(–C)–C or C–NH–C units. The intense bands at 1633, 1558, 1456 and 1406 cm^{-1} represent typical stretching vibration modes of heptazine-derived repeating units.[70]

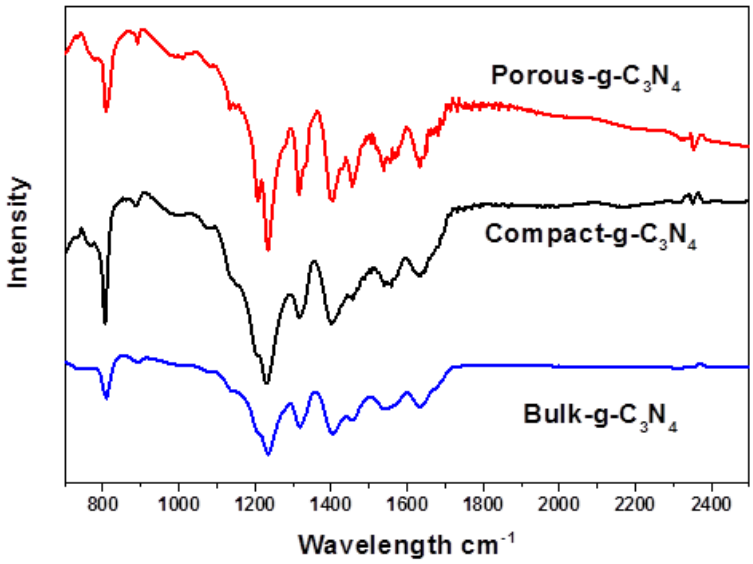

Fig. 41 FT-IR spectra of bulk-g-C_3N_4 film, compact-g-C_3N_4 film and porous-g-C_3N_4 film

Apart from FT-IR, another important technique XPS has been used to analyse the elemental composition, chemical state and electronic state of the elements on the surface of g-C_3N_4. (It is worth noticing that XPS can only determine the elements components on the surface of materials. To characterize the elements ratio in the bulk, such as g-C_3N_4, CHN techniques may be more suitable). XPS

spectra of bulk-g-C_3N_4 film, compact-g-C_3N_4 film and porous-g-C_3N_4 film are displayed in **Fig. 42**. As shown in **Fig. 42**a, the C1s XPS spectra show a peak at 288.1 eV corresponds to the binding energy of C-N-C bonds. The faint peak at 286.2 eV corresponds to C-O bonds and the peak centered at 284.8 eV is adventitious carbon.

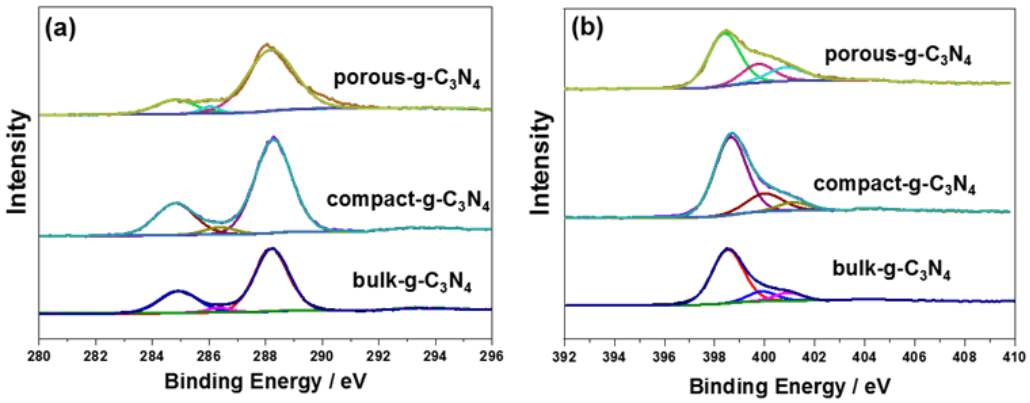

Fig. 42 (a) XPS C1s spectra and (b) XPS N1s spectra of bulk-g-C_3N_4 film, compact-g-C_3N_4 film and porous-g-C_3N_4 film

N1s XPS spectrum can be fitted to three components. The main peak located at 398.7 eV is attributed to C-N-C bonds. The other two peaks at higher energy account for C-$[N]_3$ (399.9 eV) and C-NH_x bonds (401.1 eV) respectively.[68] A percentage breakdown of different bonds is listed in **Table 5**. The atomic percentage of C-NH_x, which is recognized as the terminal groups of g-C_3N_4 structure, in compact-g-C_3N_4 film, bulk-g-C_3N_4 film and porous-g-C_3N_4 film are 8%, 13.6% and 18.8%, respectively. As a more ordered g-C_3N_4 structure has a lower percentage terminal group (C-NH_x), the structure of three samples, in order of decreasing completeness, are compact-g-C_3N_4; bulk-g-C_3N_4; and porous-g-C_3N_4, agreeing with the XRD and Raman analysis.

Table 5 Percentage of different bonds within the N1s spectra (in Fig. 42b) of porous-g-C_3N_4 film, bulk-g-C_3N_4 film and compact-g-C_3N_4 film

Bond	Binding Energy (eV)	Atomic % of bond (sample)		
		Porous-g-C_3N_4	Bulk-g-C_3N_4	Compact-g-C_3N_4
C-N-C	398.7	60.0%	71.8%	72.8%
N-$[C]_3$	399.9	21.2%	14.6%	19.2%
C-NH_x	401.1	18.8%	13.6%	8%

Furthermore, the C to N ratios in compact-g-C_3N_4, bulk-g-C_3N_4 and porous-g-C_3N_4 are calculated to be $C_3N_{4.12}$, $C_3N_{3.76}$ and $C_3N_{3.79}$ from the XPS spectra (**Table 6**). The C/N ratio in compact-g-C_3N_4 is the closest to the ideal ratio of 3:4 among three samples.

Table 6 C to N ratio in porous-g-C_3N_4 film, bulk-g-C_3N_4 film and compact-g-C_3N_4 film derived from XPS spectra

Sample	C_XN_Y
Porous-g-C_3N_4	$C_3N_{3.79}$
Bulk-g-C_3N_4	$C_3N_{3.76}$
Compact-g-C_3N_4	$C_3N_{4.12}$

With comprehensive characterizations of all samples, I want to further investigate the charge dynamics in these samples. Charge dynamics are investigated using the OCVD measurement which is proven to be a useful method to study the trap states and to estimate the lifetime of electrons in photoelectrodes.[162-165] OCVD plots obtained using bulk-g-C_3N_4, compact-g-C_3N_4 and porous-g-C_3N_4 photoelectrodes are displayed in **Fig. 43**.

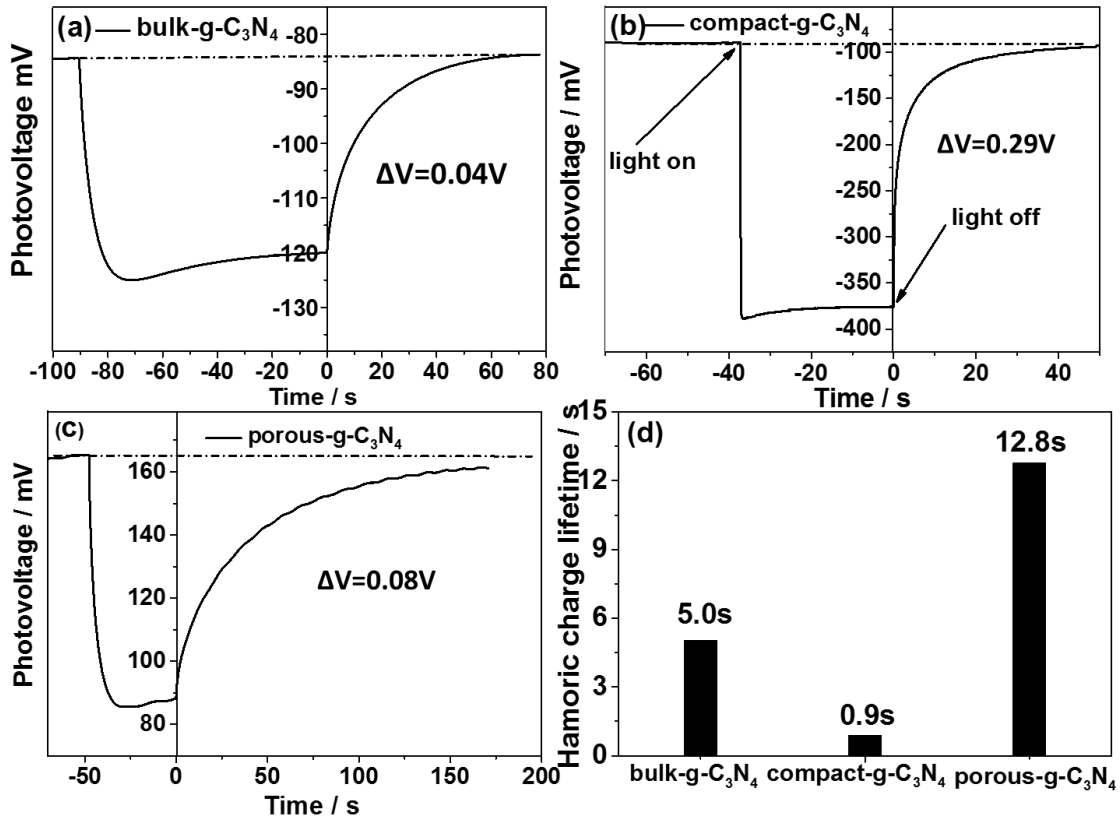

Fig. 43 Open Circuit Transient Voltage Decay (OCVD) plots of (a) bulk-g-C_3N_4, (b) compact-g-C_3N_4, (c) porous-g-C_3N_4 with 150W Xenon lamp illumination from the electrolyte-electrode (EE) side, (d) the calculated average charge-life time in bulk-g-C_3N_4 film, compact-g-C_3N_4 film and porous-g-C_3N_4 film (generated photovoltage ΔV is the difference in voltage between dark and illumination conditions).

Samples are placed in dark condition at the beginning of the experiment to avoid unwanted/erroneous effects from light absorption. Strong illumination was irradiated to the electrolyte-electrode (EE) side of the sample to generate a photovoltage. The generation of photovoltage is due to the recovery from the band bending at EE interface (when it is in the dark) of a semiconductor under illumination.[187] A decay in OCV was noted when the illumination was shut off. The electron lifetime is determined by fitting the decay curve to a biexponential function (**Fig. 44**).[162]

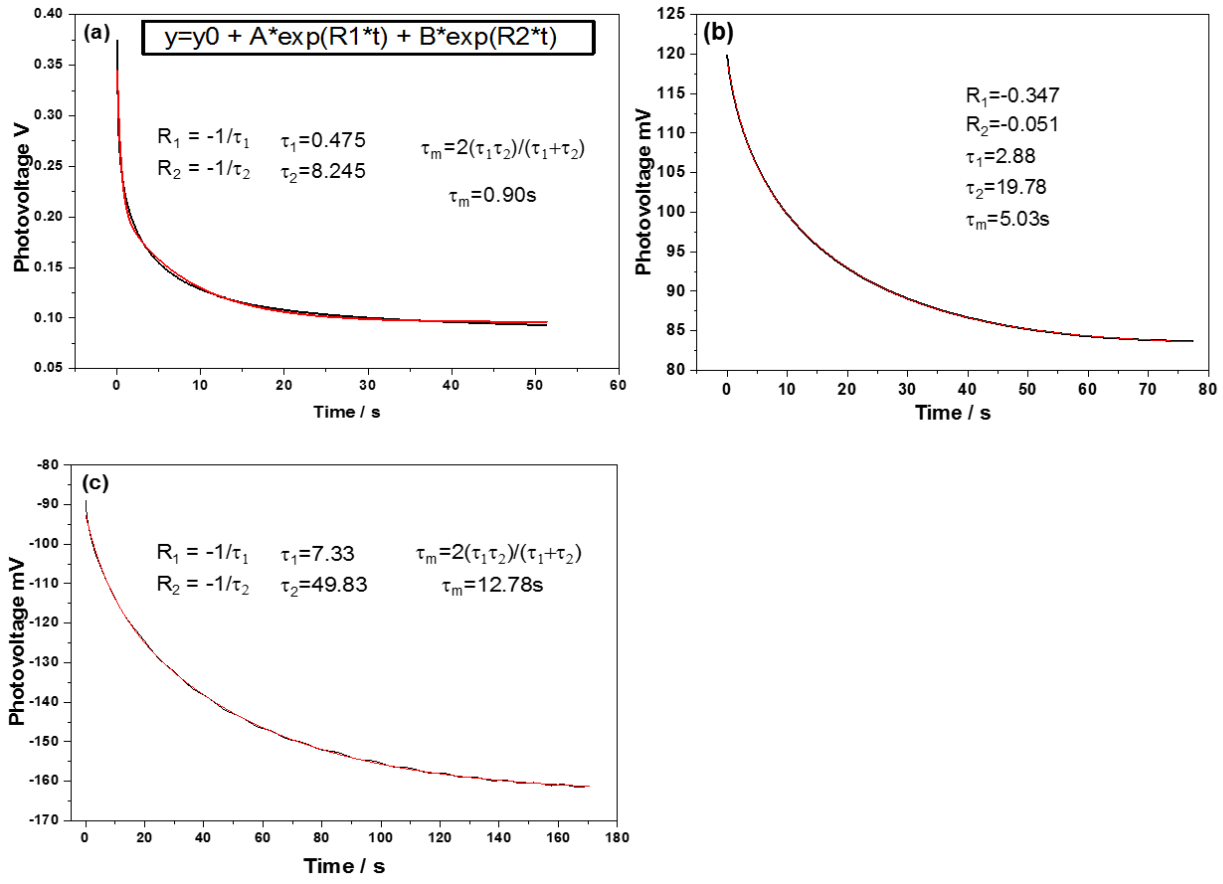

Fig. 44 Determination of harmonic mean of electron lifetimes τ_m by a biexponential fitting in (a) compact-g-C_3N_4 film (b) bulk-g-C_3N_4 film and (c) porous-g-C_3N_4 film.

When the light is on, a prompt increase in transient photovoltage is observed. Among the studied films, the compact-g-C_3N_4 showed the highest increase rate with the transient photovoltage (ΔV) of 0.29 V, whereas for porous-g-C_3N_4 and bulk-g-C_3N_4 showed relatively slow increase rate and photovoltages were 0.08 V and 0.04 V, respectively, indicating that electrons are being transferred fastest in the compact-g-C_3N_4 film among all samples. After turning off the light, different decay profiles were observed. Photovoltage decay in the compact-g-C_3N_4 is much faster than that in bulk-g-C_3N_4 and porous-g-C_3N_4. The average lifetimes of electrons are found to be 0.9 s, 5.0 s and 12.8 s for the compact-g-C_3N_4, bulk-g-C_3N_4 and porous-g-C_3N_4, respectively. The rapid photovoltage decay or short average electron lifetimes indicate facile electrons recombine with holes in the absence of an electron donor in the electrolyte, while a long lifetime of electrons observed in other samples is mainly due to severe electron trap effect.[162] Most of the long-lifetime electrons are deeply trapped and locates at low energy levels (more positive levels) that are insufficient to participate in redox reactions.[152] These deep trap states can act as recombination centers and hinders the migration of electrons in a photoelectrode towards the surface. As photogenerated electrons tend to migrate from the conduction band to the deep trap states (recombination centers) after excitation, reducing the deep trap states density can promote the charge transfer efficiency and thereby enhancing the photocurrent density of a photoelectrode. Apparently, significantly reduced electron average lifetime in compact-g-C_3N_4 film (0.9 s) indicates that the majority of photogenerated electrons are less likely deep-trapped compared to the bulk-g-C_3N_4 samples (5.0 s). Also, the long average electron lifetime in porous-g-C_3N_4 (12.8 s) suggested the presence of severe deep electron

trapping states. Therefore, the degree of the crystallinity shows a good correlation with trap states. Thus lesser the crystallinity is, higher the density of deeper trap states is.

More clues of trap states condition can be extracted from the photovoltage (ΔV) in **Fig. 43**. The situation is schematically shown in **Fig. 45**. In dark condition, when an electrical equilibrium is established between a semiconductor and a redox in an electrolyte ($E_{Red/Ox}$), the fermi level of the semiconductor aligns with $E_{Red/Ox}$. Under illumination, electrons are usually excited into the conduction band from the valence band, promoting the Fermi level of the semiconductor close to its initial level (before contacting with electrolyte) and reduce the band bending. ΔV represents the potential difference between the Fermi level of the semiconductor under illumination and the $E_{Red/Ox}$ in the electrolyte.[42] As the redox potential is fixed, higher photovoltage indicates a more negative electron Fermi level. In the compact-g-C_3N_4, the generated photovoltage (ΔV=0.29 V) is much larger than that in bulk-g-C_3N_4 film and porous-g-C_3N_4 film whose photovoltages are less than 0.1 V. It indicates that the compact-g-C_3N_4 under illumination has a more negative electron energy level than other two samples due to less deep trap states.

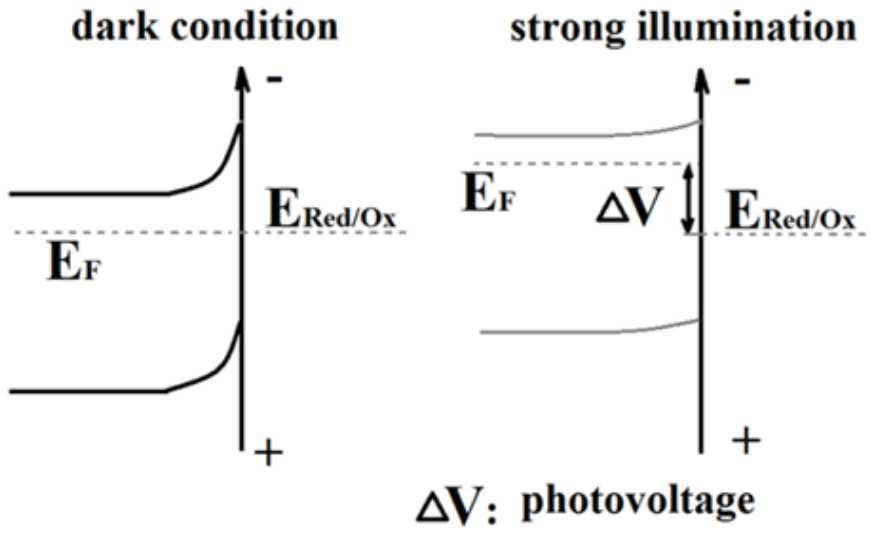

Fig. 45 Schematic of photovoltage generation for an n-type semiconductor

To summarise, there is a clear correlation of trap-state conditions with the crystallinity of g-C_3N_4 films which is associated with the decay lifetime. The compact-g-C_3N_4 film with the most ordered structure seems to consist of shallow trap states, resulting in the shortest average electron lifetime (0.9 s) and highest photovoltage (0.29 V) among all three samples. In contrast, both the bulk-g-C_3N_4 film and porous-g-C_3N_4 film have deep trap states due to their low crystallinity, leading to long charge lifetime (5.0 s for bulk-g-C_3N_4 film and 12.8 s for porous-g-C_3N_4 film) and low photovoltage (0.04V for bulk-g-C_3N_4 film and 0.08V for porous-g-C_3N_4 film). It could be reasonable that high crystallinity of a semiconductor resulted in fewer defects in structure thereby reducing the deep trap states density.

The capacitances of the bulk-g-C_3N_4 film, compact-g-C_3N_4 film, porous-g-C_3N_4 film and FTO substrate at different potentials are also derived from the impedance plots (**Fig. 46**) and shown in **Fig. 47**, by fitting the data with the equivalent circuit as shown in **Fig. 48**.

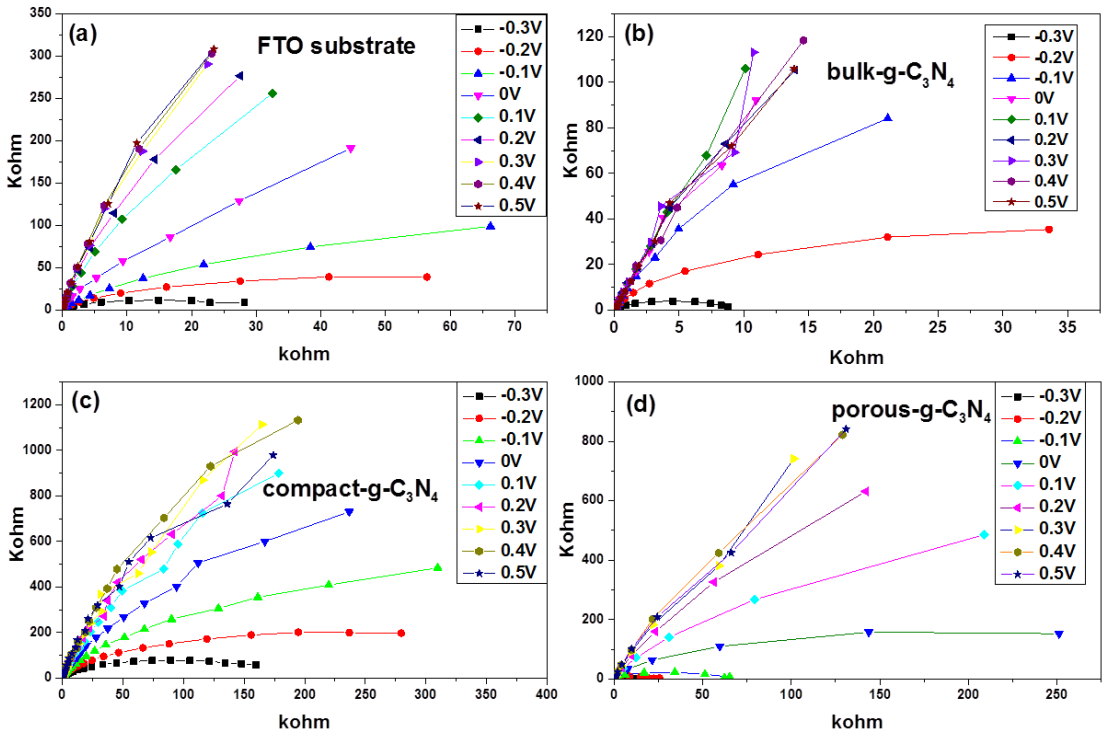

Fig. 46 EIS spectra of (a) FTO substrate, (b) bulk-g-C_3N_4 film, (c) compact-g-C_3N_4 film and (d) porous-g-C_3N_4 film; potential range -0.3 V to 0.5 V vs Ag/AgCl; frequency 10 KHz to 0.1Hz; amplitude: 0.01V.

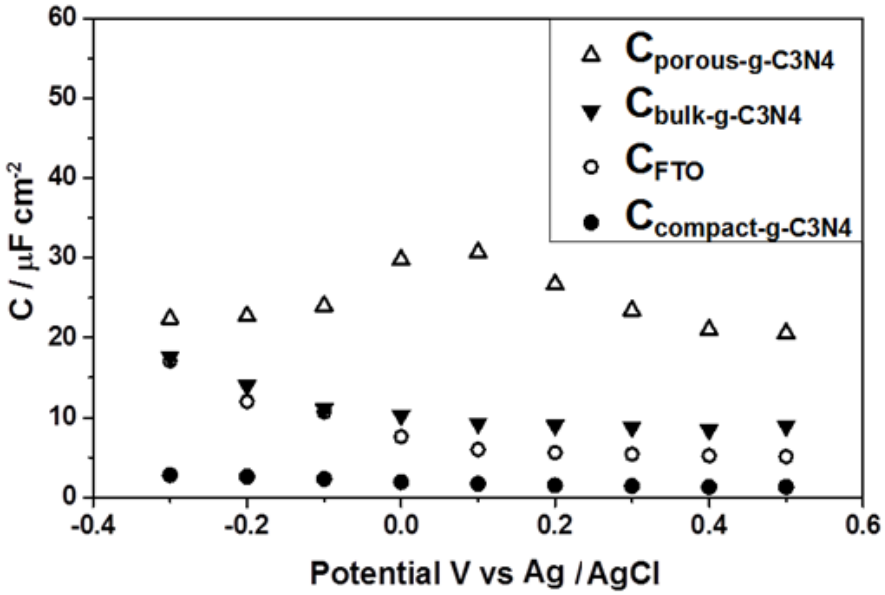

Fig. 47 Capacitance of bulk-g-C_3N_4 film, compact-g-C_3N_4 film, porous-g-C_3N_4 film and FTO substrate

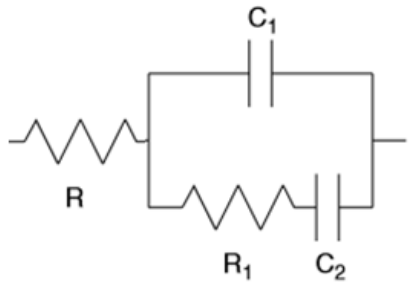

Fig. 48 Equivalent circuit representing the photoanode/electrolyte system used for EIS data modelling. R is the system resistance, C_1 is the space charge layer capacitor, R_1 and C_2 are the surface recombination impedance.

The bulk-g-C_3N_4 film, compact-g-C_3N_4 film, porous-g-C_3N_4 film and FTO substrate show the space charge layer capacitance of 10.8 μF/cm^2, 1.9 μF/cm^2, 24.6 μF/cm^2 and 8.3 μF/cm^2, respectively. Apparently, bulk-g-C_3N_4 film and porous-g-C_3N_4 film exhibit 6 and 13 times higher capacitance than the compact-g-C_3N_4 film due to their non-uniform morphology/severe trap states[138]. It is noticed that compact-g-C_3N_4 film only has a 1/4 capacitance as that of the FTO substrate. Although the compact-g-C_3N_4 film grew on the top of the FTO surface, the high-quality carbon nitride film screens the electronic effect of FTO substrate well and results in lower capacitance.[188]

Consequently, the photocatalytic performances of the bulk-g-C_3N_4 film, compact-g-C_3N_4 film and porous-g-C_3N_4 film were examined in a PEC system, and the results are shown in **Fig. 49**a, b and c. Apparently, the compact-g-C_3N_4 film exhibits the highest anodic photocurrent density (e.g. 180 μA/cm^2 at 0.6 V vs Ag/AgCl) among three photoelectrodes due to its significantly reduced deep trap-state density and surface states caused by high crystallinity and uniform morphology, as discussed earlier. In contrast, the bulk-g-C_3N_4 film and porous-g-C_3N_4 film with low crystallinity and rough morphology resulting into deeper

trap states, only exhibited less than 30 times lower photocurrent density (5 μA/cm^2 at 0.6 V vs Ag/AgCl). It reveals that the significantly mitigated deep trap states in the g-C_3N_4 films improve charge transfer across the film and facilitates charge collection on the electrode and electrolyte interface, resulting in a significantly enhanced photocatalytic performance.

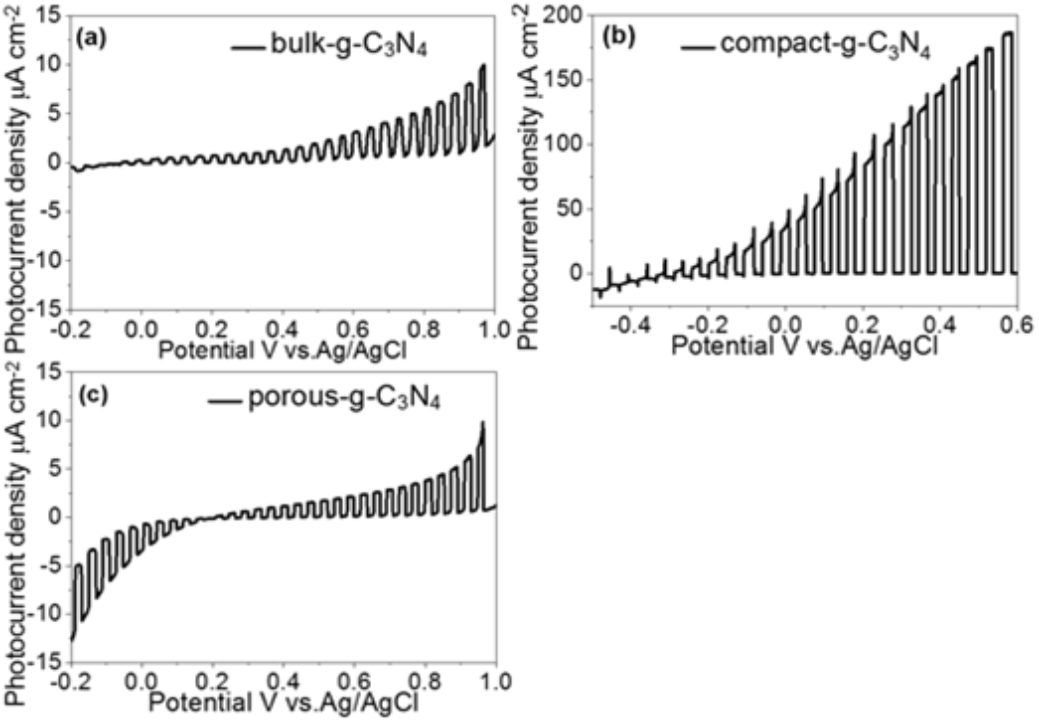

Fig. 49 Photocurrent vs potential plot of (a) bulk-g-C_3N_4 film, (b) compact-g-C_3N_4 film and (c) porous-g-C_3N_4 film using 150 W Xenon lamp illuminating from the substrate-electrode (SE) side (the 150 W Xenon lamp contains much stronger UV light irradiation than the stimulated one sun illumination), electrolyte: 0.1 M Na_2SO_4, pH=6.5.

Charge diffusion length is a key factor that determines the photoelectrodes' performance. The diffusion length indicates the average distance that the carrier can move before it is recombined. A long charge diffusion length guarantees the efficient charge transfer across the film. Metal oxides photoelectrodes vary their diffusion length with materials. For example, TiO_2 has a ~10 micrometer

diffusion length by adopting TPV method by Durrant *et al*.,[138] while Fe_2O_3 has a much smaller diffusion length of 2 - 4 nm. The charge diffusion lengths of polymers photoelectrodes have much less investigated. TPV has been used to determine this important factor for the g-C_3N_4 film. In this method, a continuous strong light source was irradiated onto the sample to generate electron-hole pairs. Deep trap states were then occupied during the illumination. After the equilibrium between charge generation and charge consumption (filling the deep trap states and recombination) was achieved, a single pulse light was applied onto the EE side of the electrode. The photovoltage rise and decay corresponding to the pulse light was recorded, and electron diffusion length has been derived as follow.

The electron diffusion length for the benchmark photocatalyst (compact-g-C_3N_4-film) was measured using a range of light pulse intensities (25 w – 100 w). It is observed that the amplitude of the transient photovoltage changed from 5 mV to 20 mV by tuning the output power of the pulse light. Time constants for photovoltage rise (τ_{rise}) and decay (τ_n) are determined by using the initial phase of the photovoltage rise and decay in **Fig. 50**. The duration of the pulse light is around 1ms. The corresponding τ_{rise} and τ_n are calculated using equation 19 and the resultant electron diffusion length (L) is then determined by equation 20 and 21[138, 189], where d is the thickness of the film; C_{c3n4} is the capacitance of carbon nitride film; C_{sub} is the capacitance of FTO substrate; τ_{rise} is the time constant of photovoltage rise; τ_n is the time constant of photovoltage decay, D_n is the diffusion coefficient, and L is the charge diffusion length The determined results are represented in **Fig. 50**b.

$$\tau = -\frac{K_B T}{q}\left(\frac{dV_{oc}}{dt}\right)^{-1} \quad \text{(Equation 19)}$$

$$D_n = \frac{d^2}{\pi^2}\left(1 + \frac{3}{1+\left(\frac{3}{\sqrt{2}}-1\right)\frac{C_{C3N4}}{C_{sub}}}\right)\left(\frac{1}{\tau_{rise}} - \frac{1}{\tau_n}\right)$$ (Equation 20)

$$L = (D_n \tau_n)^{1/2}$$ (Equation 21)

It is observed that the effective electron lifetime (τ_n) decreases with an increase in pulse intensity from 950 ms at 25 W to 350 ms at 100 W. At high light intensity, the reduced electron lifetime could be due to increased rate of recombination of electron-hole pairs.[147] As expected, though a series of light pulse intensities result in different values of τ_{rise} and τ_n, the electron diffusion length in the g-C_3N_4 film is *ca.* 1000 nm. As an intrinsic property, it remains independent of the pulse light intensity. Compared to the thickness of the compact-g-C_3N_4 film (600 nm), such a long electron diffusion length can guarantee the efficient charge transfer and collection across the film, which significantly contributes to its excellent PEC performance.

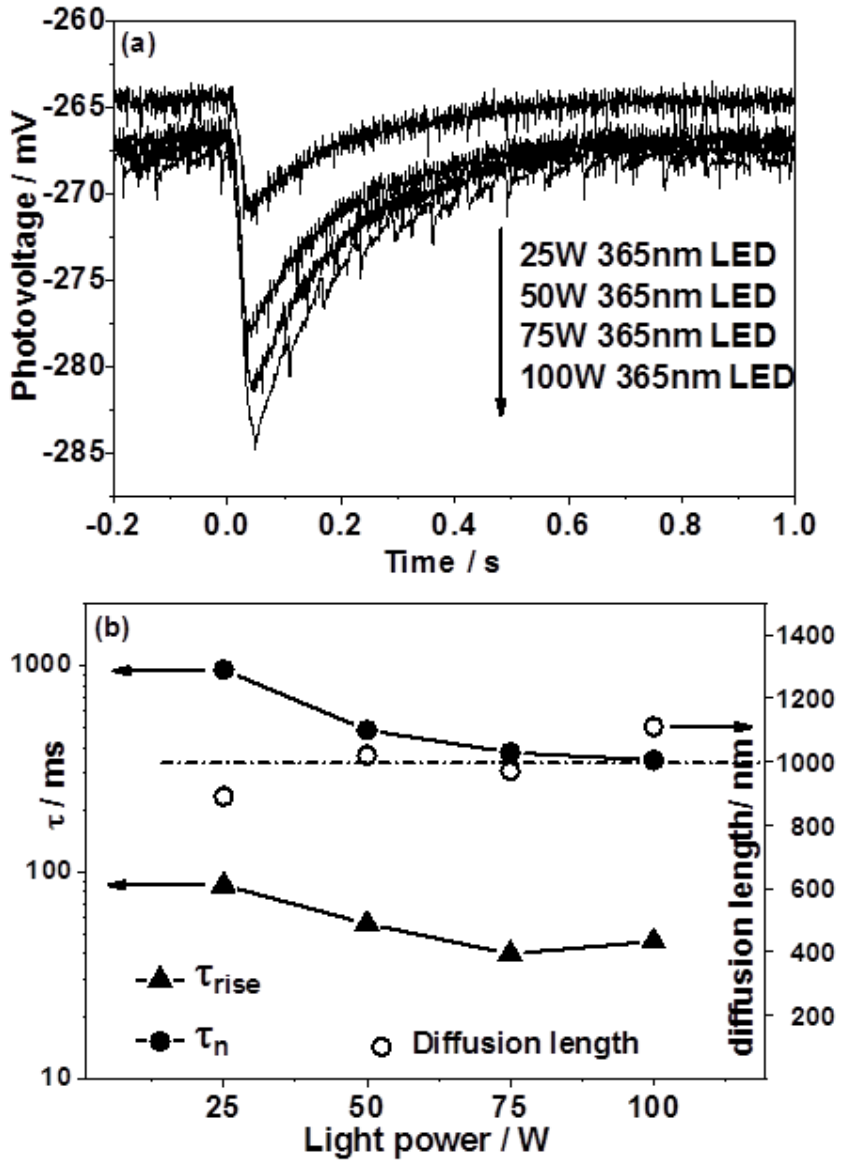

Fig. 50 (a) Transient photovoltage vs time at varying light power, and (b) Dependence of photovoltage rise time (τ_{rise}), effective electron lifetime (τ_n) and charge diffusion length of the compact-g-C_3N_4 sample on light power.

To further confirm the intrinsic charge diffusion length, TPV measurements have been performed on another sample S1 which was also prepared by the rapid thermal vapor condensation method. By adjusting the synthesis time, the thickness of sample S1 was manipulated to 800 nm (in **Fig. 51**). The diffusion length determined form TPV measurements against different pulse intensities

are displayed in **Fig. 52**a. The average charge diffusion length is determined to be 950 nm. From this, it is evident that the charge diffusion length does not change with the thickness of the films, at least in the range studied in this work. Thus the average electron diffusion length of the g-C_3N_4 film fabricated by the rapid thermal vapor condensation method is *ca.* 1000 nm. Photocurrent response of sample S1 is shown in **Fig. 52**b. The photocurrent density is *ca.* 130 μA/cm^2 at 0.6 V vs Ag/AgCl, which is smaller than that observed in the 600nm thick compact-g-C_3N_4 film (180 μA/cm^2), while it is still 20 times higher than the bulk g-C_3N_4 It is reasonable that a film thickness smaller than its charge diffusion length is beneficial for its PEC performance.

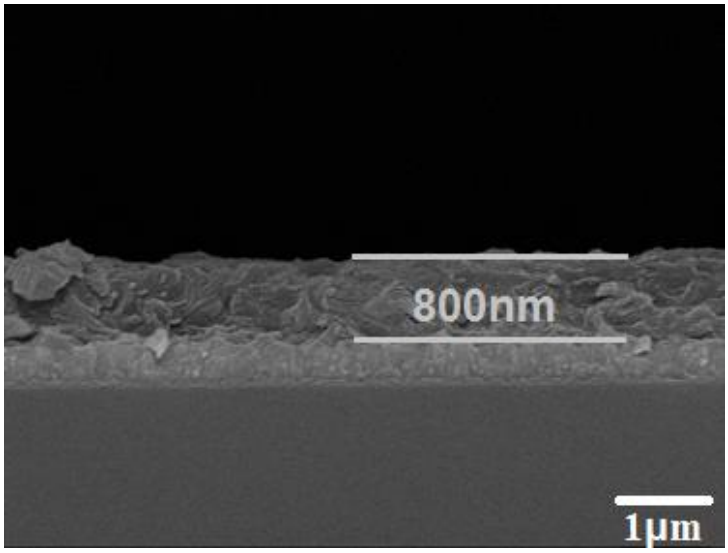

Fig. 51 Side SEM side view of g-C_3N_4 S1 sample

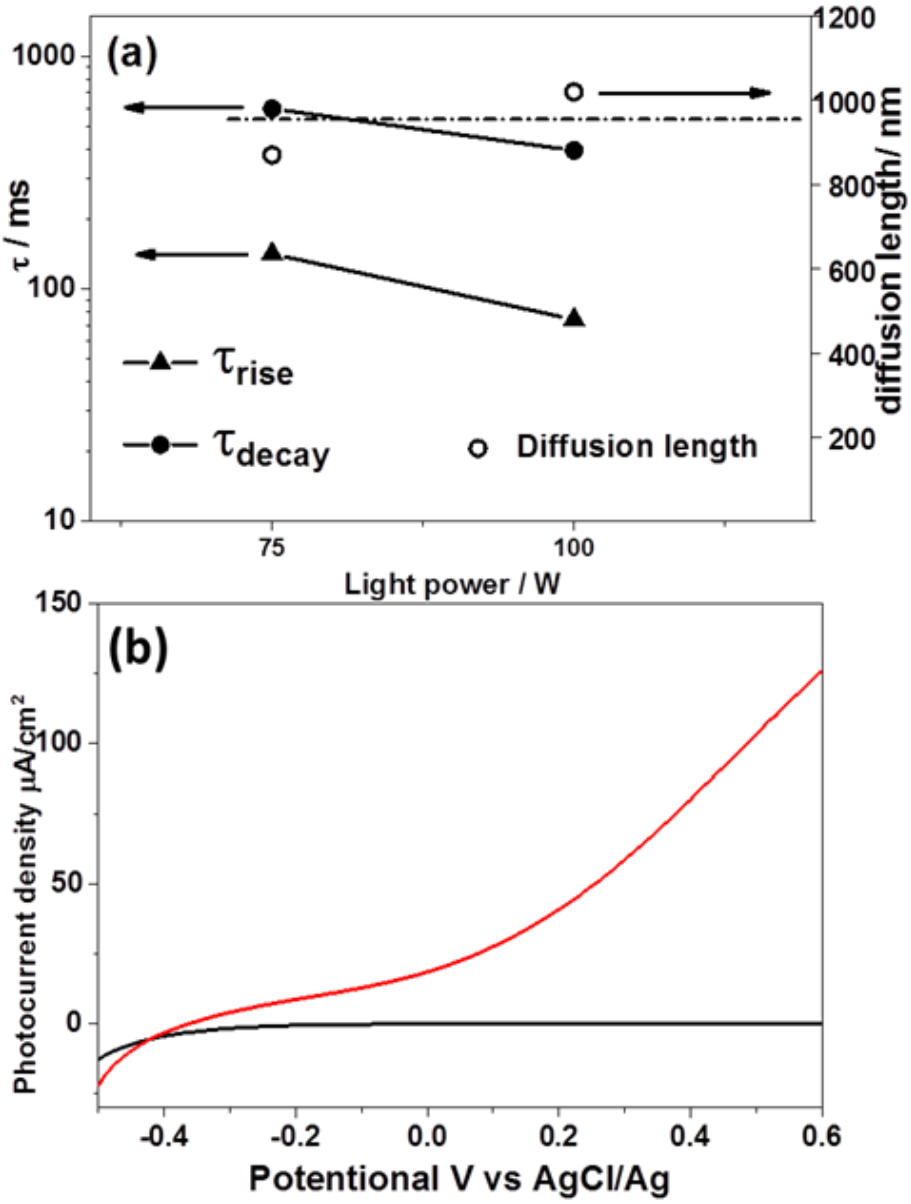

Fig. 52 (a) Dependence of photovoltage rise time (τ_{rise}), effective electron lifetime (τ_n) and charge diffusion length of light power of g-C_3N_4 S1 sample. (b) photocurrent vs potential plot of S1 sample using 150W Xenon lamp illuminating from the substrate-electrode (SE).

In addition, TPV measurements show no reliable and reproducible response for bulk-g-C_3N_4 as well as porous-g-C_3N_4 samples. It is believed that short diffusion lengths caused by a large number of deep traps states make such measurement difficult.

To further confirm the electron diffusion length in compact-g-C_3N_4, the PEC performance measurements of two samples with forward-illumination and back-illumination have been performed, respectively. One film has a thickness of *ca.* 500nm, which is much smaller than our calculated diffusion length (1000nm). The other sample has a thickness of *ca.* 900nm, which is approaching the calculated diffusion length. The I-V curves (1^{st} cycle) of two samples with forward/back-illumination are presented in **Fig. 53** along with their SEM side view. In **Fig. 53**a, the sample with a thickness of 500 nm has shown a slightly higher photocurrent density with forward-illumination (illumination from EE side) than with back-illumination (illumination from SE side). It indicates that electrons can sufficiently travel across the film and the film thickness (500 nm) is much smaller than the electron diffusion length in the compact-g-C_3N_4 film. However, in **Fig. 53**c, when the film thickness is similar to the diffusion length (900nm vs 1000nm), the 900nm-thick g-C_3N_4 has shown a 1/3 lower photocurrent density with forward-illumination than that with back-illumination. It should be noted that in this film electrons have to travel across the film if the illumination is from EE side, while holes have to travel across the film if the illumination is from the SE side. The lower performance with forward-illumination than the back-illumination in 900nm-thick film is because when the film thickness is similar to the electron diffusion length, a part of electrons cannot freely travel across the film but recombine. It causes a loss of electrons reaching the SE interface and, therefore, a lower photocurrent density.

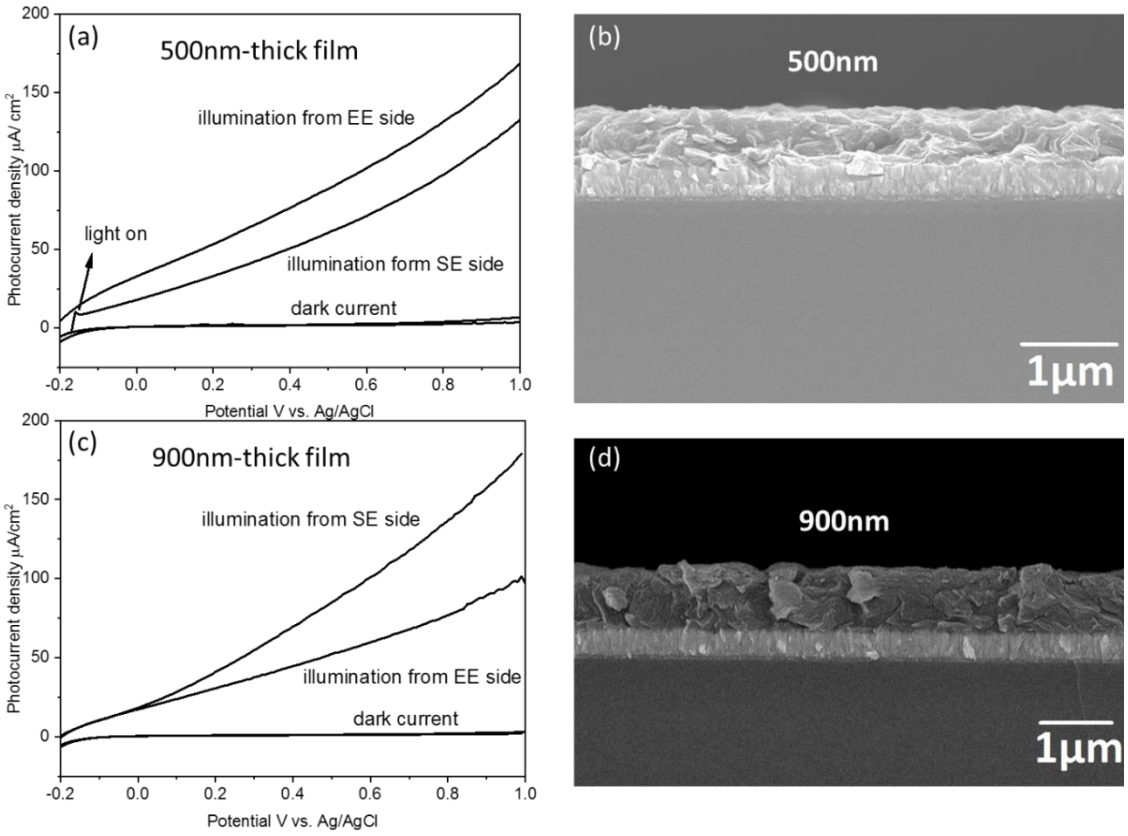

Fig. 53 (a) I-V curve (1st cycle) of a 500 nm-thick compact-g-C_3N_4 film with illumination from EE (electrode/electrolyte) and SE (substrate/electrolyte) side; (b) SEM side view of the 500 nm-thick compact-g-C_3N_4 film; (c) I-V curve (1st cycle) of a 900 nm-thick compact-g-C_3N_4 film with illumination from EE (electrode/electrolyte) and SE (substrate/electrolyte) side; (b) SEM side view of the 900 nm-thick compact-g-C_3N_4 film.

4.4 Conclusion

In summary, it is demonstrated that there is a good relationship between crystallinity and the trap states in graphitic carbon nitride. Worse crystallinity results in deeper trap states, which would lead to unusual long-lived charge carrier that does not guarantee good photoelectrochemical performance. Low deep trap-state density and long electron diffusion length could be achieved in

g-C_3N_4 films by manipulating its crystallinity and morphology. The significantly shorten charge lifetime, large transient photovoltage, essentially reduced capacitance, all illustrate the low deep trap state density in a well crystallized, closely packed, high quality g-C_3N_4 thin film. The intrinsic property of the charge diffusion length in g-C_3N_4 electrodes was determined to be *ca.* 1000 nm. The reduced deep trap state density and the long electron diffusion length finally contributed to the facilitated charge transfer, efficient charge collection in the film and excellent photocatalytic performance of 180 μA/cm^2 at a bias of +0.6 V vs Ag/AgCl under full arc illumination (150W Xenon lamp), which is 30 times higher than the bulk g-C_3N_4 film prepared by carbon nitride powders widely used in the photocatalytic suspension system. This study intensifies the effect of trap states on the photoelectrochemical performance of benchmark polymer photocatalyst and determines the electron diffusion length of g-C_3N_4. It will further encourage the mechanistic study of highly efficient polymer photoelectrode for photosynthesis in the future.

5 Nanojunction Polymer Photoelectrode for Efficient Charge Transport and Separation

Although crystalline g-C_3N_4 has a long electron diffusion length measured in Chapter 4, its PEC performance is still very limited probably due to the low charge carrier density and severe charge recombination on the surface. To solve this problem, a novel one-step construction approach has been developed to synthesise a nanojunction metal-free photoanode, composed of B-doped carbon nitride nanolayer and bulk carbon nitride (this nanojunction is donated as s-BCN). This type of nanojunction overcomes a few intrinsic drawbacks of carbon nitride film, e.g. severe charge recombination and slow charge transfer. For the optimum samples, the top layer of the nanojunction has a depth of *ca.* 100 nm and the bottom layer is *ca.* 900 nm. This nanojunction photoanode results into a 10 fold higher photocurrent than compact-g-C_3N_4 photoanode with a recorded photocurrent density of 103.2 μA/cm^2 at 1.23V vs RHE under one sun condition (AM 1.5, 100mW/cm^2) and a high incident photon-to-current efficiency (IPCE) of *ca.* 10% at 400 nm. The EIS, MS and IMPS spectroscopies all prove such enhancement is mainly due to more than 10 times faster charge transfer rate at electrode/electrolyte interface and nearly 3 times higher conductivity due to the nanojunction structure.

5.1 introduction

Despite the potential to be an efficient photoelectrode mentioned in previous chapters, there are limited reports on the PEC application of g-C_3N_4 due to a number of problems, such as a high charge recombination rate, slow charge transfer and high electrical resistance of the intrinsic graphic carbon nitride.[117]

To overcome these drawbacks, variable strategies have been used during the process of carbon nitride film fabrication, including reducing grain boundary defects of G-CN via a sol-processing,[117] printing carbon nitride on a substrate to build micro-contact between carbon nitride and the substrate,[120] and improving optical and electronic properties of carbon nitride by monomers design.[119] However, even in the presence of sacrificial agents, the efficiency of the synthesised photoanodes is still very moderate.[119, 190] Elemental doping is an effective strategy to modify the electronic properties of a semiconductor and improve its photocatalytic performance,[16, 61-62, 191-192] which has also been used for carbon nitride.[61, 193] However, a detrimental effect of bulk-doped semiconductors is the increasing charge recombination centers due to doping,[194-195] especially in a PEC system where effective diffusion of charge carriers to the surface is crucial, resulting in very low efficiency.

As water-splitting reaction takes place on a surface, doping the surface of a photoelectrode can significantly affect the surface state, morphology, surface charge transfer and electrode/electrolyte interfacial properties[146, 196-197] without changing the bulk properties of the photoelectrode. Furthermore, the formation of surface layer/bulk heterojunction may help charge transfer and separation, leading to an improved photocatalytic performance, which has been justified in powder system.[198-202]

Herein, for the first time, an efficient one-step approach has been developed to control the surface layer of metal-free carbon nitride film fabricated on FTO substrate. Remarkably, the resulting nanojunction film, composed of 100 nm B-doped carbon nitride and 900 nm bulk carbon nitride, exhibits 10 times higher PEC performance than compact-g-C_3N_4 film. I further investigate the effect of

the boron-doped carbon nitride nanolayer on interfacial charge transport and recombination, which supports the extraordinary photocatalytic activity of the nanojunction photoanode.

5.2 Experimental

Synthesis methods

Compact-g-C_3N_4 and s-BCN films were synthesised by a new “rapid thermal vapour deposition” method. 50mg Dicyandiamide (Alfa Aesar, 99%) and 0 wt%-5 wt% Boric Acid (Sigma-Aldrich, 99.5%) were mixed and dissolved with DI water in a Φ35 mm petri dish. After drying at 70°C for 1h, the mixture of Dicyandiamide and Boric Acid were crystallized and adhered to the internal surface of the petri dish. A piece of 20 mm×20 mm FTO glass used as the substrate was placed on a slightly concave crucible lid and covered by the petri dish. The sample was calcined in a 600°C preheated Muffle furnace (Carbolite, CWF 1300) for 20min and quenched to the room temperature in air.

Characterisation

XRD patterns were taken by a D8 Bruker Diffractometer. UV-Vis absorption spectra were collected using a Shimadzu UV-Vis 2550 spectrophotometer fitted with an integrating sphere using $BaSO_4$ as the reference material. FTIR spectroscopy was performed on a Perkin-Elmer 1605 FT-IR spectrometer in the wavenumber range from 400 – 4000 cm^{-1} with a resolution of 0.5 cm^{-1}. Raman spectroscopic measurements were performed on a Renishaw InVia Raman Microscope, using a 325 nm excitation laser, and a wavenumber range from 100 – 3000 cm^{-1}. XPS measurements were done on a Thermoscientific XPS K-alpha surface analysis machine using an Al source. The analysis was

performed on the Casa XPS software. SEM images were taken by a JOEL JSM-7401F Scanning Electron Microscope.

Photocatalytic analysis

The photoelectrochemical properties were investigated in a conventional three-electrode cell using an electrochemical analyzer (IVIUM Technologies). The as-prepared film, a Pt net and an Ag/AgCl electrode were used as the working, counter and reference electrodes, respectively. Sunlight was simulated with a 150 W xenon lamp (Newport) and AM 1.5 filter (Newport) (approximately on sun condition). The light intensity was set using a calibrated crystalline silicon solar cell, equivalent to global AM 1.5 illumination at 100 mW/cm^2. (Again, AM 1.5 illumination has a very weak UV irradiation compared to 150W Xenon lamp) The photocurrent of samples was measured in 0.1M Na_2SO_4 aqueous solution (pH=6.5). Samples were illuminated from the back-side (FTO substrate/semiconductor interface) and the mask-off irradiated area was 0.28 cm^2. Cyclic voltammetry measurements were performed at a scan speed of 10mV s^{-1}. The potentials of the working electrodes can be calculated by the formula $V_{RHE}=V_{Ag/AgCl} + 0.059\ pH + 0.1976\ V$, where VRHE is a potential vs. a reversible hydrogen potential, $V_{Ag/AgCl}$ is a potential vs. Ag/AgCl electrode. The Mott–Schottky curves were measured at a certain DC potential range with an AC amplitude of 5 mV and a frequency of 1000Hz under dark condition. Electrochemical impedance spectra (EIS) were measured at 0.0 V vs Ag/AgCl. A sinusoidal ac perturbation of 5mV was applied to the electrode over the frequency range 0.1 Hz−10 kHz. The IPCE was obtained under light irradiation using a different wavelength generated by monochromatic filters with a 10 nm band-width. Intensity-modulated photocurrent spectroscopy (IMPS) was

conducted using a potentiostat (IVIUM technology) in a three-electrode configuration. Modulated illumination (LED: ultraviolet 365nm) was provided by a ModuLight module (IVIUM technology).

The equation 22 was used for IPCE calculation[6]:

$$IPCE = \frac{1240 * I_{ph}}{P * \lambda}$$ (Equation 22)

Where P and λ are incident light intensity (μW cm^{-2}) and wavelength (nm), respectively; I_{ph} is the photocurrent density (μA cm^{-2}).

5.3 results and discussion

The boron-doped top nanolayer and g-CN bulk layer were prepared by modifying the vapour deposition method as shown in **Fig. 54**, where DCDA was replaced by a mixture of boric acid and DCDA.

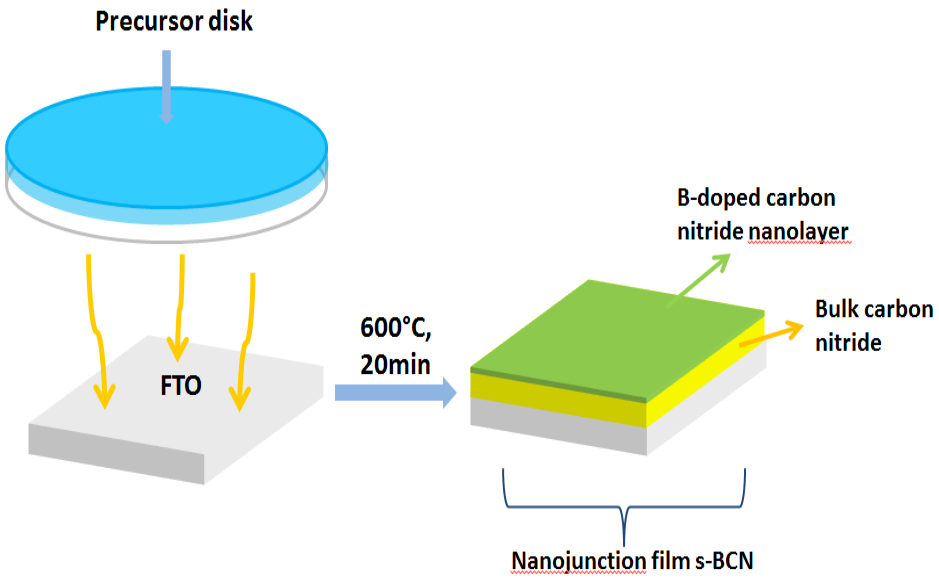

Fig. 54 Illustration of one step depositing s-BCN on FTO substrate

The XRD pattern of both s-BCN and compact-g-C_3N_4 were very similar, indicating that the bulk of the film was compact-g-C_3N_4 and that the top layer of s-BCN is too thin to be observed by XRD (**Fig. 55**).

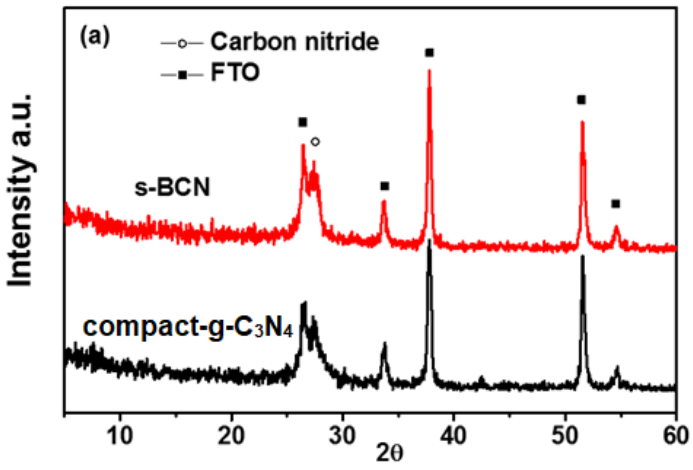

Fig. 55 XRD patterns of compact-g-C_3N_4 and s-BCN

The chemical environment of boron in the top layer of s-BCN was determined by X-ray photoelectron spectroscopy (XPS) and Nuclear Magnetic Resonance (NMR) spectroscopy. In **Fig. 56**a, a single B1s peak centered at 191.7 eV with a FWHM of 1.56 eV was detected which can be assigned to a B-N-C bond connection.[203-204] The binding energy of boron in s-BCN is higher than that of h-BN (190.1eV),[205] suggesting boron atoms in s-BCN structure are more electropositive. This can be explained by one boron atom bonding with three nitrogen atoms in the heptazine.[203] XPS B1s peak of B-C bonds was usually centred at 189.4eV,[203] which is absent in the s-BCN structure. The boron content in s-BCN surface layer could be controlled by adjusting the boron amount in the precursor. The optimum s-BCN sample had a real boron content of 0.6% on the surface layer determined by XPS. ^{11}B chemical shift data was

collected with BF_3Et_2O as the reference to investigate the structural details of boron incorporation into CN matrix. ^{11}B solid-state MAS NMR spectrum shows one single peak at -5.93 ppm which can be assigned to boron substituting "bay-carbon" site[206] (**Fig. 56**b). The negative chemical shift indicates the stronger shielding effects and increased electron cloud density around the B nuclei, which can be explained by electrons flowing to B atom by forming conjugated π bonds with surrounding three N atoms. XPS and NMR spectra indicate that boron atoms have most likely substituted for carbon in $CN_2(NH_2)$ cluster. XPS depth profile of B1s (**Fig. 56**a) shows that the boron concentration drops with depth. Negligible boron signal can be observed at 100 nm below the surface, suggesting that boron doping is limited to the 100 nm surface of s-BCN. STEM elemental mapping in **Fig. 57** demonstrates the evenly distributed boron doping on the surface.

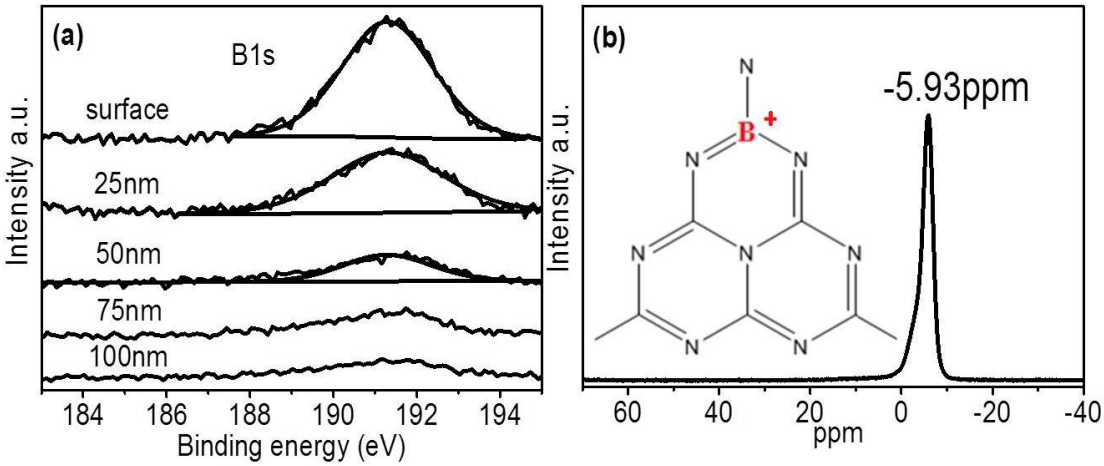

Fig. 56 a) XPS depth-profile of B1s in s-BCN film; b) Solid state ^{11}B MAS NMR spectra of s-BCN

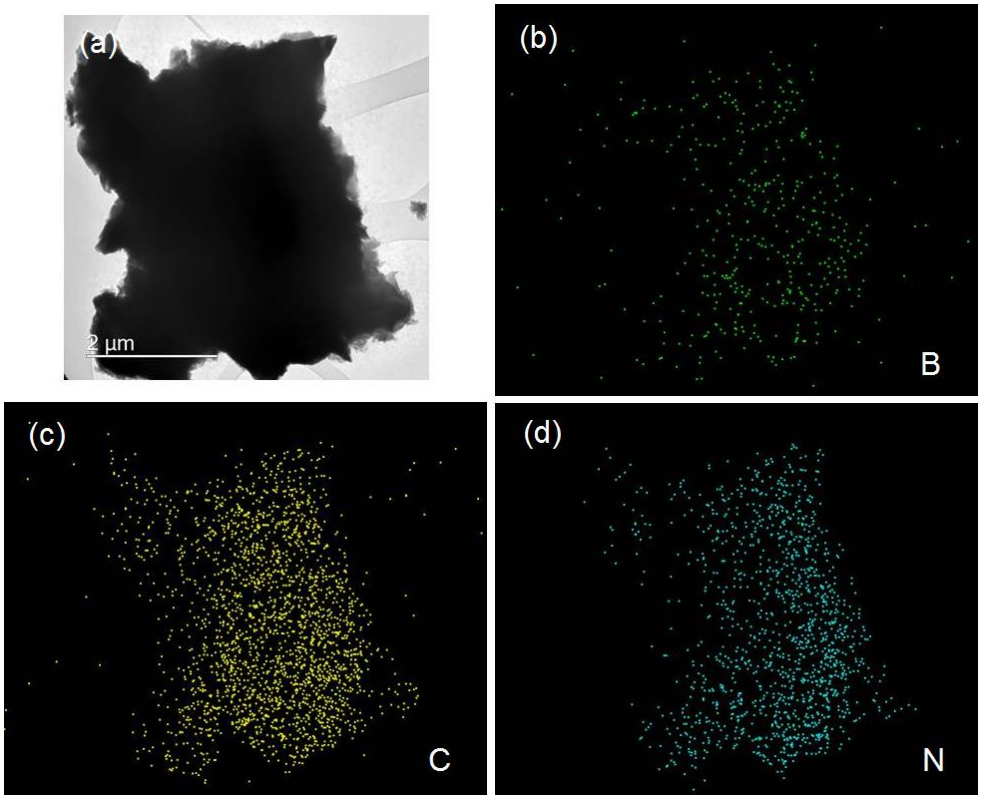

Fig. 57 a) TEM top view of s-BCN sample (the sample flake was scraped from the FTO substrate), b-d) boron, carbon and nitrogen elemental mapping.

It is very interesting that the boron only exists on the top layer of compact-g-C_3N_4. Therefore, the fabrication process of the s-BCN film is further investigated by observation of samples synthesised for 5 min, 10 min, 15 min and 20 min (**Fig. 48**), which evidences the evolution from compact-g-C_3N_4 to the s-BCN photoanode. A clear difference is observed among samples synthesised at different times in terms of morphology, thickness and boron concentration. A transformation of morphology with calcination time is observed, from a loosely compact surface to a rough and dense morphology. A synthesis time of 5 minutes produced a *ca.* 1.5 µm-thick carbon nitride film on the substrate with negligible boron appearing on the surface. This is due to the process of boron doping being much slower than carbon nitride polymerization. At 10 mins, the carbon nitride film grew to *ca.* 2.2 µm and small boron peaks appeared in the

B1s XPS spectrum. This suggests that further polymerization of carbon nitride with boron doping is happening at the same time. At 15 mins, the thickness of the carbon nitride film was reduced to *ca.* 1.7 μm and further to 1.0 μm (100 nm B doped carbon nitride and 900 nm carbon nitride) at 20 mins, while boron doping concentration on the surface continued to increase. The reduction in thickness is most likely due to polymerization of carbon nitride and decomposition of a less stable structure. The accumulation of boron on the surface implies that the good thermal stability of boron-doped carbon nitride is probably due to nitrogen being stabilized by bonding to the boron atoms[203]. In **Fig. 58**f, the XPS N1s peak also demonstrates a change at 400 eV with calcination time, which is believed to relate to the boron doping concentration.

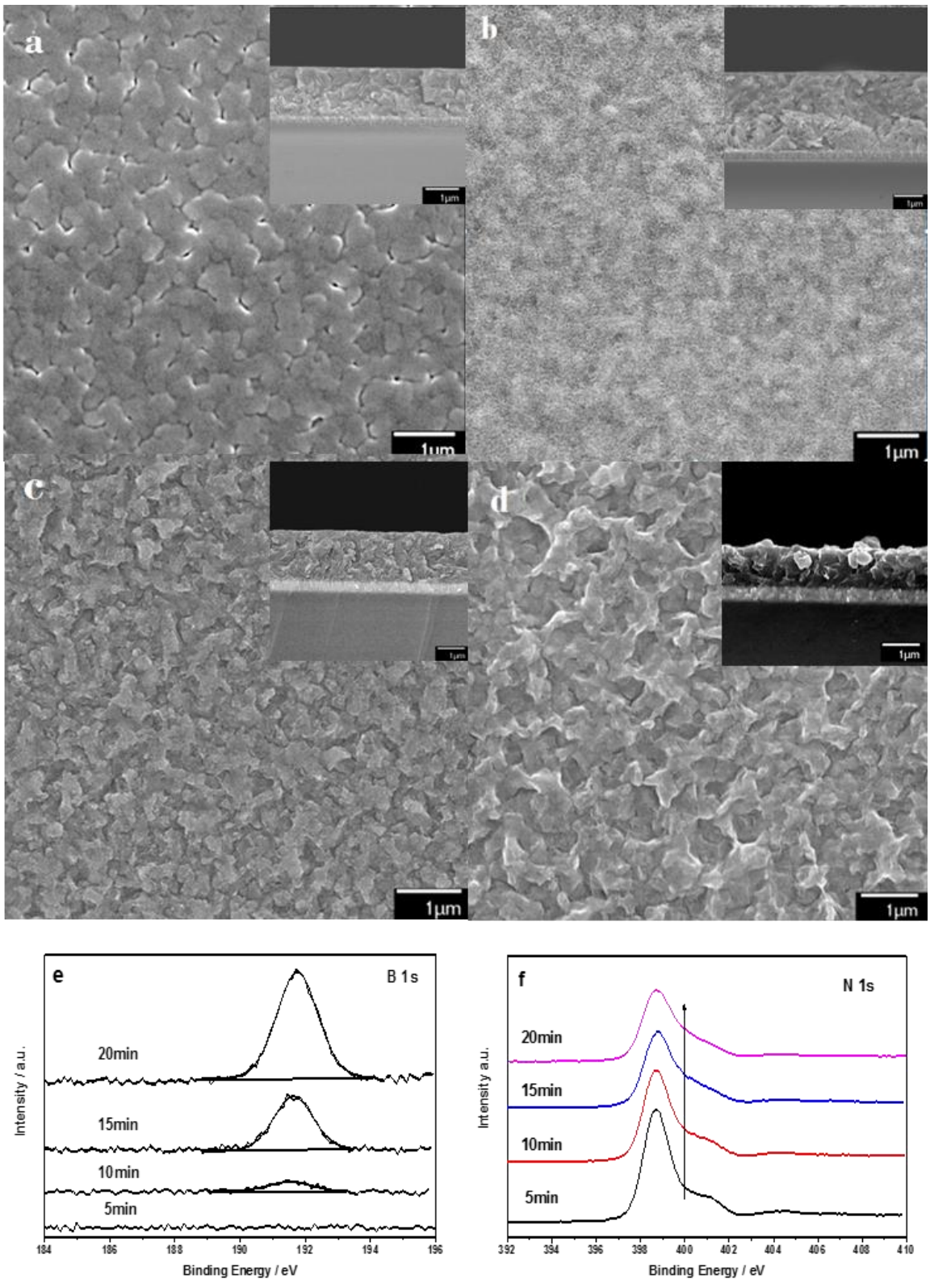

Fig. 58 SEM top and cross-section (inserted) view of s-BCN calcined for a) 5min, b) 10min, c) 15min, d) 20min and their e) B1s and f) N1s XPS spectrum

The optical properties of compact-g-C_3N_4 and s-BCN films, as an important physical property for photocatalysis, are investigated by UV-vis spectroscopy, shown in **Fig. 59**a with UV-Vis spectra of compact-g-C_3N_4 and B-doped CN powder in **Fig. 59**b as references. Pure carbon nitride exhibits a bandgap of *ca.* 2.72 eV, similar to previous reports.[207-208] S-BCN shows a red-shift of the spectrum with a slightly narrower bandgap of *ca.* 2.65 eV. The narrowed bandgap of s-BCN extends its visible light absorption, which is somehow beneficial to the photocatalytic reaction. UV-Vis spectra on g-C_3N_4 powder and B-doped CN powder are shown in **Fig. 59**b. It is found that B-doped CN powder has a bandgap of 2.61 eV, smaller than that of g-C_3N_4 powder (2.72 eV). It is noticed that the bandgap measured for s-BCN film (2.65 eV) (composed of 100 nm B-doped CN layer and 900 nm G-CN layer) is larger than that of bulk B-doped CN (2.61 eV) while smaller than the g-C_3N_4 powder (2.72 eV). It may indicate that the B-doped nanolayer partially contributed to the light absorption of the s-BCN film.

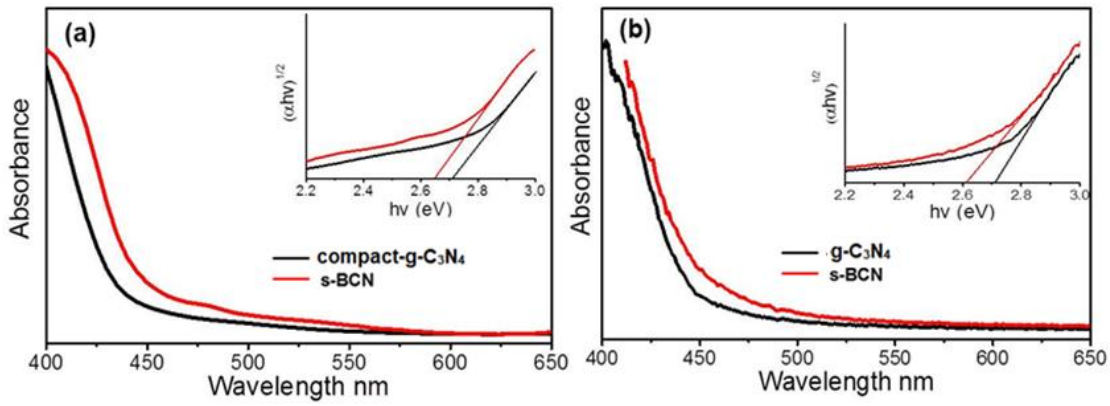

Fig. 59 UV-Vis spectrum and tauc plot (inset) of a) compact-g-C_3N_4 and s-BCN film; b) g-C_3N_4 and B-CN powder

N1s and C 1s XPS spectra are then observed to further understand the doping position of B in the films. Typical N1s spectra of s-BCN are fitted to four components in **Fig. 60**a. The main peak locates at 398.8 eV is usually attributed to C-N-C bonds[70]. Compared to compact-g-C_3N_4, an additional peak at 399.6 eV is believed to be associated with boron substitution (**Fig. 60**a). Apart from that, the other two peaks at higher energy account for C-$[N]_3$ (400.0 eV), C-NH_x bonds (401.1 eV) respectively, consistent with pure carbon nitride.[70] In **Fig. 60**b, C1s peak at 288.2 eV, corresponds to the binding energy of C-N-C bonds. The small peak at 286.4 eV is C-O bonds and peak centered at 284.8 eV is C-C carbon impurity. The unchanged carbon chemical environment (**Fig. 60**) further proves boron atoms substitute carbon, not nitrogen.

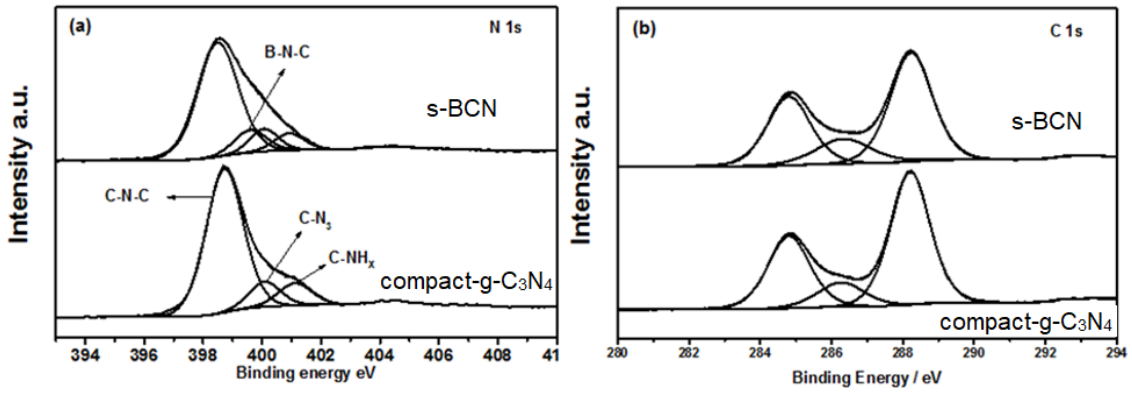

Fig. 60 a) N1s XPS spectra and b) C1s XPS spectra of compact-g-C_3N_4 and s-BCN

Doped with boron, the FT-IR spectrum of s-BCN reveals a typical molecular structure of graphite carbon nitride (**Fig. 61**a). The intense band at 806 cm^{-1} represents the out-of-plane bending vibration characteristic of heptazine rings or BN stretching vibration[209]. The bands at 1311 and 1226 cm^{-1} correspond to stretching vibration of connected units of C–N(–C)–C or C–NH–C. The intense bands at 1633, 1558, 1456 and 1406 cm^{-1} can be assigned to typical stretching

vibration modes of heptazine-derived repeating units. Raman spectroscopy allows the fine structure of compact-g-C_3N_4 and s-BCN to be examined in detail (**Fig. 61**b). From 1200-1700 cm^{-1} a series of peaks are attributed to C-N stretching vibrations, specifically “G and “D” band profiles of structurally disordered graphitic carbon and other carbon/nitrogen layered compounds[210]. The peak at 980 cm^{-1} can be assigned to the symmetric N-breathing mode of heptazine, whilst the peak at 690 cm^{-1} corresponds to the in-plane bending vibrations of the tri/heptazine C-N-C linkages[211]. Both FTIR and Raman spectrum prove that compact-g-C_3N_4 and s-BCN had a typical local structure of g-C_3N_4.

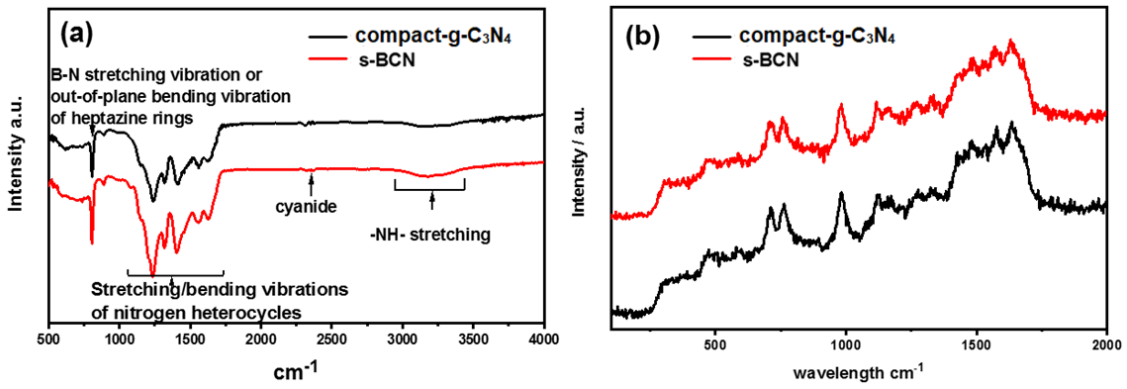

Fig. 61 a) FTIR and b) Raman spectrum of compact-g-C_3N_4 and s-BCN

Solid-state ^{13}C CP-MAS NMR spectra (**Fig. 62**) shows two distinct peaks at δ = 156.0 ppm and δ = 164.1ppm, respectively. The first peak is attributed to the sp^3 hybridized C centered in the melem unit. The second peak can be assigned to the surround C atoms in $CN_2(NH_2)$ group[212]. All these characterizations confirm the successful synthesise of a pure carbon nitride film and surface nanojunction s-BCN film.

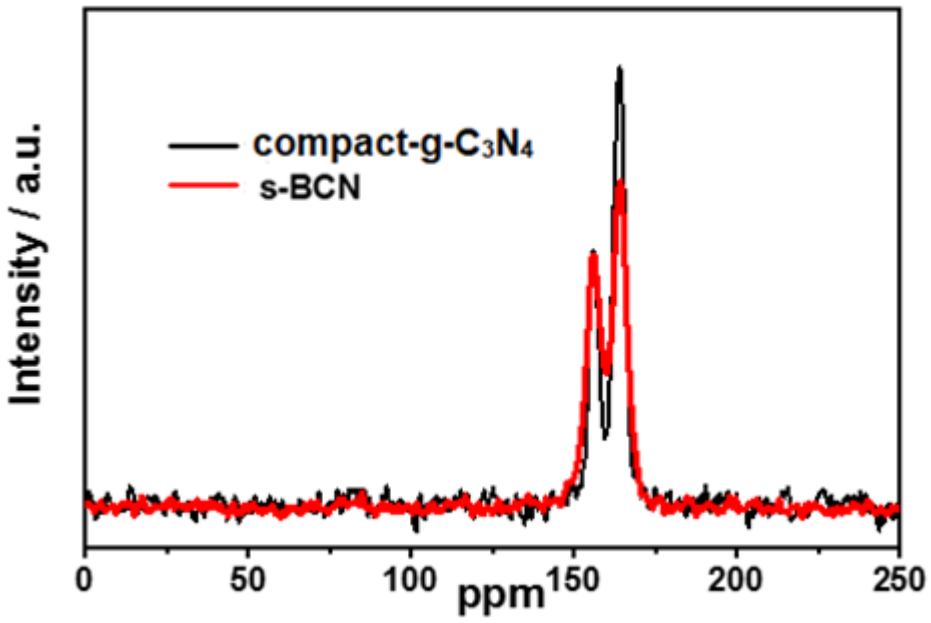

Fig. 62 Solid-state ^{13}C CP-MAS spectra of compact-g-C_3N_4 and s-BCN

The photocatalytic water splitting by these samples in a PEC cell was then carried out and the anodic photocurrent curves of compact-g-C_3N_4 and s-BCN are displayed in **Fig. 63**a. Compact-g-C_3N_4 and s-BCN samples show negligible dark current from 0.4 V to 1.23 V vs RHE. G-CN shows a low photocurrent of 10.6 μA/cm^{-2} at 1.23 V vs RHE, similar to previous reports.[117, 120, 190] The performance of the compact-g-C_3N_4 sample is significantly enhanced by adding a nanolayer of boron doped CN. To find the optimum boron content, different samples have been tested (If a wt% boric acid precursor and (1-a) wt% DCDA precursor were used, the prepared sample was denoted s-BCN (a%)) (**Fig. 63**a). The s-BCN (4%) nanojunction film exhibits the highest photocurrent of 103.2 μA/cm^{-2} at 1.23 V vs RHE, which is the highest for g-CN based polymer photoanode in the absence of any chemical scavenger, to the best of our knowledge. This specific film has a 100 nm surface doped CN layer onto 900 nm G-CN. The real boron concentration on the doped CN layer is determined to

be 0.6% by XPS. Further increase of boron concentration results in a decrease in photocurrent. To investigate the photocatalytic response of electrodes at different wavelengths, incident light-to-electron conversion efficiency (IPCE) measurements of both s-BCN (4%) and compact-g-C_3N_4 films are acquired at 1.23 V_{RHE} (**Fig. 63**b). The IPCE of compact-g-C_3N_4 has been measured to be around 1% at 400 nm, while remarkably increasing to nearly 10% for s-BCN (4%) at the same wavelength.

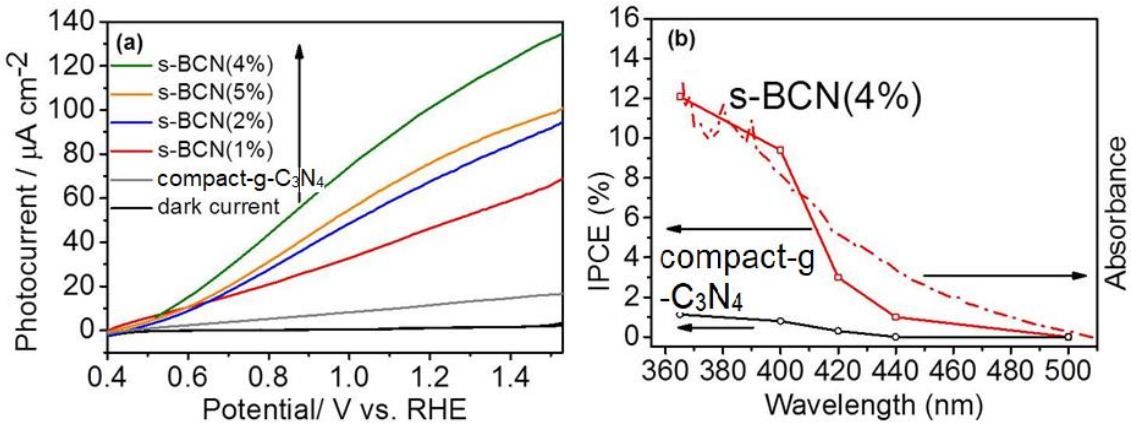

Fig. 63 a) Photocurrent-potential curves for s-BCN (0-5%) illuminated from the back-side; electrolyte: 0.1M Na_2SO_4 solutions (pH=6.5), one sun irradiation provided. b) IPCE plot of compact-g-C_3N_4 and s-BCN (4%) at 1.23V vs RHE

More electrochemical analysis of s-BCN and compact-g-C_3N_4 samples have been carried out, including Mott-Schottky (MS) plots and electrochemical impedance spectroscopy (EIS) Nyquist plots, to investigate the reason for dramatically enhanced IPCE. Typical MS plots in the dark condition disclose the n-type characteristics of s-BCN and compact-g-C_3N_4 due to the positive slope of the linear plots (**Fig. 64**a).[213] The carrier density of s-BCN and compact-g-C_3N_4 derived from Mott-Schottky plots are of the same order of magnitude. The similar carrier density suggests that nanoscale surface doping, as expected,

does not affect the carrier concentration in bulk. The flat-band potential is also derived from the extrapolation of MS plots at different frequencies (**Fig. 65**). For both compact-g-C_3N_4 and s-BCN, the flat-band potentials are determined to be *ca.* -1.3 V vs Ag/AgCl (pH=6.5), consistent with previously reported pristine carbon nitride.[35, 213-214] However, the s-BCN has a smaller bandgap than compact-g-C_3N_4 which forms a heterojunction on the surface. Apparently, boron doping slightly shifts the band structure of carbon nitride and the driving force between carbon nitride and boron-doped nanolayer enables the efficient charge separation between the bulk and the surface for photooxidation reaction.

EIS Nyquist plots (**Fig. 64**b) were used to observe the charge transfer rate. A significantly decreased diameter for semicircle of s-BCN is observed. The electron-transfer conductivity calculated with an equivalent circuit shows a three-time increase for the s-BCN sample compared with compact-g-C_3N_4, which is further confirmed by the measurement of the photocurrent (inset of **Fig. 64**b). A remarkable improvement in photocurrent of s-BCN over compact-g-C_3N_4 is likely due to a more efficient charge transfer for s-BCN samples

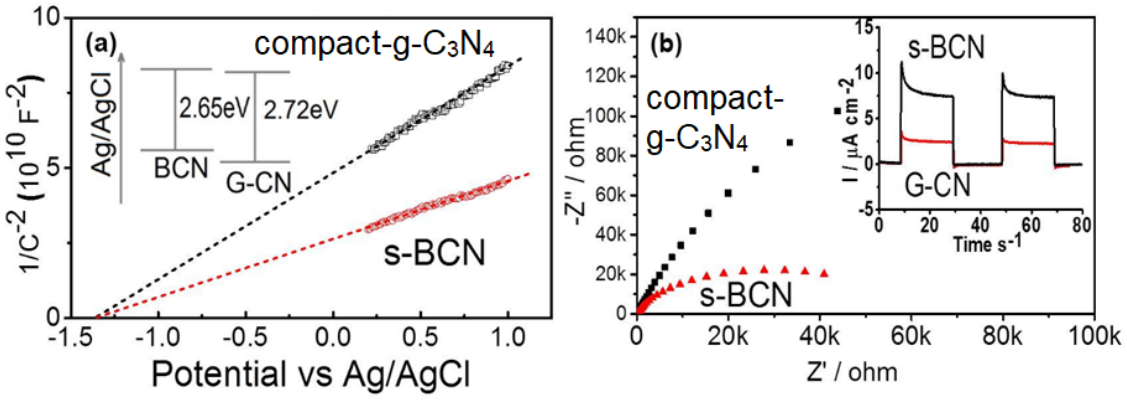

Fig. 64 a) Mott–Schottky plots of G-CN and s-BCN at 1 kHz frequency and the plots at other frequencies shown in Fig. 65) Nyquist plots of compact-g-C_3N_4

and s-BCN obtained by applying a sine wave with an amplitude of 5.0 mV over the frequency range from 10 kHz to 0.1 Hz with the inset showing the periodic on/off photocurrent response of compact-g-C_3N_4 and s-BCN electrodes in 0.1 M Na_2SO_4 with 0 V bias versus Ag/AgCl.

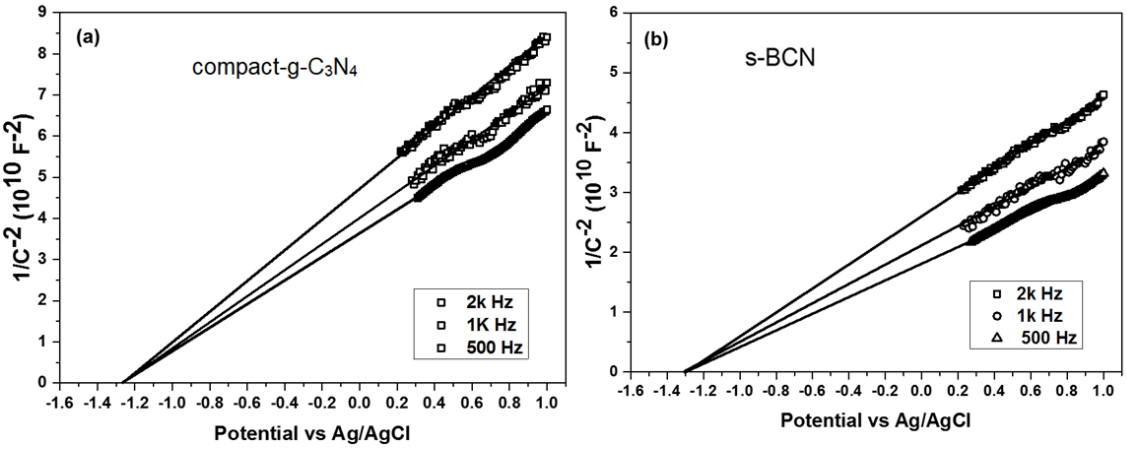

Fig. 65 Mott-Schottky plots of a) compact-g-C_3N_4 and b) s-BCN at 2k, 1k and 0.5 k Hz frequencies.

To further investigate the kinetics of charges in s-BCN, intensity-modulated photocurrent spectroscopy (IMPS) has been employed. Typical IMPS responses of compact-g-C_3N_4 and s-BCN photoanode are provided in a complex plane (**Fig. 66**). The high-frequency semicircle (lower semicircle) indicates charge transport and relaxation in photoanode, whose intercept with x-axis equals to the hole current without recombination, while the low-frequency semicircle (upper semicircle) corresponds to the competition between interfacial charge transfer and surface recombination.[215] Compared with compact-g-C_3N_4, the larger hole current (no recombination) of s-BCN implies more efficient hole capture by surface, which in sequence are either transferred to electrolyte or recombine with electrons.[161]

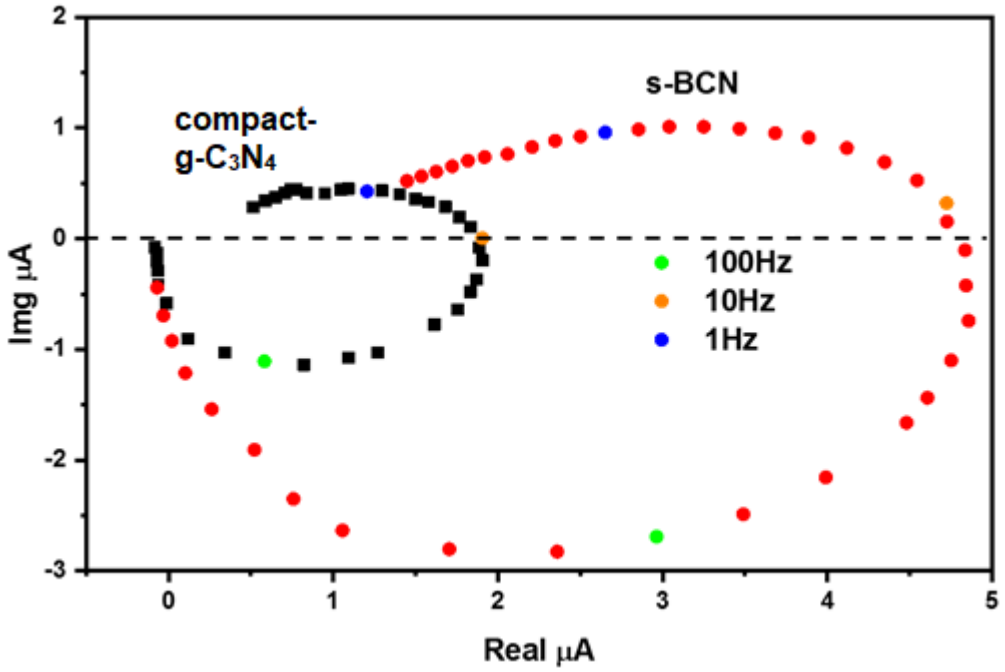

Fig. 66 Typical IMPS response of compact-g-C_3N_4 (black) and s-BCN (red) films at 0.1V vs Ag/AgCl, 0.1M Na_2SO_4, pH=6.5

Kinetics of charges can be represented by the first-order rate constant of surface recombination (K_r) and interface charge transfer (K_t) derived from IMPS plot data (**Fig. 67**) and plotted in **Fig. 68**. Larger K_r describes a faster charge recombination on the electrode surface. In both samples, K_r decreases strongly with potential as expected for an ideal semiconductor/electrolyte interface, because large potential increases the band bending so that charge recombination both in bulk and at the surface is suppressed.[161] It is noted that at a low potential, K_r in s-BCN is larger than that in compact-g-C_3N_4. It can be explained that boron doping can introduce defects on the surface that becomes recombination centers for charge recombination. Consistent with this, too high a concentration of boron doping promotes surface recombination and results in poorer PEC performance (**Fig. 63**a), so the bulk doped samples always yields a low photocurrent as reported.[216] At high potential, the surface recombination of

both samples is suppressed as most electrons are driven to the counter electrode by bias. K_t is used to describe the transfer of charges between electrode and electrolyte, i.e. reaction between holes and water in the study. As shown in **Fig. 68**, K_t of s-BCN samples is apparently 10 fold larger than that of compact-g-C_3N_4, e.g. 7 s^{-1} for s-BCN samples and 0.7 s^{-1} for compact-g-C_3N_4 at 0.2 V vs Ag/AgCl, indicating nearly 10 times faster reaction rate of photoholes with water as a result of the nanojunction architecture. More importantly, the ratios of K_t/K_r of G-CN and s-BCN which are plot in **Fig. 68** (inset) indicate the efficiency of the photoanode. At potential larger than 0.2 V vs. Ag/AgCl, the value of K_t/K_r of s-BCN becomes sharply increase, much larger than that of compact-g-C_3N_4, e.g. 3 times larger at 0.4 V vs. Ag/AgCl, indicating much more charges to be used for water oxidation by the nanojunction photoanode.

Based on the band alignment in the inset of **Fig. 64**a, boron doping shifts the valence band of CN upward. The driven force between valence band of compact-g-C_3N_4 layer and upshifted valence band of B-doped CN layer allows holes after excitation to transfer from compact-g-C_3N_4 to B-doped CN layer, while electrons transfer to the compact-g-C_3N_4 layer even in the presence of very weak bias. A 10 time higher charge transfer rate on the s-BCN top layer further helps the fast water oxidation reaction. Therefore, the final photon conversion efficiency in the visible region (at 400nm) enhances by a factor of 10 due to the nanojunction.

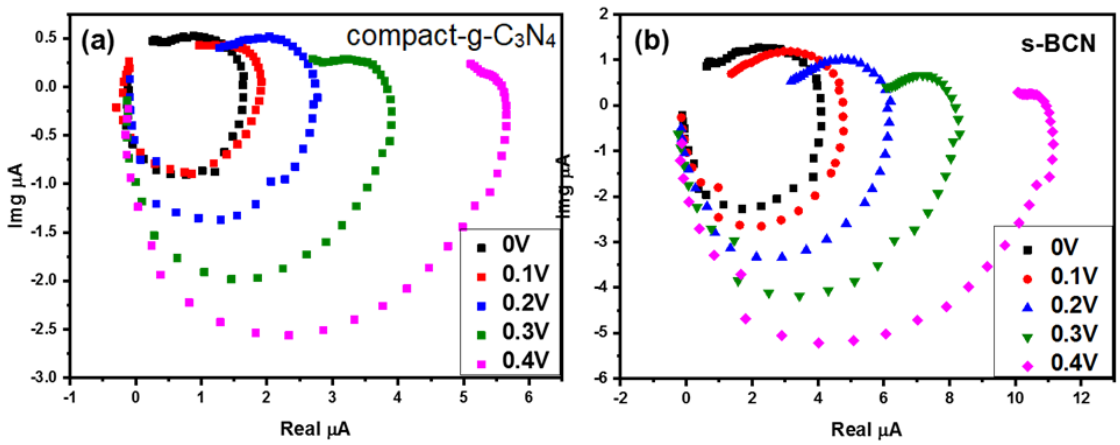

Fig. 67 IMPS plots of a) compact-g-C_3N_4 and b) s-BCN at 0 V - 0.4 V vs Ag/AgCl

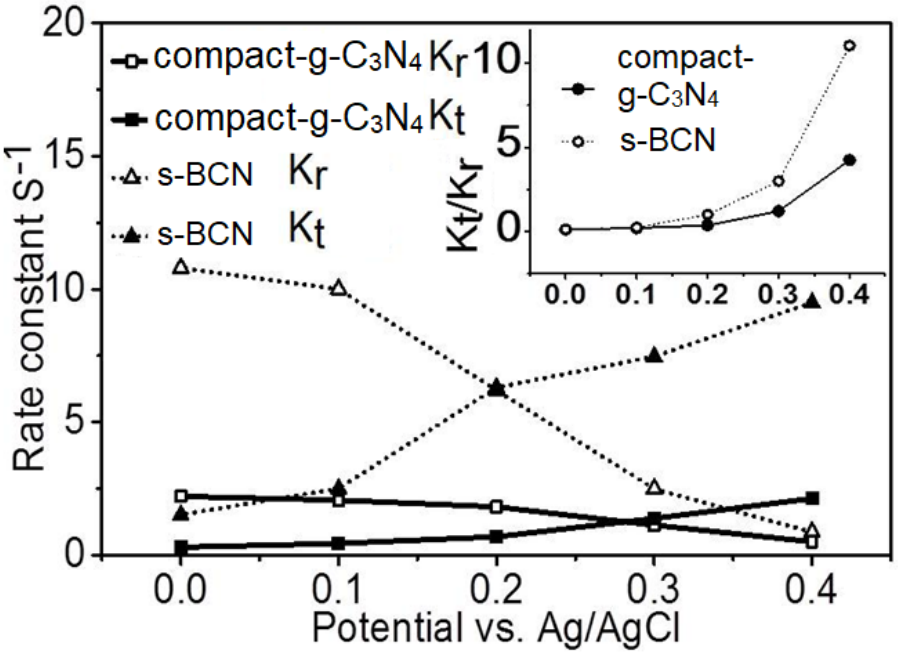

Fig. 68 Potential dependence of the rate constant K_t and K_r for s-BCN and compact-g-C_3N_4 (g-C_3N_4) samples, Illumination: 365nm UV light

To further prove the sufficient charge separation on the s-BCN surface. I added H_2O_2 as efficient hole scavenger in the electrolyte, aiming to remove charge recombination on the surface. In **Fig. 69**, at low potential (e.g. 0 V vs Ag/AgCl), H_2O_2 could significantly enhance the photocurrent density of s-BCN

due to a large K_r value of 11 s^{-1} at that potential. However, at high potential (e.g. V > 0.4 V vs. Ag/AgCl), adding H_2O_2 cannot further improve the photocurrent density. It indicates that the charge separation at the s-BCN surface is sufficient, agreeing with a high ratio of K_t/K_r displayed in **Fig. 68** (e.g. K_t/K_r > 10 at 0.4 V vs Ag/AgCl). In contrast, H_2O_2 significantly improves photocurrent of compact-g-C_3N_4 film, indicating that charge separation on the compact-g-C_3N_4 surface is less efficient,

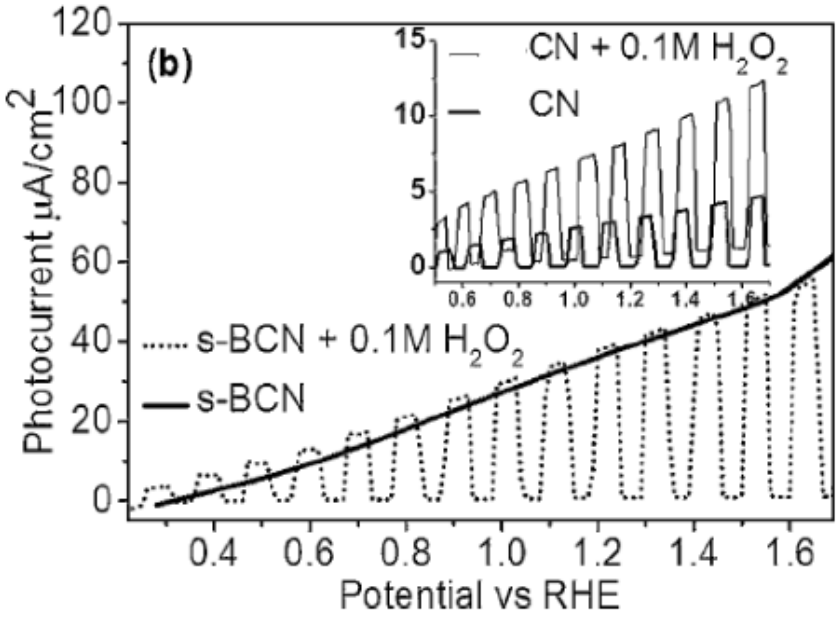

Fig. 69 Photocurrent of s–BCN and CN (compact-g-C_3N_4) with and without the addition of 0.1M H_2O_2

5.4 Conclusion

To conclude, this chapter presents a novel strategy for the production of nanojunciton on carbon nitride film, which acts as a potential photoanode for water oxidation. The resulting nanojunciton film shows a high photocurrent density of 103.2 μA/cm^2 at 1.23 V vs RHE under one sun condition (weaker light

intensities than that used in chapter 4) and a high IPCE of 10% at 400 nm, which is 10 times higher than that of pristine carbon nitride. Data from XPS, UV-vis, and PEC analysis show that the surface nanolayer doping can significantly improve the solar to fuel conversion efficiency but without dramatically changing the bandgap and bulk properties. Such enhancement is mainly due to the efficient charge separation and fast charge transfer in the nanojunction as evidenced by EIS, MS and IMPS spectroscopies. Furthermore, the H_2O_2 addition proves that the efficient charge separation can be achieved by the nanojunciton itself. I believe that this surface nanojunction strategy can be extended to other semiconductors to efficiently improve their applications in the fields of solar fuel conversion and environmental purification.

6 Insight on shallow trap states introduced photocathodic performance in n-type polymer photocatalysts

With the success of preparing efficient g-C_3N_4 photoanode, the potential of g-C_3N_4 as a promising photocathode is explored. Strategies of transforming an n-type g-C_3N_4 semiconductor from a photoanode to a photocathode and fundamental understandings thus will be investigated in this chapter.

6.1 Introduction

Great successes in overall water cleavage and especially hydrogen evolution (up to 20000 μmol $h^{-1}g^{-1}$) have been achieved using a nominal g-C_3N_4 (in fact it is CN_xH_y as many protons are incorporated in the commonly prepared carbon nitrides. It is denoted as g-C_3N_4 in this work for consistence with all papers published in this field)[57] in suspension systems. Such H_2 evolution rate is much higher than the majority of inorganic photocatalysts,[217] indicating this nominal g-C_3N_4 would be an excellent candidate as a photocathode.[36, 70] However, only a few works reported on the single phase g-C_3N_4 as a photocathode while with a low photocurrent density.[108, 117, 137, 218-219] The reason behind this inconsistency between its extremely excellent H_2 evolution ability and very poor photocathodic performance is not well studied while of scientific significance for its application and efficiency improvement in photoelectrochemical water splitting taking into account its potential to be an excellent photocathode for solar H_2 production. To

address this challenge, fundamental factors that affect the photocathodic behavior of g-C_3N_4 have to be understood comprehensively.

The intrinsic property of the g-C_3N_4 film as an n-type semiconductor limits hydrogen generation at the electrode/electrolyte interface, as n-type semiconductors exhibit upward band bending which results in accumulation of holes on the surface. This promotes anodic behavior, resulting in many literature reports of photoanodes based on pristine g-C_3N_4.[154, 176, 220] In order to realize its potential to be an efficient photocathode, diverse strategies of preparing g-C_3N_4-based photocathodes were developed including heteroatom doping,[221] biopolymer–activation[222] and heterojunction construction[137] while the photocurrent of the prepared photocathode is still very moderate, nearly 10 times smaller than that as a photoanode.[122] The function of trap states has been shown to be essential to pristine g-C_3N_4's performance in a suspension system, where long-lived trapped electrons enabled H_2 evolution even in the dark condition[223] and shallow trapped electrons significantly improved the H_2 generation activity.[152] Trap states in g-C_3N_4 are commonly a result of structural defects, and can be caused by structural nonideality, including C/N vacancies and/or -OH/–NH_x terminal groups. Different defects give rise to different types of trap states, which in turn result in different PEC behavior.

To understand the impact of trap states on the photoelectrode characteristics of g-C_3N_4 in depth and more importantly to discover an efficient strategy for g-C_3N_4 to be an excellent photocathode herein I tried to introduce N defects along with C-OH terminal groups to generate shallow trap states in the g-C_3N_4 framework through ultrasonication. Compared to a reference g-C_3N_4 film (compact-g-C_3N_4) that behaves as a photoanode, defect-introduced g-C_3N_4

exhibits clear cathodic PEC behavior. To provide further evidence for the necessity of trap states associated with C-OH terminal groups and N defects for cathodic performance, reference g-C_3N_4 film (compact-g-C_3N_4) was protonated using H_2O_2 treatment, and shows a clear transformation from a photoanode to a photocathode. These findings provide a novel strategy for an efficient polymer photocathode for solar driven H_2 fuel synthesis.

6.2 Experimental

Sample preparation

g-C_3N_4 powder was synthesised by calcinating 2g Dicyandiamide (Alfa Aesar, 99%) at 600 °C for 4h with a ramping of 5°C/min in air atmosphere. 10 mg as-prepared g-C_3N_4 particles were sonicated in 30ml distilled water for 1h, 2h and 5h. 1ml as-obtained suspension was drop-casted on a 2 cm * 2cm FTO glass and dried at 70 °C for 1h. The fabricated films made from 1h, 2h and 5h sonicated g-C3N4 suspension were labelled as def-g-C_3N_4-1, def-g-C_3N_4-2 and def-g-C_3N_4-5, respectively.

Reference g-C_3N_4 film (compact-g-C_3N_4) was fabricated as I reported before.[176, 224] To be brief, 50 mg Dicyandiamide (Alfa Aesar, 99%) was dissolved with DI water in a Φ35 mm petri dish. After drying at 70 °C for 1h, Dicyandiamide precursor were recrystallized and adhered to the internal surface of the petri dish. A piece of 2 cm × 2 cm FTO glass used as the substrate was placed on a slightly concave crucible lid and covered by the petri dish. The sample was calcined in a 600 °C preheated Muffle furnace (Carbolite, CWF 1300) for 23 min and quenched to the room temperature in air. The as prepared film was labelled as ref-g-C_3N_4.

Characterizations

XRD patterns were collected by a D8 Bruker Diffractometer. The UV-Vis absorption spectra were collected using a Shimadzu UV-Vis 2550 spectrophotometer fitted with an integrating sphere using $BaSO_4$ as the reference material. XPS measurements were done on a Thermoscientific XPS K-alpha surface analysis machine using an Al source. Analysis was performed on the Casa XPS software. SEM images were taken by a JEOL JSM-7401F Scanning Electron Microscope.

The photoelectrochemical properties were investigated in a conventional three-electrode cell using an electrochemical analyser (IVIUM Technologies). The as-prepared film, a Pt net and an Ag/AgCl electrode were used as the working, counter and reference electrodes, respectively. The photocurrent of samples was measured in 0.1 M Na_2SO_4 aqueous solution purged with argon under 150 W Xenon lamp (Newport). Samples were illuminated from the SE side (FTO substrate/semiconductor interface).

In the open circuit voltage decay (OCVD) measurement, electrodes were placed in dark condition until the voltage became stable. 150 W Xenon lamp (Newport) was illuminated to the EE side of the electrode. After the stable photovoltage was observed, light source was turned off to obtain the photovoltage decay. The electrolyte–electrode (EE) side of each sample was exposed to intense irradiation to generate a photovoltage. The Mott–Schottky curves were measured at a certain DC potential range with an AC amplitude of 5 mV and a frequency of 1000 Hz under 0% - 100% illumination. The charge density could be determined from the slope of the MS plot using the equation 15-16, where C is the differential capacitance; ε is the dielectric constant of the semiconductor, ε_0 is the permittivity of free space, A is the area, e is the

elementary charge, N_D is the density of charge carriers, V is the applied potential, V_{fb} is the flat-band potential, k_B is the Boltzmann constant, and T is the absolute temperature.

$$\frac{1}{C^2} = \frac{2}{\varepsilon\varepsilon_0 A^2 e N_D}\left(V - V_{fb} - \frac{k_B T}{e}\right) \quad \text{(Equation 15)}$$

$$slope = \frac{2}{\varepsilon\varepsilon_0 A^2 e N_D} \quad \text{(Equation 16)}$$

6.3 Results and discussion

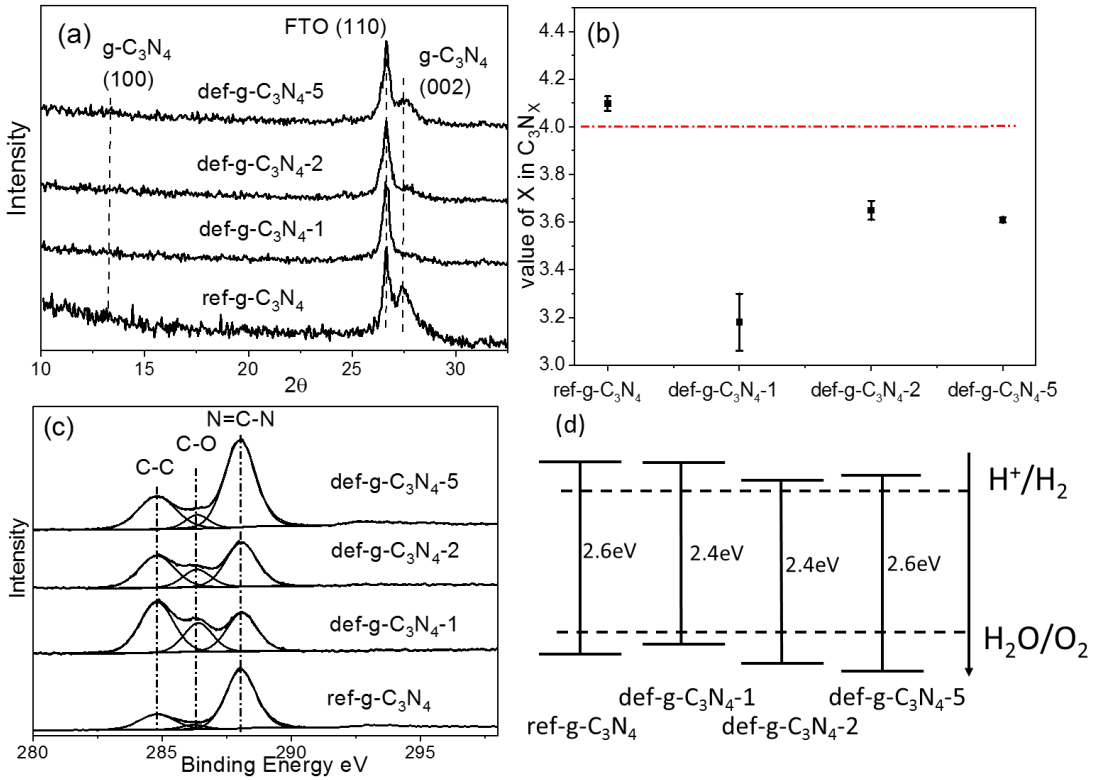

Fig. 70 (a) XRD patterns of ref-g-C_3N_4 (compact-g-C_3N_4), def-g-C_3N_4-1, def-g-C_3N_4-2 and def-g-C_3N_4-5 prepared on FTO substrate, and shows an extra peak from SnO_2 (110) plane; (b) Carbon to nitrogen ratio calculated from XPS survey spectrum of all samples, the red straight line indicates the carbon to nitrogen ratio in an ideal g-C_3N_4; (c) analysis of C1s XPS peak of all samples; (d) band

structure of all samples determined by their UV-Vis absorption and XPS valence-band spectra in **Fig. 72**.

In order to investigate the functions of trap states in g-C_3N_4, four different g-C_3N_4 samples were prepared, consisting of one reference film (ref-g-C_3N_4) with low defect density and three defect-introduced films. The defect-introduced films were prepared by sonicating g-C_3N_4 powder for 1h, 2h or 5h in water, then drop-casted onto FTO glass substrate, respectively labelled as def-g-C_3N_4-1, def-g-C_3N_4-2 and def-g-C_3N_4-5. More details on sample preparation can be found in Supporting Information (SI). The XRD pattern of all four samples are shown in **Fig. 70**a. All samples show a peak at 27.5°, which represents the interlayer arrangement in g-C_3N_4 structure, indicating that defects introduced by ultrasonication does not affect the interlayer spacing of g-C_3N_4. Obviously, sonicating has a significant impact on the crystallinity of g-C_3N_4 as the peak intensity at 27.5° shows a big variation with sonication duration. The lowest peak intensity of g-C_3N_4-1 indicates that 1h sonication has introduced severe structure disorder, while longer sonicating duration (2h and 5h) could partially restore the crystallinity. The other board peak at 13.2° is ascribed to repeating heptazine structure which is absent in def-g-C_3N_4-1 and def-g-C_3N_4-2 sample due to their poor crystallinity.[225] The sharp peak at 26.7° is attributed to the (110) plane from FTO substrate.[224]

To investigate the impact of sonication on g-C_3N_4 structure in more detail, the carbon to nitrogen ratio on the surface of all samples were calculated from XPS survey spectra, and displayed in **Fig. 70**b. The ref-g-C_3N_4 (compact-g-C_3N_4) has an average N/C ration of 4.1/3, close to the stoichiometric ratio of pristine g-C_3N_4. 1h sonicating results in a decrease of N/C ratio to 3.2/3. The decreased

N/C ratio likely indicates that N vacancies were created by sonication. Further sonication (2h and 5h) increases the N/C ratio to 3.6/3. With longer sonication time, the elementary component of g-C_3N_4 particles becomes more uniform, evident from the reduced error bar calculated by 3 repeated experiments in **Fig. 70**b. Consistent with XRD analysis, more N defects results in lower crystallinity of g-C_3N_4 structure.

Fig. 70c shows C1s XPS spectra which elaborates the chemical surroundings of C element in all four samples. The peak at 288.1 eV corresponds to the binding energy of the C-N bonding, which is dominant in the heptazin structure. The peak centred at 284.8 eV is assigned to adventitious carbon. The faint peak at 286.2 eV corresponds to C-O bonds. In ref-g-C_3N_4 (compact-g-C_3N_4), the concentration of C-O bonds is quite low. Sonicating the g-C_3N_4 powder for 1h significantly increases the amount of C-O. Further sonication (2h and 5h) decreases the amount of C-O, but not to a critical value.

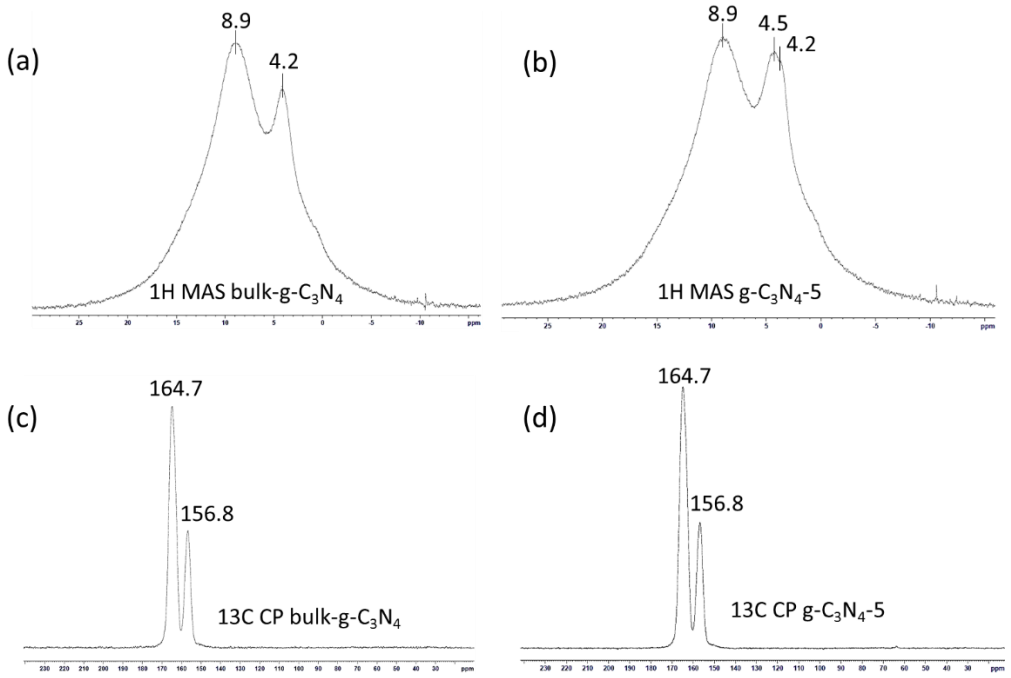

Fig. 71 ^{1}H MAS solid state NMR spectra of (a) g-C_3N_4-5 and (b) bulk-g-C_3N_4; ^{13}C CP MAS solid state NMR spectra of (c) g-C_3N_4-5 and (d) bulk-g-C_3N_4

Agreeing with XPS analysis, ^{1}H Solid state NMR spectra of ref-g-C_3N_4 (compact-g-C_3N_4) and defects introduced def-g-C_3N_4-5 sample show obvious differences. As shown in **Fig. 71**, ^{1}H Solid state NMR spectrum of ref-g-C_3N_4 (compact-g-C_3N_4) contains two main peaks at 8.9 ppm and 4.2 ppm, which can be attributed to the chemical shifts of –NH_x ending group and residual water, respectively.[226] An additional clear peak locating at 4.5 ppm is present in def-g-C_3N_4-5 sample and can be ascribed to the formation C-OH bonds.[226] The appearance of C-OH in def-g-C_3N_4-5 sample NMR spectrum is in agreement with XPS analysis. One can see an interesting correlation between N defects and C-OH groups, more N defects, higher amount of C-OH group. ^{13}C solid state NMR spectra of these two samples show two similar peaks at 156.8 ppm and 164.7 ppm, which has been assigned to C-$[N]_3$ and $CN_2(NH_2)$ groups, respectively.[68]

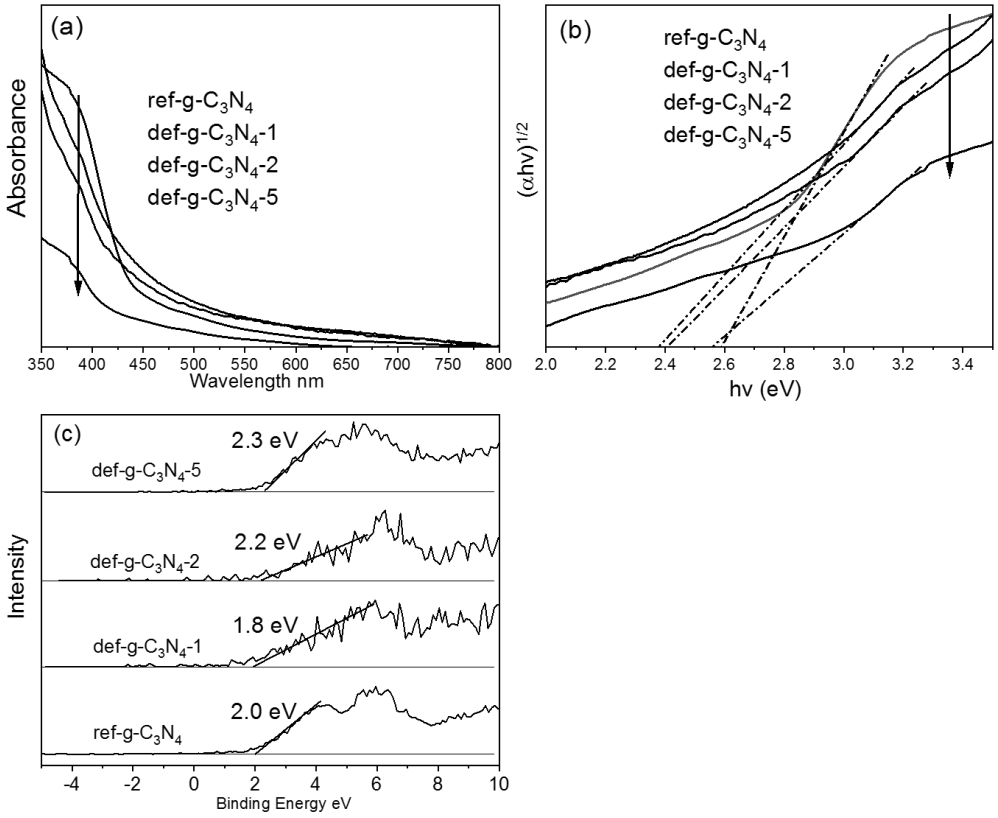

Fig. 72 (a) UV-vis spectra, (b) Tauc plots and (c) XPS valence band spectra of ref-g-C_3N_4 (compact-g-C_3N_4), def-g-C_3N_4-1, def-g-C_3N_4-2 and def-g-C_3N_4-5 films

Significant differences in structure may influence the light absorption of semiconductors. UV-vis spectra illustrating the light absorption of all samples are displayed in **Fig. 72**a. The bandgaps of ref-g-C_3N_4 (compact-g-C_3N_4), def-g-C_3N_4-1, def-g-C_3N_4-2 and def-g-C_3N_4-5 are respectively 2.6 eV, 2.4 eV, 2.4 eV and 2.6 eV, determined from the Tauc plots in **Fig. 72**b. The creation of N defects and introducing of C-O bonds inevitably changed the band structure of g-C_3N_4 samples. From **Fig. 72**c, the linear extrapolations of XPS valence band plots intercept the x-axis at 2.0 eV, 1.8 eV, 2.2 eV and 2.3 eV for ref-g-C_3N_4 (compact-g-C_3N_4), def-g-C_3N_4-1, def-g-C_3N_4-2 and def-g-C_3N_4-5, respectively. Combining this information with bandgap from UV-vis spectra, the relative band structure of all four g-C_3N_4 samples are depicted in **Fig. 70**d.

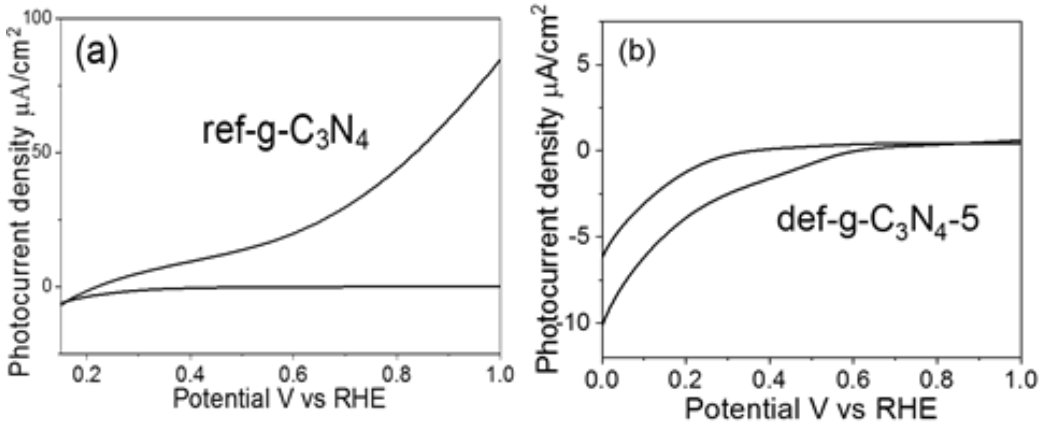

Fig. 73 Photocurrent vs. potential curves of (a) ref-g-C_3N_4 (compact-g-C_3N_4), (b) def-g-C_3N_4-5 with an 150W Xenon lamp illumination in 0.1M Na_2SO_4 electrolyte (pH=6.5).

Photoelectrochemical performance of ref-g-C_3N_4 (compact-g-C_3N_4) and def-g-C_3N_4-5 samples were examined in **Fig. 73**, using a three electrode PEC system. In **Fig. 73**a, the ref-g-C_3N_4 (compact-g-C_3N_4) sample exhibits a clear photoanodic current with a relatively low onset potential at +0.15 V vs RHE. Such a low potential indicates that oxidation reaction could easily happen on the electrode/electrolyte interface, which is expected as holes accumulate on the surface of an n-type semiconductor, resulting in typical photoanode performance of *ca.* 90 μA/cm^2 at 1.0 V vs. RHE. On the other hand, characteristic for a photocathode, negative photocurrent is recorded for def-g-C_3N_4-5, measured as -4 μA/cm^2 at 0 V vs RHE in **Fig. 73**b. Compared with ref-g-C_3N_4 (compact-g-C_3N_4), the def-g-C_3N_4-5 film also experiences a large right shift of the onset potential from +0.15 V vs. RHE to over +0.60 V vs. RHE. The shifted onset potential is probably because introduced the trap states could reduce surface hole accumulation, thus allowing electron accumulation on the surface as evidenced below by the open circuit photovoltage analysis, leading

to photoreduction reaction taking place on the surface of the g-C_3N_4-5 photoelectrode. Together with XPS and NMR analysis discussed above, it is reasonable to speculate that N-defects and -OH terminal groups may play a key role for its photocathode behavior.

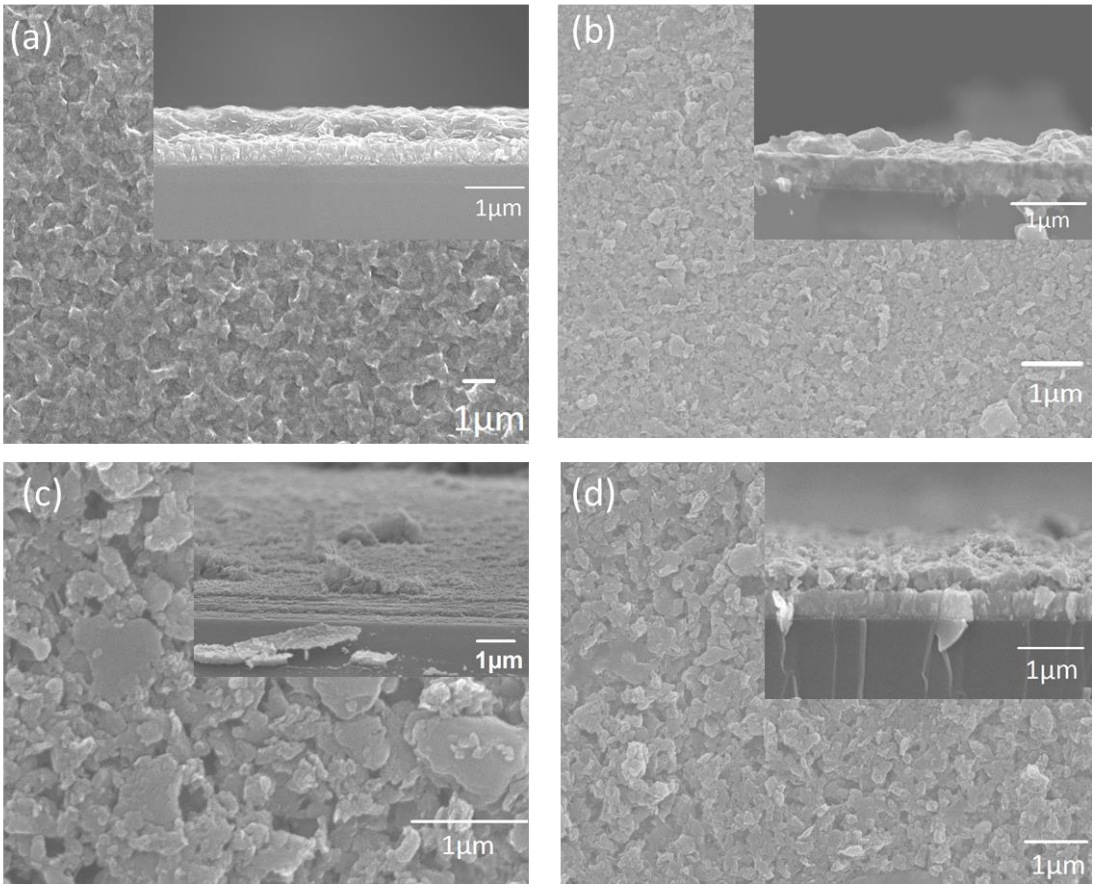

Fig. 74 SEM images of (a) ref-g-C_3N_4 (compact-g-C_3N_4), (b) def-g-C_3N_4-1, (c) def-g-C_3N_4-2 and (d) def-g-C_3N_4-5 films

It is noticing that ref-g-C_3N_4 film (compact-g-C_3N_4) (**Fig. 74**a) has a uniform morphology with a thickness of *ca.* 500 nm and def-g-C_3N_4-5 film (**Fig. 74**d) has relative uniform morphology with thickness approaching 500 nm as well. As such, the morphology and film thickness are not factors that influence the cathodic behaviour of the def-g-C_3N_4-5 photoelectrode. For photocathodic behaviour to be observed, there needs to be a significant proportion of surface

electrons with enough potential for water reduction. Thus it is speculated that the N-defects and C-OH groups introduced in def-g-C_3N_4-5 act as shallow surface traps for electrons. After photoexcitation, electrons trapped in these shallow surface states can reduce water, leading to cathodic behaviour.

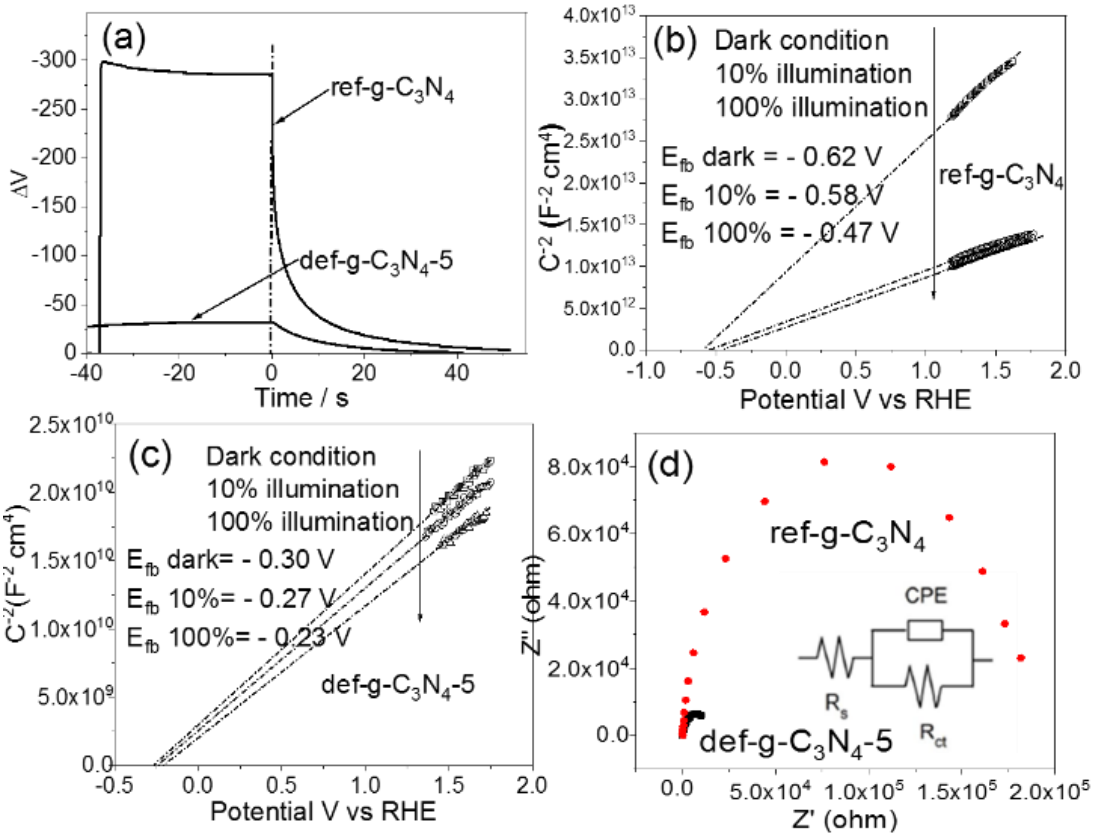

Fig. 75 (a) Open circuit photovoltage decay (OCVD) of ref-g-C_3N_4 (compact-g-C_3N_4) and def-g-C_3N_4-5 electrodes; (b) Mott-schottky plots of ref-g-C_3N_4 (compact-g-C_3N_4) electrode at 1 KHz with 0% - 100% illumination; (c) Mott-schottky plots of def-g-C_3N_4-5 electrode at 1 KHz with 0% - 100% illumination; (d) Impedance plots of ref-g-C_3N_4 (compact-g-C_3N_4) and def-g-C_3N_4-5 electrodes at 0.2 V vs RHE in dark condition; the inset is the equivalent circuit of g-C_3N_4 electrode, where R_s is the system resistance, R_{ct} is the charge transfer resistance, CPE is the constant phase element representing the double layer capacitor.

To investigate the contribution of trap states to the photocathodic behaviour of g-C_3N_4, Open circuit photovoltage Decay (OCVD) was performed on ref-g-C_3N_4 (compact-g-C_3N_4) and g-C_3N_4-5, and charge carrier density was studied with Mott-schottky plots. As shown in **Fig. 75**a, open circuit photovoltage decay (OCVD) plots of both samples show negative photovoltage with illumination, indicating that both films are n-type semiconductors. While the generated photovoltage in ref-g-C_3N_4 (compact-g-C_3N_4) is 10 times larger than in def-g-C_3N_4. This could be due to the surface trap states below the conduction band in def-g-C_3N_4, which mediates the band bending thus reducing the built-in electric field. Then the photoelectrons can accumulate at the trap states, resulting into a small photovoltage determined by the potential difference between the trapped electron states and surface hole states. In one word, the defects introducing into the def-g-C_3N_4-5 photoelectrode mediates its n-type characteristic. Careful observation of the OCVD, one can see that def-g-C_3N_4 has much slower photovoltage decay after the illumination cut-off compared to ref-g-C_3N_4 (compact-g-C_3N_4). The average electron lifetimes of ref-g-C_3N_4 (compact-g-

C_3N_4) and def-g-C_3N_4 are respectively determined to be 0.9 s and 5.5 s, calculated by fitting the photovoltage decay curves as shown in **Fig. 76**. This could be indicative of a significantly higher concentration of surface trap states in def-g-C_3N_4 compared to ref-g-C_3N_4 (compact-g-C_3N_4).

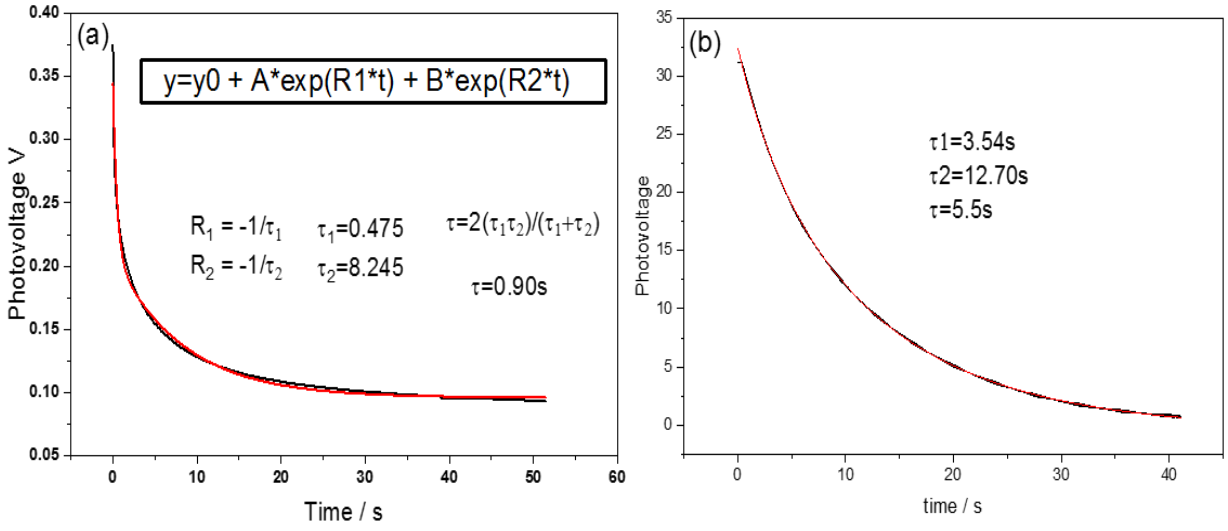

Fig. 76 Determination of average electron lifetime of (a) ref-g-C_3N_4 (compact-g-C_3N_4) and (b) def-g-C_3N_4-5 films

Mott-Schottky (MS) plots of the two samples under different illumination intensities are analysed respectively in **Fig. 75**b and c to investigate the charge carrier density in the ref-g-C_3N_4 (compact-g-C_3N_4) and defect-introduced g-C_3N_4-5. Clear differences in slope is observed under different illumination conditions for ref-g-C_3N_4 (compact-g-C_3N_4), as shown in **Fig. 75**b. Compared to the dark condition, ref-g-C_3N_4 (compact-g-C_3N_4) illuminated with 10% light intensity shows dramatically reduced slopes to a quarter of its original value (dark condition). The higher slope of MS plot usually indicates lower charge carrier density. It could, therefore, be explained that, with illumination, photo-generated electrons are promoted to the conduction band of ref-g-C_3N_4

(compact-g-C_3N_4), boosting the charge carrier density in the film by a factor of 4. Increasing the incoming light density to 100% does not further improve the carrier density level significantly, probably because of fast charge recombination with stronger light intensity[147]. For the def-g-C_3N_4-5 film, as shown in **Fig. 75**c, the slop of MS plots is three order of magnitude lower than the ref-g-C_3N_4 (compact-g-C_3N_4) samples even in the dark condition, suggesting that introducing N defects in g-C_3N_4 structure could significantly improve its charge carrier density and electron conductivity. In contrast, increasing the illumination intensity for def-g-C_3N_4-5 only slightly increases its charge carrier density, as shown in **Fig. 75**c. This is consistent with the significantly lower photovoltage developed by def-g-C_3N_4-5 under illumination compared to ref-g-C_3N_4 (compact-g-C_3N_4) as the relatively weak illumination does not dramatically increase the surface trapped electrons.

In addition, the extrapolations of MS plots in dark condition incepts the x-axis at -0.59 V vs RHE (the flat-band potential, E_{fb} was calculated to be -0.62 V vs RHE) for ref-g-C_3N_4 (compact-g-C_3N_4), while for def-g-C_3N_4, the flat-band potential is -0.30 V vs RHE, which also fits the conduction band edge in **Fig. 70**d. Increasing the light intensity has positively shifted the E_{fb}, which is a characteristic of n-type semiconductor, due to the change in hole density at the interface.[56, 227] Obviously, ref-g-C_3N_4 (compact-g-C_3N_4) has experienced a larger E_F shift of 0.15 V from -0.62 V (in dark) to -0.47 V (100% illumination) than that of def-g-C_3N_4-5 (0.07 V) whose E_{fb} shifted from -0.30 V (in dark) to -0.23 V (100% illumination). The surface states in a typical n-type semiconductor should result in a large positive shift of E_{fb},[228-229] the opposite phenomenon (smaller shift) observed here implies that the n-type characteristic

of def-g-C_3N_4-5 is moderated. This indicates that electrons are more easily transferred to the photoelectrode surface for reduction reaction. Impedance plots of two samples are displayed in **Fig. 75**d and analysed in **Table 7**. Def-g-C_3N_4-5 has a two order of magnitude smaller charge transfer resistance (5.6 * 10^3 $\Omega \cdot cm^2$) than ref-g-C_3N_4 (compact-g-C_3N_4) (1.3 * 10^5 $\Omega \cdot cm^2$), in agreement with the observation in MS analysis.

Table 7. Analysis of impedance plots of ref-g-C_3N_4 (compact-g-C_3N_4) and def-g-C_3N_4-5; R_s is the system resistance, R_{ct} is the charge transfer resistance, CPE is the constant phase element representing the double layer capacitor.

	R_s (Ω cm^2)	R_{ct} / (Ω cm^2)	CPE (S^n Ω^{-1} cm^{-2})	N
ref-g-C_3N_4 (compact-g-C_3N_4)	153	1.3 * 10^5	8.1 * 10^{-7}	0.94
def-g-C_3N_4-5	49	5.6 * 10^3	4.5 * 10^{-5}	0.85

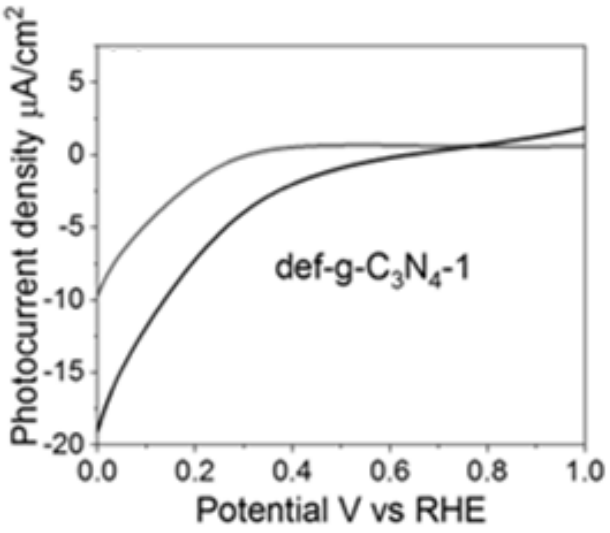

Fig. 77 (a) Photocurrent vs potential curves of def-g-C_3N_4-1.

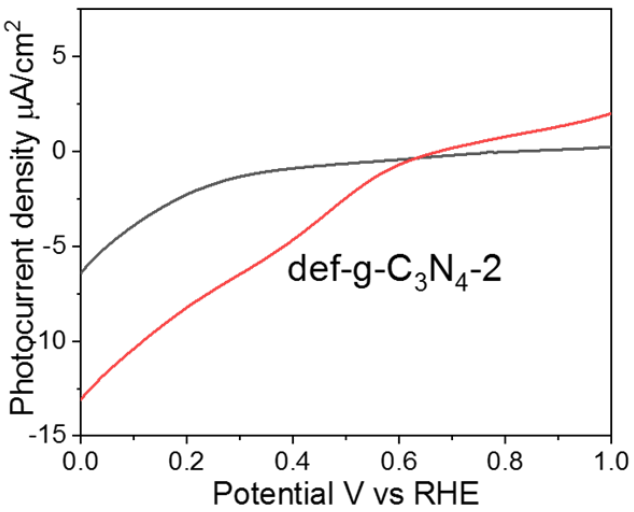

Fig. 78 Photocurrent vs. potential curves of def-g-C_3N_4-2 with a 150W Xenon lamp illumination in 0.1M Na_2SO_4 electrolyte (pH=6.5).

In order to further optimize the cathodic performance of the def-g-C_3N_4 samples, two more samples def-g-C_3N_4-1 and def-g-C_3N_4-2 were characterized by PEC measurement. Interesting, both g-C_3N_4-1 (**Fig. 77**a) and def-g-C_3N_4-2 (**Fig. 78**) exhibits a higher cathodic photocurrent density than g-C_3N_4-5 while the g-C_3N_4-1 is the best. The photocurrent response of def-g-C_3N_4-1 is nearly -10 μA/cm^2 at 0 V vs RHE, which is twice of that observed for g-C_3N_4-5. This is likely because of the much lower nitrogen to carbon ratio and a consequently higher amount of C-O bond in g-C_3N_4-1, as evidenced in **Fig. 71**b and c. Similar to g-C_3N_4-5,

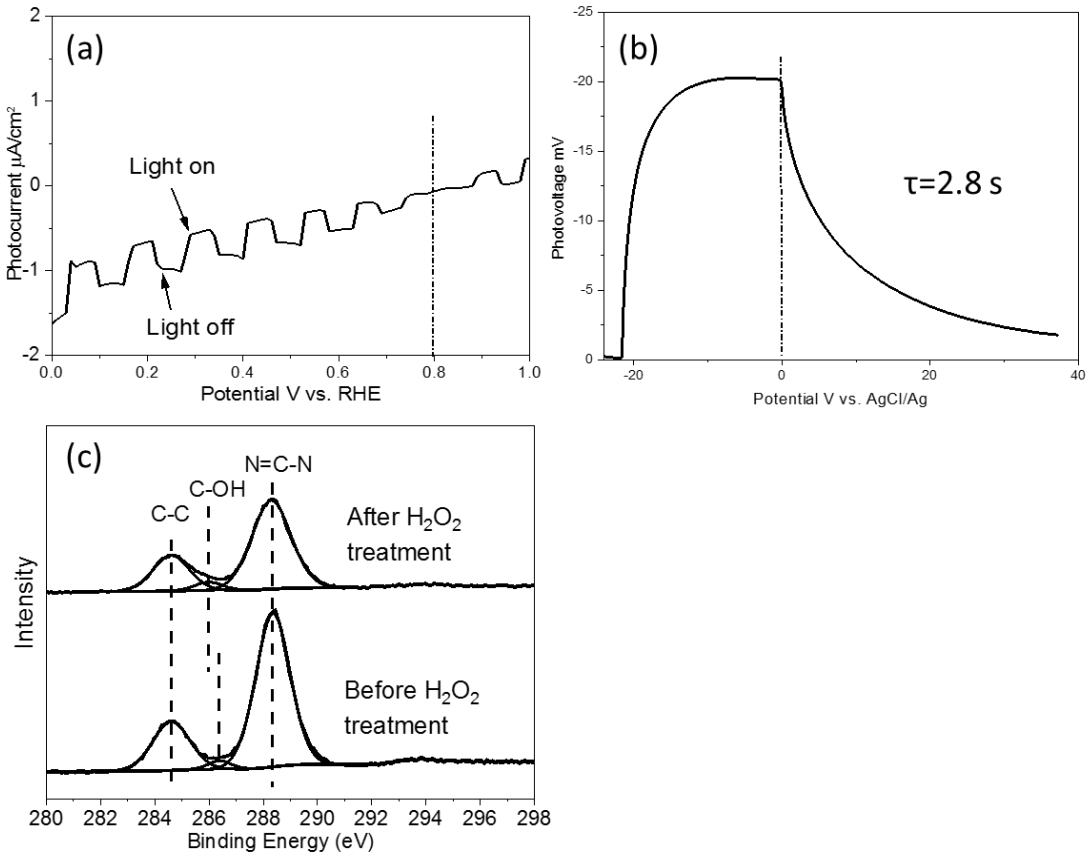

Fig. 79 (a) Photocurrent vs potential plot (b) open circuit photovoltage decay curve and (c) C1s XPS spectra of ref-g-C_3N_4 (compact-g-C_3N_4) before and after H_2O_2 treatment

Table 8. Carbon to nitrogen ratio, and C-O bond to N=C-N bond ratio in ref-g-C_3N_4 (compact-g-C_3N_4) before and after H_2O_2 treatment.

	Before H_2O_2 treatment	After H_2O_2 treatment
C_xN_y	$C_3N_{4.13\pm0.02}$	$C_3N_{3.94\pm0.04}$
C-O bond / N=C-N bond ratio	0.043±0.007	0.066±0.002

As previously mentioned, there are two types of significant trap states in the def-g-C_3N_4- sample: N defects and C-OH groups. To further investigate their roles in a g-C_3N_4 photocathode, the ref-g-C_3N_4 (compact-g-C_3N_4) sample which

has shown good photoanodic performance was protonated by H_2O_2 treatment. After treating with 30% H_2O_2 at 70°C for two weeks, ref-g-C_3N_4 (compact-g-C_3N_4) clearly shows a photocathodic performance, exhibiting a negative photocurrent with an onset potential at +0.8 V vs RHE (**Fig. 79**a). The average charge lifetime derived from OCVD plots of treated ref-g-C_3N_4 (compact-g-C_3N_4) in **Fig. 79**b has increased from 0.9 s to 2.8 s (**Fig. 80**), indicating an increase of surface trap state density after treatment. C1s XPS spectrum in **Fig. 79**c displays a clear left-shift peak of C-O bond afterH_2O_2 treatment, which is due to the appearance of C-OH end group.[230] In **Table 8** the ratio of C-O bond to N=C-N bond increases from 0.043 ± 0.007 to 0.066 ± 0.002 after H_2O_2 protonation, indicating an increase in the amount of C-OH bond as well, with N=C-N bond as a reference. Meanwhile, the carbon to nitrogen ratio has changed from $C_3N_{4.13\pm0.02}$ to $C_3N_{3.94\pm0.04}$, which suggests the introduction of N defects in the structure of g-C_3N_4 after H_2O_2 treatment. This provides further evidence that the introducing of N defects along with C-OH end groups as trap states is responsible for the cathodic behaviour of an n-type g-C_3N_4 semiconductor.

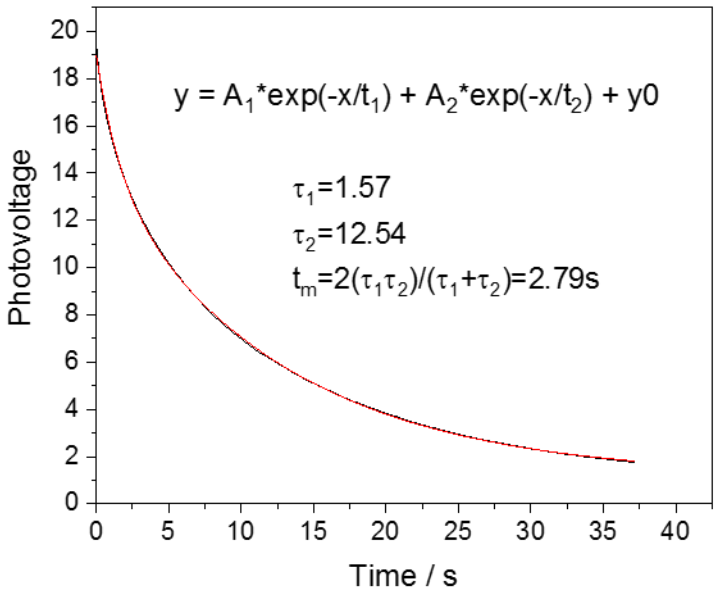

Fig. 80 OCVD curve and OCVD plot analysis of H_2O_2 treated ref-g-C_3N_4 (compact-g-C_3N_4)

6.4 Conclusion

It has been demonstrated that by introducing both N defects and C-OH terminal groups in the g-C_3N_4 structure, this n-type photoanode material (ref-g-C_3N_4) is modified to behave as a photocathode (def-g-C_3N_4). The g-C_3N_4 photoandoe shows ca 90 μA/cm^2 at 1.0 V vs RHE and the optimized def-g-C_3N_4-1 shows a photocathodic performance with *ca.* -10 μA/cm^2 at 0 V vs RHE. This photocathode performance is rationalized by the presence of shallow electron traps associated with the synergy of N-defects and C-OH terminal groups introduced through ultrasonication in water, as indicated by XPS and NMR. The ultrasonicated sample also develops two orders of magnitude higher conductivity and 1000 times longer lived shallow-trapped charges compared with the g-C_3N_4. Furthermore, the average OCVD lifetime observed for def-g-C_3N_4 is 5 times longer than the reference, which can be attributed to the

residual surface-trapped electrons that gradually recombine with photogenerated holes in the bulk material that slowly diffuse to the surface. As such, OCVD and MS plots collectively provide evidence that long-lived electrons in surface trap states associated with N-defects and C-OH terminal groups are key to the photocathodic characteristics of def-g-C_3N_4. This is further evidenced by a clear transformation of a ref-g-C_3N_4 (compact-g-C_3N_4) photoanode to photocathodic performance after H_2O_2 treatment. This new understanding demonstrates that g-C_3N_4 can be both photoanode and photocathode candidates and could aid the rational development and improvement of sustainable organic photoelectrochemical systems for water splitting.

7 Overall conclusions and future work

7.1 Conclusion

Photoelectrochemical (PEC) photosynthesis has been regarded as a promising method to convert inexhaustible solar energy to fuels. Polymer semiconductors have been identified to be promising photocatalysts because they are abundant, environmentally benign, and have easily tuneable band structure. G-C_3N_4 as one of the most promising polymer photocatalysts has realized efficient water splitting in a particle suspension system. However, its PEC application in water splitting was quite limited due to the lack of facile methods for high quality g-C_3N_4 film fabrication, low solar to fuel conversion efficiency and a deep understanding of kinetics in the film. As PEC device is portable, easy to scale up and can produce separated products, synthesising high quality g-C_3N_4 films with high solar to fuel conversion efficiency is of great importance but remains challenging. Therefore, my PhD thesis is designed to address these main obstacles for high performance g-C_3N_4 photoelectrodes and their underlying mechanism.

Firstly, a novel film fabrication method has been developed to prepare dense, uniform and highly crystallized g-C_3N_4 films as a photoanode with controllable thickness. Comparing with g-C_3N_4 films prepared by other methods, the relationship between crystallinity, deep trap states and PEC performance of g-C_3N_4 photoelectrodes was investigated. As such, longer lived charge carriers were present in more poorly crystalline samples, due to more deeply trapped states, which inversely correlated with photoelectrochemical performance. Low deep trap-state density and long electron diffusion length could be achieved in g-C_3N_4

films by manipulating its crystallinity and morphology. The significantly shorten charge lifetime, large transient photovoltage, essentially reduced capacitance, all illustrate the low deep trap state density in a well crystallized, closely packed, high quality g-C_3N_4 thin film. The intrinsic property of the charge diffusion length in these g-C_3N_4 electrodes was determined to be ca. 1000 nm. The reduced deep trap state density and the long electron diffusion length finally contribute to the facilitated charge transfer, efficient charge collection in the film and an excellent photocatalytic performance of 180 μA/cm^2 at a bias of +0.6V vs Ag/AgCl under 150W Xenon lamp illumination (light intensity higher than 100 mW/cm^2), which was 30 times higher than the bulk g-C_3N_4 film prepared by carbon nitride powders widely used in photocatalytic suspension system. This finding intensified the effect of trap states on the photoelectrochemical performance of the benchmark polymer photocatalyst.

Next, building on the diffusion length measurement and negative function of the deep trap states on the surface, a new nanostructure composed of B-doped g-C_3N_4 (100nm) and bulk g-C_3N_4 (900 nm) was constructed which exhibited significantly higher PEC performance than a g-C_3N_4 film. The resulting nanojunciton film shows a high photocurrent density of 103.2 μA/cm^2 at 1.23V vs RHE under one sun condition and a high IPCE of 10% at 400 nm, which is 10 times higher than that of pristine carbon nitride photoanode. Data from XPS, UV-vis, and PEC analysis show that the surface nanolayer doping can significantly improve the solar to fuel conversion efficiency but without dramatically changing the bandgap and bulk properties. Such enhancement is mainly due to the efficient charge separation and fast charge transfer in the nanojunction as evidenced by EIS, MS and IMPS spectroscopies. Furthermore,

the H_2O_2 addition proves that the efficient charge separation can be achieved by the nanojunciton itself. This surface nanojuction strategy can be extended to other semiconductors to efficiently improve their applications in the fields of solar fuel conversion and environmental purification.

Finally, I attempted to realize the photocathode performance of g-C_3N_4 film following successes in photoanode design. The crucial role of defects in converting n-type semiconductor films from photoanodes to photocathodes was demonstrated. The photocathode performance was related to the presence of electron traps associated with the synergy of N-defects and C-OH terminal groups. This new understanding demonstrated that g-C_3N_4 can be both photoanode and photocathode candidates and could aid the rational development and improvement of sustainable organic photoelectrochemical systems for water splitting.

7.2 Future work

Based on the outcomes from my PhD programme project, a polymer such as g-C_3N_4 has the potential to be efficient photoanode and photocathode for solar energy conversion. However, a few problems needs to be further addressed, 1) fundamental understandings on water redox by C_3N_4 photoelectrodes is not clear; 2) developing suitable co-catalyst for water oxidation reaction is imperative; 3) most importantly, the low conductivity in bulk g-C_3N_4 due to the low charge carrier density still limits the PEC application of g-C_3N_4 films. Therefore, a few of future works are proposed here.

1) A combination of heteroatoms doping strategy and shallow trap states introducing strategy will be a promising approach following this thesis.

For example, boron-doped g-C_3N_4 can be sonicated into nanosheets, which will be further processed into a thin film of 600 nm. The high conductivity arising from heavily doping, coupling with shallow trapped electrons with extended lifetime, is likely to result into a high-performance g-C_3N_4 photocathode. More importantly, B-doped g-C_3N_4 and P-doped g-C_3N_4 nanosheets will be further processed into nanojunction thin films, where efficient charge separation is guaranteed.

2) Another important future work is preparing suitable co-catalyst to fully explore the potential of polymer photoelectrodes. The function of co-catalyst is not only enhancing the charge separation at the electrode/electrolyte interface, but also provides active sites for water redox. For example, Pt is suitable for H_2 evolution reaction, while IrO_2 is favourable for O_2 evolution reaction. Promising co-catalyst, such as Pt, PtO_x, IrO_2, Co-Pi, CoO_x, which could assist the water oxidation and reduction reactions will be applied to further improve the photocatalytic activity of polymer photoelectrodes.

3) High temperature (> 500°C) pressing method is another promising strategy which has rarely been tried for the polymer photoelectrode fabrication. The high-temperature pressing method can physically enhance the contact among particles, therefore, enhancing the electron migration among these particles. The most advantage of this method will be fabrication of solid-state Z-scheme devices (section 2.2.8) with two photocatalysts deposited on different sides for H_2 and O_2 generation, respectively. If the efficient electron migration between two

photocatalysts films can be achieved via a mediator such as copper foil, a smart solid-state device for overall water splitting will come true.

4) Beyond the scope of the PEC system, g-C_3N_4 can also be designed for other applications. For example, the HCl-assist g-C_3N_4 (preparation method in section 3.1.3) has a uniform and porous structure which is a very suitable substrate for an enzyme for the electrochemical reduction reaction. The porous structure could firmly capture the enzyme and inject photo-generated electron from its negative conduction band to the enzyme for reduction reaction such as CO_2 reduction.
5) Although g-C_3N_4 is a 2-D material with giant delocalized π bond which somehow benefits its conductivity, its unique crystal structure makes the conductivity still much worse than perfect 2-D material such as graphene. However, the conducting graphene has a zero bandgap, which cannot utilize the energy of photons for photosynthesis. It will be interesting to introduce N atoms in the structure of graphene by substitutional doping. N atoms doping could open the bandgap of graphene, but perverse most conductivity of the graphene material. Such an N-graphene material still has the tunable band structure but much better electron mobility than that in g-C_3N_4. I believe this doping strategy can come out a series of narrow bandgap polymer semiconductors with tunable band structure and good conductivity, which is promising for PEC hydrogen fuel synthesis in the future.

8 Bibliography

1. Schwartzman, P.; Schwartzman, D., A solar transition is possible. *Institute for Policy Research & Development, London* **2011**.
2. Barroso, M.; Pendlebury, S. R.; Cowan, A. J.; Durrant, J. R., Charge carrier trapping, recombination and transfer in hematite (α-Fe 2 O 3) water splitting photoanodes. *Chemical Science* **2013,** *4* (7), 2724-2734.
3. Lewerenz, H. J., Photoelectrochemical Energy Conversion. *ChemPhysChem* **2012,** *13* (12), 2807-2808.
4. Fujishima, A.; Honda, K., TiO2 photoelectrochemistry and photocatalysis. *Nature* **1972,** *238* (5358), 37-38.
5. Khan, S. U.; Al-Shahry, M.; Ingler, W. B., Efficient photochemical water splitting by a chemically modified n-TiO2. *science* **2002,** *297* (5590), 2243-2245.
6. Luo, W.; Yang, Z.; Li, Z.; Zhang, J.; Liu, J.; Zhao, Z.; Wang, Z.; Yan, S.; Yu, T.; Zou, Z., Solar hydrogen generation from seawater with a modified BiVO4 photoanode. *Energy & Environmental Science* **2011,** *4* (10), 4046-4051.
7. Su, J.; Guo, L.; Bao, N.; Grimes, C. A., Nanostructured WO3/BiVO4 heterojunction films for efficient photoelectrochemical water splitting. *Nano letters* **2011,** *11* (5), 1928-1933.
8. Sivula, K.; Le Formal, F.; Grätzel, M., Solar water splitting: progress using hematite (α ‐ Fe2O3) photoelectrodes. *ChemSusChem* **2011,** *4* (4), 432-449.
9. Martin, D. J.; Umezawa, N.; Chen, X.; Ye, J.; Tang, J., Facet engineered Ag 3 PO 4 for efficient water photooxidation. *Energy & Environmental Science* **2013,** *6* (11), 3380-3386.
10. Wang, X.; Maeda, K.; Thomas, A.; Takanabe, K.; Xin, G.; Carlsson, J. M.; Domen, K.; Antonietti, M., A metal-free polymeric photocatalyst for hydrogen production from water under visible light. *Nature materials* **2009,** *8* (1), 76.
11. Liu, J.; Liu, Y.; Liu, N.; Han, Y.; Zhang, X.; Huang, H.; Lifshitz, Y.; Lee, S.-T.; Zhong, J.; Kang, Z. J. S., Metal-free efficient photocatalyst for stable visible water splitting via a two-electron pathway. **2015,** *347* (6225), 970-974.
12. de Greef, T. F.; Meijer, E., Materials science: supramolecular polymers. *Nature* **2008,** *453* (7192), 171-173.
13. Weisbuch, C.; Vinter, B., *Quantum semiconductor structures: fundamentals and applications*. Academic press: 2014.
14. Neamen, D., *Semiconductor physics and devices*. McGraw-Hill, Inc.: 2002.
15. Jeon, T.-I.; Grischkowsky, D., Nature of conduction in doped silicon. *Physical Review Letters* **1997,** *78* (6), 1106.
16. Zhang, Y.; Mori, T.; Ye, J.; Antonietti, M., Phosphorus-doped carbon nitride solid: enhanced electrical conductivity and photocurrent generation. *Journal of the American Chemical Society* **2010,** *132* (18), 6294-6295.
17. Pierret, R., Semiconductor Device Fundamentals, Addision-Wesley. *Reading, Massachusetts* **1996**.
18. Shockley, W., On the surface states associated with a periodic potential. *Physical review* **1939,** *56* (4), 317.
19. Kudo, A.; Miseki, Y., Heterogeneous photocatalyst materials for water splitting. *Chemical Society Reviews* **2009,** *38* (1), 253-278.
20. Xu, H.; Ouyang, S.; Liu, L.; Reunchan, P.; Umezawa, N.; Ye, J., Recent advances in TiO 2-based photocatalysis. *Journal of Materials Chemistry A* **2014,** *2* (32), 12642-12661.
21. Scanlon, D. O.; Dunnill, C. W.; Buckeridge, J.; Shevlin, S. A.; Logsdail, A. J.; Woodley, S. M.; Catlow, C. R. A.; Powell, M. J.; Palgrave, R. G.; Parkin, I. P., Band alignment of rutile and anatase TiO2. *Nature materials* **2013,** *12* (9), 798-801.

22. Murphy, A.; Barnes, P.; Randeniya, L.; Plumb, I.; Grey, I.; Horne, M.; Glasscock, J., Efficiency of solar water splitting using semiconductor electrodes. *International journal of hydrogen energy* **2006,** *31* (14), 1999-2017.
23. Halary-Wagner, E.; Wagner, F.; Hoffmann, P., Titanium dioxide thin-film deposition on polymer substrate by light induced chemical vapor deposition. *Journal of the Electrochemical Society* **2004,** *151* (9), C571-C576.
24. Park, J. H.; Kim, S.; Bard, A. J., Novel carbon-doped TiO2 nanotube arrays with high aspect ratios for efficient solar water splitting. *Nano letters* **2006,** *6* (1), 24-28.
25. Varley, J.; Janotti, A.; Van de Walle, C., Mechanism of Visible‐Light Photocatalysis in Nitrogen‐Doped TiO2. *Advanced Materials* **2011,** *23* (20), 2343-2347.
26. Fang, W. Q.; Huo, Z.; Liu, P.; Wang, X. L.; Zhang, M.; Jia, Y.; Zhang, H.; Zhao, H.; Yang, H. G.; Yao, X., Fluorine‐Doped Porous Single‐Crystal Rutile TiO2 Nanorods for Enhancing Photoelectrochemical Water Splitting. *Chemistry–A European Journal* **2014,** *20* (36), 11439-11444.
27. Altomare, M.; Lee, K.; Killian, M. S.; Selli, E.; Schmuki, P., Ta‐Doped TiO2 Nanotubes for Enhanced Solar‐Light Photoelectrochemical Water Splitting. *Chemistry–A European Journal* **2013,** *19* (19), 5841-5844.
28. Yang, M.; Kim, D.; Jha, H.; Lee, K.; Paul, J.; Schmuki, P., Nb doping of TiO 2 nanotubes for an enhanced efficiency of dye-sensitized solar cells. *Chemical Communications* **2011,** *47* (7), 2032-2034.
29. Sato, J.; Saito, N.; Yamada, Y.; Maeda, K.; Takata, T.; Kondo, J. N.; Hara, M.; Kobayashi, H.; Domen, K.; Inoue, Y., RuO2-loaded β-Ge3N4 as a non-oxide photocatalyst for overall water splitting. *Journal of the American Chemical Society* **2005,** *127* (12), 4150-4151.
30. Li, Y.; Takata, T.; Cha, D.; Takanabe, K.; Minegishi, T.; Kubota, J.; Domen, K., Vertically Aligned Ta3N5 Nanorod Arrays for Solar‐Driven Photoelectrochemical Water Splitting. *Advanced materials* **2013,** *25* (1), 125-131.
31. Abe, R.; Higashi, M.; Domen, K., Facile fabrication of an efficient oxynitride TaON photoanode for overall water splitting into H2 and O2 under visible light irradiation. *Journal of the American Chemical Society* **2010,** *132* (34), 11828-11829.
32. Sathish, M.; Viswanathan, B.; Viswanath, R., Alternate synthetic strategy for the preparation of CdS nanoparticles and its exploitation for water splitting. *International Journal of Hydrogen Energy* **2006,** *31* (7), 891-898.
33. Maeda, K.; Domen, K., New non-oxide photocatalysts designed for overall water splitting under visible light. *The Journal of Physical Chemistry C* **2007,** *111* (22), 7851-7861.
34. Maeda, K.; Takata, T.; Hara, M.; Saito, N.; Inoue, Y.; Kobayashi, H.; Domen, K., GaN: ZnO solid solution as a photocatalyst for visible-light-driven overall water splitting. *Journal of the American Chemical Society* **2005,** *127* (23), 8286-8287.
35. Zhang, G.; Lan, Z.-A.; Lin, L.; Lin, S.; Wang, X., Overall water splitting by Pt/gC 3 N 4 photocatalysts without using sacrificial agents. *Chemical science* **2016,** *7* (5), 3062-3066.
36. Liu, J.; Liu, Y.; Liu, N.; Han, Y.; Zhang, X.; Huang, H.; Lifshitz, Y.; Lee, S.-T.; Zhong, J.; Kang, Z., Metal-free efficient photocatalyst for stable visible water splitting via a two-electron pathway. *Science* **2015,** *347* (6225), 970-974.
37. Fujishima, A.; Honda, K., Electrochemical evidence for the mechanism of the primary stage of photosynthesis. *Bulletin of the chemical society of Japan* **1971,** *44* (4), 1148-1150.
38. Inoue, T.; Fujishima, A.; Konishi, S.; Honda, K., Photoelectrocatalytic reduction of carbon dioxide in aqueous suspensions of semiconductor powders. *Nature* **1979,** *277*, 637-638.
39. Fujishima, A.; Honda, K., Photolysis-decomposition of water at the surface of an irradiated semiconductor. *Nature* **1972,** *238* (5385), 37-38.

40. Fujishima, A.; Kohayakawa, K.; Honda, K., Hydrogen production under sunlight with an electrochemical photocell. *Journal of the Electrochemical Society* **1975,** *122*, 1487-1489.
41. Lee, Y.; Suntivich, J.; May, K. J.; Perry, E. E.; Shao-Horn, Y., Synthesis and activities of rutile IrO2 and RuO2 nanoparticles for oxygen evolution in acid and alkaline solutions. *The journal of physical chemistry letters* **2012,** *3* (3), 399-404.
42. Walter, M. G.; Warren, E. L.; McKone, J. R.; Boettcher, S. W.; Mi, Q.; Santori, E. A.; Lewis, N. S., Solar water splitting cells. *Chemical reviews* **2010,** *110* (11), 6446-6473.
43. Kay, A.; Cesar, I.; Grätzel, M., New benchmark for water photooxidation by nanostructured α-Fe2O3 films. *Journal of the American Chemical Society* **2006,** *128* (49), 15714-15721.
44. Albery, W. J.; Bartlett, P. N., The transport and kinetics of photogenerated carriers in colloidal semiconductor electrode particles. *Journal of the Electrochemical Society* **1984,** *131* (2), 315-325.
45. Peter, L. M., Photoelectrochemistry: From Basic Principles to Photocatalysis. **2016**.
46. van de Krol, R., Principles of photoelectrochemical cells. In *Photoelectrochemical hydrogen production*, Springer: 2012; pp 13-67.
47. Morrison, S. R., Electrochemistry at semiconductor and oxidized metal electrodes. **1980**.
48. Brus, L. E., Electron–electron and electron‐hole interactions in small semiconductor crystallites: The size dependence of the lowest excited electronic state. *The Journal of chemical physics* **1984,** *80* (9), 4403-4409.
49. Barroso, M.; Cowan, A. J.; Pendlebury, S. R.; Grätzel, M.; Klug, D. R.; Durrant, J. R., The role of cobalt phosphate in enhancing the photocatalytic activity of α-Fe2O3 toward water oxidation. *Journal of the American Chemical Society* **2011,** *133* (38), 14868-14871.
50. van de Krol, R.; Liang, Y.; Schoonman, J., Solar hydrogen production with nanostructured metal oxides. *Journal of Materials Chemistry* **2008,** *18* (20), 2311-2320.
51. Margossian, T.; Culver, S. P.; Larmier, K.; Zhu, F.; Brutchey, R. L.; Copéret, C., Composition-dependent surface chemistry of colloidal Ba x Sr 1− x TiO 3 perovskite nanocrystals. *Chemical Communications* **2016,** *52* (95), 13791-13794.
52. Modak, B.; Ghosh, S. K., An Efficient Strategy for Controlled Band Gap Engineering of KTaO3. *The Journal of Physical Chemistry C* **2016,** *120* (13), 6920-6929.
53. Wang, Q.; Hisatomi, T.; Jia, Q.; Tokudome, H.; Zhong, M.; Wang, C.; Pan, Z.; Takata, T.; Nakabayashi, M.; Shibata, N., Scalable water splitting on particulate photocatalyst sheets with a solar-to-hydrogen energy conversion efficiency exceeding 1%. *Nature materials* **2016,** *15* (6), 611-615.
54. Wang, Q.; Hisatomi, T.; Suzuki, Y.; Pan, Z.; Seo, J.; Katayama, M.; Minegishi, T.; Nishiyama, H.; Takata, T.; Seki, K., Particulate photocatalyst sheets based on carbon conductor layer for efficient Z-scheme pure-water splitting at ambient pressure. *Journal of the American Chemical Society* **2017**.
55. Khaselev, O.; Turner, J. A., A monolithic photovoltaic-photoelectrochemical device for hydrogen production via water splitting. *Science* **1998,** *280* (5362), 425-427.
56. Van de Krol, R.; Grätzel, M., *Photoelectrochemical hydrogen production*. Springer: 2012; Vol. 90.
57. Wang, Y.; Vogel, A.; Sachs, M.; Sprick, R. S.; Wilbraham, L.; Moniz, S. J.; Godin, R.; Zwijnenburg, M. A.; Durrant, J. R.; Cooper, A. I., Current understanding and challenges of solar-driven hydrogen generation using polymeric photocatalysts. *Nature Energy* **2019**, 1-15.
58. Liu, J.; Wang, H.; Antonietti, M., Graphitic carbon nitride “reloaded”: emerging applications beyond (photo) catalysis. *Chemical Society Reviews* **2016,** *45* (8), 2308-2326.

59. Thomas, A.; Fischer, A.; Goettmann, F.; Antonietti, M.; Müller, J.-O.; Schlögl, R.; Carlsson, J. M., Graphitic carbon nitride materials: variation of structure and morphology and their use as metal-free catalysts. *Journal of Materials Chemistry* **2008,** *18* (41), 4893-4908.
60. Dong, G.; Zhang, Y.; Pan, Q.; Qiu, J., A fantastic graphitic carbon nitride (gC 3 N 4) material: electronic structure, photocatalytic and photoelectronic properties. *Journal of Photochemistry and Photobiology C: Photochemistry Reviews* **2014,** *20*, 33-50.
61. Liu, G.; Niu, P.; Sun, C.; Smith, S. C.; Chen, Z.; Lu, G. Q.; Cheng, H.-M., Unique electronic structure induced high photoreactivity of sulfur-doped graphitic C3N4. *Journal of the American Chemical Society* **2010,** *132* (33), 11642-11648.
62. Wang, Y.; Di, Y.; Antonietti, M.; Li, H.; Chen, X.; Wang, X., Excellent visible-light photocatalysis of fluorinated polymeric carbon nitride solids. *Chemistry of Materials* **2010,** *22* (18), 5119-5121.
63. Wang, Y.; Wang, X.; Antonietti, M., Polymeric graphitic carbon nitride as a heterogeneous organocatalyst: from photochemistry to multipurpose catalysis to sustainable chemistry. *Angewandte Chemie International Edition* **2012,** *51* (1), 68-89.
64. Zhou, Z.; Wang, J.; Yu, J.; Shen, Y.; Li, Y.; Liu, A.; Liu, S.; Zhang, Y., Dissolution and liquid crystals phase of 2D polymeric carbon nitride. *Journal of the American Chemical Society* **2015,** *137* (6), 2179-2182.
65. Bai, X.; Yan, S.; Wang, J.; Wang, L.; Jiang, W.; Wu, S.; Sun, C.; Zhu, Y., A simple and efficient strategy for the synthesis of a chemically tailored gC 3 N 4 material. *Journal of Materials Chemistry A* **2014,** *2* (41), 17521-17529.
66. Zhang, X.; Wang, H.; Wang, H.; Zhang, Q.; Xie, J.; Tian, Y.; Wang, J.; Xie, Y., Single‐Layered Graphitic‐C3N4 Quantum Dots for Two‐Photon Fluorescence Imaging of Cellular Nucleus. *Advanced Materials* **2014,** *26* (26), 4438-4443.
67. Guo, S.; Deng, Z.; Li, M.; Jiang, B.; Tian, C.; Pan, Q.; Fu, H., Phosphorus‐doped carbon nitride tubes with a layered micro‐nanostructure for enhanced visible‐light photocatalytic hydrogen evolution. *Angewandte Chemie* **2016,** *128* (5), 1862-1866.
68. Wang, Y.; Bayazit, M. K.; Moniz, S. J.; Ruan, Q.; Lau, C. C.; Martsinovich, N.; Tang, J., Linker-controlled polymeric photocatalyst for highly efficient hydrogen evolution from water. *Energy & Environmental Science* **2017,** *10* (7), 1643-1651.
69. Hong, J.; Xia, X.; Wang, Y.; Xu, R., Mesoporous carbon nitride with in situ sulfur doping for enhanced photocatalytic hydrogen evolution from water under visible light. *Journal of Materials Chemistry* **2012,** *22* (30), 15006-15012.
70. Martin, D. J.; Qiu, K.; Shevlin, S. A.; Handoko, A. D.; Chen, X.; Guo, Z.; Tang, J., Highly efficient photocatalytic H2 evolution from water using visible light and structure‐controlled graphitic carbon nitride. *Angewandte Chemie International Edition* **2014,** *53* (35), 9240-9245.
71. Li, X.; Sergeyev, I. V.; Aussenac, F.; Masters, A. F.; Maschmeyer, T.; Hook, J. M., Dynamic Nuclear Polarization NMR Spectroscopy of Polymeric Carbon Nitride Photocatalysts: Insights into Structural Defects and Reactivity. *Angewandte Chemie* **2018,** *130* (23), 6964-6968.
72. Niu, P.; Zhang, L.; Liu, G.; Cheng, H. M., Graphene‐like carbon nitride nanosheets for improved photocatalytic activities. *Advanced Functional Materials* **2012,** *22* (22), 4763-4770.
73. Groenewolt, M.; Antonietti, M., Synthesis of g‐C3N4 Nanoparticles in Mesoporous Silica Host Matrices. *Advanced materials* **2005,** *17* (14), 1789-1792.
74. Wang, Y.; Wang, X.; Antonietti, M.; Zhang, Y., Facile One‐Pot Synthesis of Nanoporous Carbon Nitride Solids by Using Soft Templates. *ChemSusChem* **2010,** *3* (4), 435-439.
75. Li, Y.; Wang, Z.; Xia, T.; Ju, H.; Zhang, K.; Long, R.; Xu, Q.; Wang, C.; Song, L.; Zhu, J., Implementing metal‐to‐ligand charge transfer in organic semiconductor for

improved visible‐near‐infrared photocatalysis. *Advanced Materials* **2016,** *28* (32), 6959-6965.
76. Xia, X.; Deng, N.; Cui, G.; Xie, J.; Shi, X.; Zhao, Y.; Wang, Q.; Wang, W.; Tang, B., NIR light induced H 2 evolution by a metal-free photocatalyst. *Chemical communications* **2015,** *51* (54), 10899-10902.
77. Liu, G.; Wang, T.; Zhang, H.; Meng, X.; Hao, D.; Chang, K.; Li, P.; Kako, T.; Ye, J., Nature‐Inspired Environmental "Phosphorylation" Boosts Photocatalytic H2 Production over Carbon Nitride Nanosheets under Visible‐Light Irradiation. *Angewandte Chemie International Edition* **2015,** *54* (46), 13561-13565.
78. Lau, V. W.-h.; Moudrakovski, I.; Botari, T.; Weinberger, S.; Mesch, M. B.; Duppel, V.; Senker, J.; Blum, V.; Lotsch, B. V., Rational design of carbon nitride photocatalysts by identification of cyanamide defects as catalytically relevant sites. *Nature communications* **2016,** *7*, 12165.
79. Zhang, G.; Lin, L.; Li, G.; Zhang, Y.; Savateev, A.; Zafeiratos, S.; Wang, X.; Antonietti, M., Ionothermal Synthesis of Triazine–Heptazine‐Based Copolymers with Apparent Quantum Yields of 60% at 420 nm for Solar Hydrogen Production from "Sea Water". *Angewandte Chemie International Edition* **2018,** *57* (30), 9372-9376.
80. Wang, Y.; Silveri, F.; Bayazit, M. K.; Ruan, Q.; Li, Y.; Xie, J.; Catlow, C. R. A.; Tang, J., Bandgap engineering of organic semiconductors for highly efficient photocatalytic water splitting. *Advanced Energy Materials* **2018,** *8* (24), 1801084.
81. Zhang, G.; Zhang, M.; Ye, X.; Qiu, X.; Lin, S.; Wang, X., Iodine modified carbon nitride semiconductors as visible light photocatalysts for hydrogen evolution. *Advanced Materials* **2014,** *26* (5), 805-809.
82. Chen, J.; Hong, Z.; Chen, Y.; Lin, B.; Gao, B., One-step synthesis of sulfur-doped and nitrogen-deficient g-C3N4 photocatalyst for enhanced hydrogen evolution under visible light. *Materials Letters* **2015,** *145*, 129-132.
83. Zhou, Y.; Zhang, L.; Liu, J.; Fan, X.; Wang, B.; Wang, M.; Ren, W.; Wang, J.; Li, M.; Shi, J., Brand new P-doped gC 3 N 4: enhanced photocatalytic activity for H 2 evolution and Rhodamine B degradation under visible light. *Journal of Materials Chemistry A* **2015,** *3* (7), 3862-3867.
84. Lan, Z.-A.; Zhang, G.; Wang, X., A facile synthesis of Br-modified g-C3N4 semiconductors for photoredox water splitting. *Applied Catalysis B: Environmental* **2016,** *192*, 116-125.
85. Li, J.; Shen, B.; Hong, Z.; Lin, B.; Gao, B.; Chen, Y., A facile approach to synthesize novel oxygen-doped g-C 3 N 4 with superior visible-light photoreactivity. *Chemical communications* **2012,** *48* (98), 12017-12019.
86. Martin, D. J.; Qiu, K.; Shevlin, S. A.; Handoko, A. D.; Chen, X.; Guo, Z.; Tang, J. J. A. C. I. E., Highly efficient photocatalytic H2 evolution from water using visible light and structure‐controlled graphitic carbon nitride. **2014,** *53* (35), 9240-9245.
87. Bhunia, M. K.; Yamauchi, K.; Takanabe, K. J. A. C. I. E., Harvesting solar light with crystalline carbon nitrides for efficient photocatalytic hydrogen evolution. **2014,** *53* (41), 11001-11005.
88. Yang, P.; Ou, H.; Fang, Y.; Wang, X. J. A. C. I. E., A facile steam reforming strategy to delaminate layered carbon nitride semiconductors for photoredox catalysis. **2017,** *56* (14), 3992-3996.
89. Ou, H.; Lin, L.; Zheng, Y.; Yang, P.; Fang, Y.; Wang, X. J. A. M., Tri‐s‐triazine‐Based Crystalline Carbon Nitride Nanosheets for an Improved Hydrogen Evolution. **2017,** *29* (22), 1700008.
90. Yang, S.; Gong, Y.; Zhang, J.; Zhan, L.; Ma, L.; Fang, Z.; Vajtai, R.; Wang, X.; Ajayan, P. M. J. A. m., Exfoliated graphitic carbon nitride nanosheets as efficient catalysts for hydrogen evolution under visible light. **2013,** *25* (17), 2452-2456.
91. Schwinghammer, K.; Mesch, M. B.; Duppel, V.; Ziegler, C.; Senker, J. r.; Lotsch, B. V. J. J. o. t. A. C. S., Crystalline carbon nitride nanosheets for improved visible-light hydrogen evolution. **2014,** *136* (5), 1730-1733.

92. Zhang, Y.; Liu, J.; Wu, G.; Chen, W. J. N., Porous graphitic carbon nitride synthesized via direct polymerization of urea for efficient sunlight-driven photocatalytic hydrogen production. **2012,** *4* (17), 5300-5303.
93. Niu, P.; Zhang, L.; Liu, G.; Cheng, H. M. J. A. F. M., Graphene ‐ like carbon nitride nanosheets for improved photocatalytic activities. **2012,** *22* (22), 4763-4770.
94. Huang, Z.-F.; Song, J.; Pan, L.; Wang, Z.; Zhang, X.; Zou, J.-J.; Mi, W.; Zhang, X.; Wang, L., Carbon nitride with simultaneous porous network and O-doping for efficient solar-energy-driven hydrogen evolution. *Nano Energy* **2015,** *12*, 646-656.
95. Guo, S.; Deng, Z.; Li, M.; Jiang, B.; Tian, C.; Pan, Q.; Fu, H., Phosphorus ‐ doped carbon nitride tubes with a layered micro ‐ nanostructure for enhanced visible ‐ light photocatalytic hydrogen evolution. *Angewandte Chemie International Edition* **2016,** *55* (5), 1830-1834.
96. Ran, J.; Ma, T. Y.; Gao, G.; Du, X.-W.; Qiao, S. Z., Porous P-doped graphitic carbon nitride nanosheets for synergistically enhanced visible-light photocatalytic H 2 production. *Energy & Environmental Science* **2015,** *8* (12), 3708-3717.
97. She, X.; Liu, L.; Ji, H.; Mo, Z.; Li, Y.; Huang, L.; Du, D.; Xu, H.; Li, H., Template-free synthesis of 2D porous ultrathin nonmetal-doped g-C3N4 nanosheets with highly efficient photocatalytic H2 evolution from water under visible light. *Applied Catalysis B: Environmental* **2016,** *187*, 144-153.
98. Lin, Z.; Wang, X., Nanostructure engineering and doping of conjugated carbon nitride semiconductors for hydrogen photosynthesis. *Angewandte Chemie International Edition* **2013,** *52* (6), 1735-1738.
99. Zhang, G.; Lin, L.; Li, G.; Zhang, Y.; Savateev, A.; Zafeiratos, S.; Wang, X.; Antonietti, M. J. A. C. I. E., Ionothermal Synthesis of Triazine–Heptazine ‐ Based Copolymers with Apparent Quantum Yields of 60% at 420 nm for Solar Hydrogen Production from “Sea Water”. **2018,** *57* (30), 9372-9376.
100. Zhang, G.; Li, G.; Lan, Z. A.; Lin, L.; Savateev, A.; Heil, T.; Zafeiratos, S.; Wang, X.; Antonietti, M. J. A. C. I. E., Optimizing optical absorption, exciton dissociation, and charge transfer of a polymeric carbon nitride with ultrahigh solar hydrogen production activity. **2017,** *56* (43), 13445-13449.
101. Liu, G.; Wang, T.; Zhang, H.; Meng, X.; Hao, D.; Chang, K.; Li, P.; Kako, T.; Ye, J. J. A. C. I. E., Nature ‐ Inspired Environmental “Phosphorylation” Boosts Photocatalytic H2 Production over Carbon Nitride Nanosheets under Visible ‐ Light Irradiation. **2015,** *54* (46), 13561-13565.
102. Li, Y.; Wang, Z.; Xia, T.; Ju, H.; Zhang, K.; Long, R.; Xu, Q.; Wang, C.; Song, L.; Zhu, J. J. A. M., Implementing metal ‐ to ‐ ligand charge transfer in organic semiconductor for improved visible ‐ near ‐ infrared photocatalysis. **2016,** *28* (32), 6959-6965.
103. Zhang, G.; Lan, Z.-A.; Wang, X., Surface engineering of graphitic carbon nitride polymers with cocatalysts for photocatalytic overall water splitting. *Chemical science* **2017,** *8* (8), 5261-5274.
104. Zhang, H.; Tian, W.; Zhou, L.; Sun, H.; Tade, M.; Wang, S., Monodisperse Co3O4 quantum dots on porous carbon nitride nanosheets for enhanced visible-light-driven water oxidation. *Applied Catalysis B: Environmental* **2018,** *223*, 2-9.
105. Zhang, J.; Grzelczak, M.; Hou, Y.; Maeda, K.; Domen, K.; Fu, X.; Antonietti, M.; Wang, X., Photocatalytic oxidation of water by polymeric carbon nitride nanohybrids made of sustainable elements. *Chemical Science* **2012,** *3* (2), 443-446.
106. Liu, J.; Zhang, Y.; Lu, L.; Wu, G.; Chen, W., Self-regenerated solar-driven photocatalytic water-splitting by urea derived graphitic carbon nitride with platinum nanoparticles. *Chemical Communications* **2012,** *48* (70), 8826-8828.
107. Wang, L.; Wan, Y.; Ding, Y.; Wu, S.; Zhang, Y.; Zhang, X.; Zhang, G.; Xiong, Y.; Wu, X.; Yang, J., Conjugated microporous polymer nanosheets for overall water splitting using visible light. *Advanced Materials* **2017,** *29* (38), 1702428.

108. Che, W.; Cheng, W.; Yao, T.; Tang, F.; Liu, W.; Su, H.; Huang, Y.; Liu, Q.; Liu, J.; Hu, F., Fast photoelectron transfer in (Cring)–C3N4 plane heterostructural nanosheets for overall water splitting. *Journal of the American Chemical Society* **2017,** *139* (8), 3021-3026.
109. Zhang, G.; Lan, Z.-A.; Wang, X. J. C. s., Surface engineering of graphitic carbon nitride polymers with cocatalysts for photocatalytic overall water splitting. **2017,** *8* (8), 5261-5274.
110. Chen, X.; Shi, R.; Chen, Q.; Zhang, Z.; Jiang, W.; Zhu, Y.; Zhang, T. J. N. E., Three-dimensional porous g-C3N4 for highly efficient photocatalytic overall water splitting. **2019**.
111. Maeda, K.; Higashi, M.; Lu, D.; Abe, R.; Domen, K. J. J. o. t. A. C. S., Efficient nonsacrificial water splitting through two-step photoexcitation by visible light using a modified oxynitride as a hydrogen evolution photocatalyst. **2010,** *132* (16), 5858-5868.
112. Wang, Q.; Hisatomi, T.; Jia, Q.; Tokudome, H.; Zhong, M.; Wang, C.; Pan, Z.; Takata, T.; Nakabayashi, M.; Shibata, N. J. N. m., Scalable water splitting on particulate photocatalyst sheets with a solar-to-hydrogen energy conversion efficiency exceeding 1%. **2016,** *15* (6), 611.
113. Wang, Q.; Hisatomi, T.; Suzuki, Y.; Pan, Z.; Seo, J.; Katayama, M.; Minegishi, T.; Nishiyama, H.; Takata, T.; Seki, K. J. J. o. t. A. C. S., Particulate photocatalyst sheets based on carbon conductor layer for efficient Z-scheme pure-water splitting at ambient pressure. **2017,** *139* (4), 1675-1683.
114. Pan, Z.; Zhang, G.; Wang, X. J. A. C., Polymeric Carbon Nitride/RGO/Fe2O3: All Solid State Z‐scheme Systems for Photocatalytic Overall Water Splitting. **2019**.
115. Martin, D. J.; Reardon, P. J. T.; Moniz, S. J.; Tang, J., Visible light-driven pure water splitting by a nature-inspired organic semiconductor-based system. *Journal of the American Chemical Society* **2014,** *136* (36), 12568-12571.
116. Zhang, X.; Xie, X.; Wang, H.; Zhang, J.; Pan, B.; Xie, Y., Enhanced photoresponsive ultrathin graphitic-phase C3N4 nanosheets for bioimaging. *Journal of the American Chemical Society* **2012,** *135* (1), 18-21.
117. Zhang, J.; Zhang, M.; Lin, L.; Wang, X., Sol processing of conjugated carbon nitride powders for thin‐film fabrication. *Angewandte Chemie International Edition* **2015,** *54* (21), 6297-6301.
118. Xu, J.; Brenner, T. J.; Chabanne, L.; Neher, D.; Antonietti, M.; Shalom, M., Liquid-Based Growth of Polymeric Carbon Nitride Layers and Their Use in a Mesostructured Polymer Solar Cell with V oc Exceeding 1 V. *Journal of the American Chemical Society* **2014,** *136* (39), 13486-13489.
119. Bian, J.; Xi, L.; Huang, C.; Lange, K. M.; Zhang, R. Q.; Shalom, M., Efficiency Enhancement of Carbon Nitride Photoelectrochemical Cells via Tailored Monomers Design. *Advanced Energy Materials* **2016**.
120. Liu, J.; Wang, H.; Chen, Z. P.; Moehwald, H.; Fiechter, S.; van de Krol, R.; Wen, L.; Jiang, L.; Antonietti, M., Microcontact‐Printing‐Assisted Access of Graphitic Carbon Nitride Films with Favorable Textures toward Photoelectrochemical Application. *Advanced Materials* **2015,** *27* (4), 712-718.
121. Peng, G.; Xing, L.; Barrio, J.; Volokh, M.; Shalom, M. J. A. C. I. E., A general synthesis of porous carbon nitride films with tunable surface area and photophysical properties. **2018,** *57* (5), 1186-1192.
122. Ruan, Q.; Luo, W.; Xie, J.; Wang, Y.; Liu, X.; Bai, Z.; Carmalt, C. J.; Tang, J. J. A. C. I. E., A nanojunction polymer photoelectrode for efficient charge transport and separation. **2017,** *56* (28), 8221-8225.
123. Peng, G.; Volokh, M.; Tzadikov, J.; Sun, J.; Shalom, M. J. A. E. M., Carbon Nitride/Reduced Graphene Oxide Film with Enhanced Electron Diffusion Length: An Efficient Photo‐Electrochemical Cell for Hydrogen Generation. **2018,** *8* (23), 1800566.
124. Wang, R.; Liu, H.; Fan, Z.; Li, L.; Cai, Y.; Xu, G.; Luo, W.; Yang, B.; Zhou, Y.; Zou, Z. J. N., Unconventional gas-based bottom-up, meter-area-scale fabrication of

hydrogen-bond free g-CN nanorod arrays and coupling layers with TiO 2 toward high-efficiency photoelectrochemical performance. **2018,** *10* (7), 3342-3349.
125. Park, T. J.; Pawar, R. C.; Kang, S.; Lee, C. S. J. R. A., Ultra-thin coating of gC 3 N 4 on an aligned ZnO nanorod film for rapid charge separation and improved photodegradation performance. **2016,** *6* (92), 89944-89952.
126. An, X.; Hu, C.; Lan, H.; Liu, H.; Qu, J. J. A. a. m.; interfaces, Strongly Coupled Metal Oxide/Reassembled Carbon Nitride/Co–Pi Heterostructures for Efficient Photoelectrochemical Water Splitting. **2018,** *10* (7), 6424-6432.
127. Tang, J.; Durrant, J. R.; Klug, D. R. J. J. o. t. A. C. S., Mechanism of photocatalytic water splitting in TiO2. Reaction of water with photoholes, importance of charge carrier dynamics, and evidence for four-hole chemistry. **2008,** *130* (42), 13885-13891.
128. Zhang, G.; Huang, C.; Wang, X. J. S., Dispersing molecular cobalt in graphitic carbon nitride frameworks for photocatalytic water oxidation. **2015,** *11* (9-10), 1215-1221.
129. Zhang, W.; Albero, J.; Xi, L.; Lange, K. M.; Garcia, H.; Wang, X.; Shalom, M. J. A. a. m.; interfaces, One-Pot Synthesis of Nickel-Modified Carbon Nitride Layers Toward Efficient Photoelectrochemical Cells. **2017,** *9* (38), 32667-32677.
130. Zhang, G.; Zang, S.; Lin, L.; Lan, Z.-A.; Li, G.; Wang, X. J. A. a. m.; interfaces, Ultrafine cobalt catalysts on covalent carbon nitride frameworks for oxygenic photosynthesis. **2016,** *8* (3), 2287-2296.
131. Lu, X.; Liu, Z.; Li, J.; Zhang, J.; Guo, Z. J. A. C. B. E., Novel framework g-C3N4 film as efficient photoanode for photoelectrochemical water splitting. **2017,** *209*, 657-662.
132. Hou, Y.; Wen, Z.; Cui, S.; Feng, X.; Chen, J. J. N. l., Strongly coupled ternary hybrid aerogels of N-deficient porous graphitic-C3N4 nanosheets/N-doped graphene/NiFe-layered double hydroxide for solar-driven photoelectrochemical water oxidation. **2016,** *16* (4), 2268-2277.
133. Lv, X.; Cao, M.; Shi, W.; Wang, M.; Shen, Y. J. C., A new strategy of preparing uniform graphitic carbon nitride films for photoelectrochemical application. **2017,** *117*, 343-350.
134. Liu, J.; Wang, H.; Chen, Z. P.; Moehwald, H.; Fiechter, S.; van de Krol, R.; Wen, L.; Jiang, L.; Antonietti, M. J. A. M., Microcontact‐Printing‐Assisted Access of Graphitic Carbon Nitride Films with Favorable Textures toward Photoelectrochemical Application. **2015,** *27* (4), 712-718.
135. Bian, J.; Li, Q.; Huang, C.; Li, J.; Guo, Y.; Zaw, M.; Zhang, R.-Q. J. N. E., Thermal vapor condensation of uniform graphitic carbon nitride films with remarkable photocurrent density for photoelectrochemical applications. **2015,** *15*, 353-361.
136. Bian, J.; Xi, L.; Huang, C.; Lange, K. M.; Zhang, R. Q.; Shalom, M. J. A. E. M., Efficiency enhancement of carbon nitride photoelectrochemical cells via tailored monomers design. **2016,** *6* (12), 1600263.
137. Han, Y. Y.; Lu, X. L.; Tang, S. F.; Yin, X. P.; Wei, Z. W.; Lu, T. B., Metal‐Free 2D/2D Heterojunction of Graphitic Carbon Nitride/Graphdiyne for Improving the Hole Mobility of Graphitic Carbon Nitride. *Advanced Energy Materials* **2018,** *8* (16), 1702992.
138. Leng, W.; Barnes, P. R.; Juozapavicius, M.; O'Regan, B. C.; Durrant, J. R., Electron diffusion length in mesoporous nanocrystalline TiO2 photoelectrodes during water oxidation. *The Journal of Physical Chemistry Letters* **2010,** *1* (6), 967-972.
139. Lindgren, T.; Vayssieres, L.; Wang, H.; Lindquist, S.-E., Photo-oxidation of water at hematite electrodes. *Chemical physics of nanostructured semiconductors* **2003**, 83-110.
140. Galuza, A.; Beznosov, A.; Eremenko, V., Optical absorption edge in alpha-Fe2O3: the exciton-magnon structure. *Low Temperature Physics* **1998,** *24*, 726-729.
141. Cesar, I.; Kay, A.; Gonzalez Martinez, J. A.; Grätzel, M., Translucent thin film Fe2O3 photoanodes for efficient water splitting by sunlight: nanostructure-directing

effect of Si-doping. *Journal of the American Chemical Society* **2006,** *128* (14), 4582-4583.
142. Wheeler, D. A.; Wang, G.; Ling, Y.; Li, Y.; Zhang, J. Z., Nanostructured hematite: synthesis, characterization, charge carrier dynamics, and photoelectrochemical properties. *Energy & Environmental Science* **2012,** *5* (5), 6682-6702.
143. Lichterman, M. F.; Carim, A. I.; McDowell, M. T.; Hu, S.; Gray, H. B.; Brunschwig, B. S.; Lewis, N. S., Stabilization of n-cadmium telluride photoanodes for water oxidation to O 2 (g) in aqueous alkaline electrolytes using amorphous TiO 2 films formed by atomic-layer deposition. *Energy & Environmental Science* **2014,** *7* (10), 3334-3337.
144. Li, Z.; Luo, W.; Zhang, M.; Feng, J.; Zou, Z., Photoelectrochemical cells for solar hydrogen production: current state of promising photoelectrodes, methods to improve their properties, and outlook. *Energy & Environmental Science* **2013,** *6* (2), 347-370.
145. Zhong, D. K.; Choi, S.; Gamelin, D. R., Near-complete suppression of surface recombination in solar photoelectrolysis by "Co-Pi" catalyst-modified W: BiVO4. *Journal of the American Chemical Society* **2011,** *133* (45), 18370-18377.
146. Chang, S.-m.; Liu, W.-s., Surface doping is more beneficial than bulk doping to the photocatalytic activity of vanadium-doped TiO 2. *Applied Catalysis B: Environmental* **2011,** *101* (3), 333-342.
147. Tang, J.; Durrant, J. R.; Klug, D. R., Mechanism of photocatalytic water splitting in TiO2. Reaction of water with photoholes, importance of charge carrier dynamics, and evidence for four-hole chemistry. *Journal of the American Chemical Society* **2008,** *130* (42), 13885-13891.
148. Tilley, S. D.; Cornuz, M.; Sivula, K.; Grätzel, M., Light‐Induced Water Splitting with Hematite: Improved Nanostructure and Iridium Oxide Catalysis. *Angewandte Chemie* **2010,** *122* (36), 6549-6552.
149. Kanan, M. W.; Nocera, D. G., In situ formation of an oxygen-evolving catalyst in neutral water containing phosphate and Co2+. *Science* **2008,** *321* (5892), 1072-1075.
150. Kim, J. Y.; Magesh, G.; Youn, D. H.; Jang, J.-W.; Kubota, J.; Domen, K.; Lee, J. S., Single-crystalline, wormlike hematite photoanodes for efficient solar water splitting. *Scientific reports* **2013,** *3*, 2681.
151. Ahmed, S.; Leduc, J.; Haller, S., Photoelectrochemical and impedance characteristics of specular hematite. 1. Photoelectrochemical parallel conductance, and trap rate studies. *The Journal of Physical Chemistry* **1988,** *92* (23), 6655-6660.
152. Godin, R.; Wang, Y.; Zwijnenburg, M. A.; Tang, J.; Durrant, J. R., Time-resolved spectroscopic investigation of charge trapping in carbon nitrides photocatalysts for hydrogen generation. *Journal of the American Chemical Society* **2017,** *139* (14), 5216-5224.
153. Maschmeyer, T.; Li, X.; Sergeyev, I.; Aussenac, F.; Masters, A.; Hook, J., DNP NMR Spectroscopy of Polymeric Carbon Nitride Photocatalysts: Insight into Structural Defects and Reactivity. *Angewandte Chemie* **2018**.
154. Peng, G.; Volokh, M.; Tzadikov, J.; Sun, J.; Shalom, M., Carbon Nitride/Reduced Graphene Oxide Film with Enhanced Electron Diffusion Length: An Efficient Photo‐Electrochemical Cell for Hydrogen Generation. *Advanced Energy Materials* **2018,** *8* (23), 1800566.
155. Tauc, J., Optical properties and electronic structure of amorphous Ge and Si. *Materials Research Bulletin* **1968,** *3* (1), 37-46.
156. Hwang, G. W.; Kim, D.; Cordero, J. M.; Wilson, M. W.; Chuang, C. H. M.; Grossman, J. C.; Bawendi, M. G., Identifying and Eliminating Emissive Sub‐bandgap States in Thin Films of PbS Nanocrystals. *Advanced Materials* **2015,** *27* (30), 4481-4486.
157. Sears, F. W.; Zemansky, M. W., University physics. **1964**.

158. Vanmaekelbergh, D.; Gomes, W.; Cardon, F., A Quantitative Analysis of Photoinduced Capacitance Peaks in the Impedance of the n‐GaAs Electrode. *Journal of The Electrochemical Society* **1987,** *134* (4), 891-894.
159. Rajeshwar, K., Fundamentals of semiconductor electrochemistry and photoelectrochemistry. *Encyclopedia of electrochemistry* **2007**.
160. Ponomarev, E.; Peter, L., A generalized theory of intensity modulated photocurrent spectroscopy (IMPS). *Journal of Electroanalytical Chemistry* **1995,** *396* (1), 219-226.
161. Peter, L. M.; Wijayantha, K. U.; Tahir, A. A., Kinetics of light-driven oxygen evolution at α-Fe 2 O 3 electrodes. *Faraday discussions* **2012,** *155*, 309-322.
162. Pu, Y.-C.; Wang, G.; Chang, K.-D.; Ling, Y.; Lin, Y.-K.; Fitzmorris, B. C.; Liu, C.-M.; Lu, X.; Tong, Y.; Zhang, J. Z., Au nanostructure-decorated TiO2 nanowires exhibiting photoactivity across entire UV-visible region for photoelectrochemical water splitting. *Nano letters* **2013,** *13* (8), 3817-3823.
163. Liu, W.; Cao, L.; Cheng, W.; Cao, Y.; Liu, X.; Zhang, W.; Mou, X.; Jin, L.; Zheng, X.; Che, W., Single‐site active cobalt‐based photocatalyst with long carriers lifetime for spontaneous overall water splitting. *Angewandte Chemie International Edition* **2017**.
164. Bai, S.; Yang, L.; Wang, C.; Lin, Y.; Lu, J.; Jiang, J.; Xiong, Y., Boosting Photocatalytic Water Splitting: Interfacial Charge Polarization in Atomically Controlled Core–Shell Cocatalysts. *Angewandte Chemie International Edition* **2015,** *54* (49), 14810-14814.
165. Zhou, Y.; Zou, Z.; Luo, W.; Yang, B.; Xu, G.; Cai, Y.; Li, L.; Fan, Z.; Liu, H.; Wang, R., Unconventional Gas-Based Bottom-up, Meter-Area-Scale Fabrication of Hydrogen-Bond Free g-CN Nanorod Arrays and Coupling Layers with TiO2 toward High-Efficient Photoelectrichemical Performance. *Nanoscale* **2018**.
166. Zhu, M.; Kim, S.; Mao, L.; Fujitsuka, M.; Zhang, J.; Wang, X.; Majima, T., Metal-free photocatalyst for H2 evolution in visible to near-infrared region: black phosphorus/graphitic carbon nitride. *Journal of the American Chemical Society* **2017,** *139* (37), 13234-13242.
167. Kasap, H.; Achilleos, D. S.; Huang, A.; Reisner, E., Photoreforming of Lignocellulose into H2 Using Nanoengineered Carbon Nitride under Benign Conditions. *Journal of the American Chemical Society* **2018,** *140* (37), 11604-11607.
168. Cometto, C.; Kuriki, R.; Chen, L.; Maeda, K.; Lau, T.-C.; Ishitani, O.; Robert, M., A Carbon Nitride/Fe Quaterpyridine Catalytic System for Photostimulated CO2-to-CO Conversion with Visible Light. *Journal of the American Chemical Society* **2018**.
169. Wang, H.; Yuan, X.; Wang, H.; Chen, X.; Wu, Z.; Jiang, L.; Xiong, W.; Zeng, G., Facile synthesis of Sb2S3/ultrathin g-C3N4 sheets heterostructures embedded with g-C3N4 quantum dots with enhanced NIR-light photocatalytic performance. *Applied Catalysis B: Environmental* **2016,** *193*, 36-46.
170. Fu, Q.; Ruan, Q.; McKenzie, T. G.; Reyhani, A.; Tang, J.; Qiao, G. G., Development of a Robust PET-RAFT Polymerization Using Graphitic Carbon Nitride (g-C3N4). *Macromolecules* **2017,** *50* (19), 7509-7516.
171. Ou, H.; Lin, L.; Zheng, Y.; Yang, P.; Fang, Y.; Wang, X., Tri‐s‐triazine‐Based Crystalline Carbon Nitride Nanosheets for an Improved Hydrogen Evolution. *Advanced Materials* **2017,** *29* (22), 1700008.
172. Lin, Z.; Wang, X., Nanostructure engineering and doping of conjugated carbon nitride semiconductors for hydrogen photosynthesis. *Angewandte Chemie* **2013,** *125* (6), 1779-1782.
173. Ruan, Q.; Luo, W.; Xie, J.; Wang, Y.; Liu, X.; Bai, Z.; Carmalt, C. J.; Tang, J., Nanojunction polymer photoelectrode for efficient charge transport and separation. *Angewandte Chemie International Edition* **2017**.
174. Fang, Y.; Xu, Y.; Li, X.; Ma, Y.; Wang, X., Coating polymeric carbon nitride photoanodes on conductive Y: ZnO nanorod arrays for overall water splitting. *Angewandte Chemie* **2018**.

175. Volokh, M.; Peng, G.; Barrio, J.; Shalom, M., Carbon Nitride Materials for Water Splitting Photoelectrochemical Cells. *Angewandte Chemie International Edition* **2018**.
176. Ruan, Q.; Luo, W.; Xie, J.; Wang, Y.; Liu, X.; Bai, Z.; Carmalt, C. J.; Tang, J., A nanojunction polymer photoelectrode for efficient charge transport and separation. *Angewandte Chemie International Edition* **2017,** *56* (28), 8221-8225.
177. Lin, L.; Yu, Z.; Wang, X., Crystalline Carbon Nitride Semiconductors for Photocatalytic Water Splitting. *Angewandte Chemie International Edition* **2018**.
178. Kim, T. W.; Choi, K.-S., Nanoporous BiVO4 photoanodes with dual-layer oxygen evolution catalysts for solar water splitting. *Science* **2014**, 1245026.
179. Yu, J.; Kudo, A., Effects of structural variation on the photocatalytic performance of hydrothermally synthesized BiVO4. *Advanced Functional Materials* **2006,** *16* (16), 2163-2169.
180. Baeck, S. H.; Choi, K. S.; Jaramillo, T. F.; Stucky, G. D.; McFarland, E. W., Enhancement of photocatalytic and electrochromic properties of electrochemically fabricated mesoporous WO3 thin films. *Advanced Materials* **2003,** *15* (15), 1269-1273.
181. Jorand Sartoretti, C.; Alexander, B. D.; Solarska, R.; Rutkowska, I. A.; Augustynski, J.; Cerny, R., Photoelectrochemical oxidation of water at transparent ferric oxide film electrodes. *The Journal of Physical Chemistry B* **2005,** *109* (28), 13685-13692.
182. Duret, A.; Grätzel, M., Visible light-induced water oxidation on mesoscopic α-Fe2O3 films made by ultrasonic spray pyrolysis. *The Journal of Physical Chemistry B* **2005,** *109* (36), 17184-17191.
183. Agrios, A. G.; Pichat, P., Recombination rate of photogenerated charges versus surface area: opposing effects of TiO2 sintering temperature on photocatalytic removal of phenol, anisole, and pyridine in water. *Journal of Photochemistry and Photobiology A: Chemistry* **2006,** *180* (1-2), 130-135.
184. Wang, R.; Liu, H.; Fan, Z.; Li, L.; Cai, Y.; Xu, G.; Luo, W.; Yang, B.; Zhou, Y.; Zou, Z., Unconventional gas-based bottom-up, meter-area-scale fabrication of hydrogen-bond free g-CN nanorod arrays and coupling layers with TiO 2 toward high-efficiency photoelectrochemical performance. *Nanoscale* **2018,** *10* (7), 3342-3349.
185. Kim, K.-K.; Song, J.-H.; Jung, H.-J.; Choi, W.-K.; Park, S.-J.; Song, J.-H., The grain size effects on the photoluminescence of ZnO/α-Al 2 O 3 grown by radio-frequency magnetron sputtering. *Journal of Applied Physics* **2000,** *87* (7), 3573-3575.
186. Wang, H.; Zhang, X.; Xie, J.; Zhang, J.; Ma, P.; Pan, B.; Xie, Y., Structural distortion in graphitic-C 3 N 4 realizing an efficient photoreactivity. *Nanoscale* **2015,** *7* (12), 5152-5156.
187. Rajeshwar, K., Semiconductor electrodes and photoelectrochemistry. Wiley-VCH, ISBN: 2002; pp 978-3.
188. ter Heijne, A.; Liu, D.; Sulonen, M.; Sleutels, T.; Fabregat-Santiago, F., Quantification of bio-anode capacitance in bioelectrochemical systems using Electrochemical Impedance Spectroscopy. *Journal of Power Sources* **2018,** *400*, 533-538.
189. O'Regan, B. C.; Bakker, K.; Kroeze, J.; Smit, H.; Sommeling, P.; Durrant, J. R., Measuring charge transport from transient photovoltage rise times. A new tool to investigate electron transport in nanoparticle films. *The Journal of Physical Chemistry B* **2006,** *110* (34), 17155-17160.
190. Bian, J.; Li, Q.; Huang, C.; Li, J.; Guo, Y.; Zaw, M.; Zhang, R.-Q., Thermal vapor condensation of uniform graphitic carbon nitride films with remarkable photocurrent density for photoelectrochemical applications. *Nano Energy* **2015,** *15*, 353-361.
191. Dong, G.; Zhao, K.; Zhang, L., Carbon self-doping induced high electronic conductivity and photoreactivity of gC 3 N 4. *Chemical Communications* **2012,** *48* (49), 6178-6180.
192. Asahi, R.; Morikawa, T.; Ohwaki, T.; Aoki, K.; Taga, Y., Visible-light photocatalysis in nitrogen-doped titanium oxides. *science* **2001,** *293* (5528), 269-271.

193. Wang, Y.; Zhang, J.; Wang, X.; Antonietti, M.; Li, H., Boron ‐ and Fluorine ‐ Containing Mesoporous Carbon Nitride Polymers: Metal ‐ Free Catalysts for Cyclohexane Oxidation. *Angewandte Chemie International Edition* **2010,** *49* (19), 3356-3359.
194. Nagaveni, K.; Hegde, M.; Madras, G., Structure and Photocatalytic Activity of Ti1-x M x O2±δ (M= W, V, Ce, Zr, Fe, and Cu) Synthesized by Solution Combustion Method. *The Journal of Physical Chemistry B* **2004,** *108* (52), 20204-20212.
195. Choi, W.; Termin, A.; Hoffmann, M. R., Effects of Metal ‐ Ion Dopants on the Photocatalytic Reactivity of Quantum ‐ Sized TiO2 Particles. *Angewandte Chemie International Edition in English* **1994,** *33* (10), 1091-1092.
196. Inerbaev, T. M.; Hoefelmeyer, J. D.; Kilin, D. S., Photoinduced charge transfer from titania to surface doping site. *The Journal of Physical Chemistry C* **2013,** *117* (19), 9673-9692.
197. Matis, B. R.; Burgess, J. S.; Bulat, F. A.; Friedman, A. L.; Houston, B. H.; Baldwin, J. W., Surface doping and band gap tunability in hydrogenated graphene. *ACS nano* **2012,** *6* (1), 17-22.
198. Zhang, J.; Zhang, M.; Sun, R. Q.; Wang, X., A facile band alignment of polymeric carbon nitride semiconductors to construct isotype heterojunctions. *Angewandte Chemie* **2012,** *124* (40), 10292-10296.
199. Tong, Z.; Yang, D.; Sun, Y.; Nan, Y.; Jiang, Z., Tubular g ‐ C3N4 Isotype Heterojunction: Enhanced Visible ‐ Light Photocatalytic Activity through Cooperative Manipulation of Oriented Electron and Hole Transfer. *Small* **2016,** *12* (30), 4093-4101.
200. Wang, J.; Chen, Y.; Shen, Y.; Liu, S.; Zhang, Y., Coupling polymorphic nanostructured carbon nitrides into an isotype heterojunction with boosted photocatalytic H2 evolution. *Chemical Communications* **2017,** *53* (20), 2978-2981.
201. Liang, Q.; Li, Z.; Bai, Y.; Huang, Z. H.; Kang, F.; Yang, Q. H., A Composite Polymeric Carbon Nitride with In Situ Formed Isotype Heterojunctions for Highly Improved Photocatalysis under Visible Light. *Small* **2017,** *13* (9).
202. Moniz, S. J.; Shevlin, S. A.; Martin, D. J.; Guo, Z.-X.; Tang, J., Visible-light driven heterojunction photocatalysts for water splitting–a critical review. *Energy & Environmental Science* **2015,** *8* (3), 731-759.
203. Kawaguchi, M.; Kawashima, T.; Nakajima, T., Syntheses and structures of new graphite-like materials of composition BCN (H) and BC3N (H). *Chemistry of materials* **1996,** *8* (6), 1197-1201.
204. Lei, W.; Portehault, D.; Dimova, R.; Antonietti, M., Boron carbon nitride nanostructures from salt melts: tunable water-soluble phosphors. *Journal of the American Chemical Society* **2011,** *133* (18), 7121-7127.
205. Song, L.; Ci, L.; Lu, H.; Sorokin, P. B.; Jin, C.; Ni, J.; Kvashnin, A. G.; Kvashnin, D. G.; Lou, J.; Yakobson, B. I., Large scale growth and characterization of atomic hexagonal boron nitride layers. *Nano letters* **2010,** *10* (8), 3209-3215.
206. Wang, Y.; Li, H.; Yao, J.; Wang, X.; Antonietti, M., Synthesis of boron doped polymeric carbon nitride solids and their use as metal-free catalysts for aliphatic C–H bond oxidation. *Chemical Science* **2011,** *2* (3), 446-450.
207. Wang, X.; Maeda, K.; Thomas, A.; Takanabe, K.; Xin, G.; Carlsson, J. M.; Domen, K.; Antonietti, M., A metal-free polymeric photocatalyst for hydrogen production from water under visible light. *Nature materials* **2009,** *8* (1), 76-80.
208. Yan, S.; Li, Z.; Zou, Z., Photodegradation of rhodamine B and methyl orange over boron-doped g-C3N4 under visible light irradiation. *Langmuir* **2010,** *26* (6), 3894-3901.
209. Kisku, S. K.; Swain, S. K., Synthesis and characterization of chitosan/boron nitride composites. *Journal of the American Ceramic Society* **2012,** *95* (9), 2753-2757.
210. Ferrari, A. C.; Robertson, J., Interpretation of Raman spectra of disordered and amorphous carbon. *Physical review B* **2000,** *61* (20), 14095.

211. Larkin, P.; Makowski, M.; Colthup, N., The form of the normal modes of s-triazine: infrared and Raman spectral analysis and ab initio force field calculations. *Spectrochimica Acta Part A: Molecular and Biomolecular Spectroscopy* **1999,** *55* (5), 1011-1020.
212. Gu, Q.; Liao, Y.; Yin, L.; Long, J.; Wang, X.; Xue, C., Template-free synthesis of porous graphitic carbon nitride microspheres for enhanced photocatalytic hydrogen generation with high stability. *Applied Catalysis B: Environmental* **2015,** *165*, 503-510.
213. Zhang, J.; Chen, X.; Takanabe, K.; Maeda, K.; Domen, K.; Epping, J. D.; Fu, X.; Antonietti, M.; Wang, X., Synthesis of a Carbon Nitride Structure for Visible‐Light Catalysis by Copolymerization. *Angewandte Chemie International Edition* **2010,** *49* (2), 441-444.
214. Yang, S.; Gong, Y.; Zhang, J.; Zhan, L.; Ma, L.; Fang, Z.; Vajtai, R.; Wang, X.; Ajayan, P. M., Exfoliated graphitic carbon nitride nanosheets as efficient catalysts for hydrogen evolution under visible light. *Advanced materials* **2013,** *25* (17), 2452-2456.
215. Cummings, C. Y.; Marken, F.; Peter, L. M.; Tahir, A. A.; Wijayantha, K. U., Kinetics and mechanism of light-driven oxygen evolution at thin film α-Fe 2 O 3 electrodes. *Chemical Communications* **2012,** *48* (14), 2027-2029.
216. Zhang, J.; Sun, J.; Maeda, K.; Domen, K.; Liu, P.; Antonietti, M.; Fu, X.; Wang, X., Sulfur-mediated synthesis of carbon nitride: band-gap engineering and improved functions for photocatalysis. *Energy & Environmental Science* **2011,** *4* (3), 675-678.
217. Kong, D.; Zheng, Y.; Kobielusz, M.; Wang, Y.; Bai, Z.; Macyk, W.; Wang, X.; Tang, J., Recent advances in visible light-driven water oxidation and reduction in suspension systems. *Materials Today* **2018,** *21* (8), 897-924.
218. Guo, Y.; Li, J.; Yuan, Y.; Li, L.; Zhang, M.; Zhou, C.; Lin, Z., A Rapid Microwave‐Assisted Thermolysis Route to Highly Crystalline Carbon Nitrides for Efficient Hydrogen Generation. *Angewandte Chemie International Edition* **2016,** *55* (47), 14693-14697.
219. Wang, J.; Zhang, C.; Shen, Y.; Zhou, Z.; Yu, J.; Li, Y.; Wei, W.; Liu, S.; Zhang, Y., Environment-friendly preparation of porous graphite-phase polymeric carbon nitride using calcium carbonate as templates, and enhanced photoelectrochemical activity. *Journal of Materials Chemistry A* **2015,** *3* (9), 5126-5131.
220. Peng, G.; Albero, J.; Garcia, H.; Shalom, M., A Water‐Splitting Carbon Nitride Photoelectrochemical Cell with Efficient Charge Separation and Remarkably Low Onset Potential. *Angewandte Chemie* **2018,** *130* (48), 16033-16037.
221. Sagara, N.; Kamimura, S.; Tsubota, T.; Ohno, T., Photoelectrochemical CO2 reduction by a p-type boron-doped g-C3N4 electrode under visible light. *Applied Catalysis B: Environmental* **2016,** *192*, 193-198.
222. Zhang, Y.; Schnepp, Z.; Cao, J.; Ouyang, S.; Li, Y.; Ye, J.; Liu, S., Biopolymer-activated graphitic carbon nitride towards a sustainable photocathode material. *Scientific reports* **2013,** *3*, 2163.
223. Lau, V. W. h.; Klose, D.; Kasap, H.; Podjaski, F.; Pignié, M. C.; Reisner, E.; Jeschke, G.; Lotsch, B. V., Dark Photocatalysis: Storage of Solar Energy in Carbon Nitride for Time‐Delayed Hydrogen Generation. *Angewandte Chemie International Edition* **2017,** *56* (2), 510-514.
224. Ruan, Q.; Bayazit, M.; Kiran, V.; Xie, J.; Tang, J., Key Factors Dominating Photoelectrochemical Performance of g-C3N4 polymer films. *Chemical Communications* **2019**.
225. Sun, B.-w.; Yu, H.-y.; Yang, Y.-j.; Li, H.-j.; Zhai, C.-y.; Qian, D.-J.; Chen, M., New complete assignment of X-ray powder diffraction patterns in graphitic carbon nitride using discrete Fourier transform and direct experimental evidence. *Physical Chemistry Chemical Physics* **2017,** *19* (38), 26072-26084.
226. Zhang, Q.; Chen, P.; Tan, C.; Chen, T.; Zhuo, M.; Xie, Z.; Wang, F.; Liu, H.; Cai, Z.; Liu, G., A photocatalytic degradation strategy of PPCPs by a heptazine-based CN organic polymer (OCN) under visible light. *Environmental Science: Nano* **2018,** *5* (10), 2325-2336.

227. Allongue, P.; Cachet, H., Band‐Edge Shift and Surface Charges at Illuminated n‐GaAs/Aqueous Electrolyte Junctions Surface‐State Analysis and Simulation of Their Occupation Rate. *Journal of the Electrochemical Society* **1985,** *132* (1), 45-52.
228. Yang, Y.; Liu, G.; Irvine, J. T.; Cheng, H. M., Enhanced photocatalytic H2 production in core–shell engineered rutile TiO2. *Advanced Materials* **2016,** *28* (28), 5850-5856.
229. Klahr, B.; Gimenez, S.; Fabregat-Santiago, F.; Hamann, T.; Bisquert, J., Water oxidation at hematite photoelectrodes: the role of surface states. *Journal of the American Chemical Society* **2012,** *134* (9), 4294-4302.
230. Xu, J.; Li, D.; Chen, Y.; Tan, L.; Kou, B.; Wan, F.; Jiang, W.; Li, F., Constructing sheet-on-sheet structured graphitic carbon nitride/reduced graphene oxide/layered MnO2 ternary nanocomposite with outstanding catalytic properties on thermal decomposition of ammonium Perchlorate. *Nanomaterials* **2017,** *7* (12), 450.